Gas Chemistry of the Hellisheidi Geothermal Field

Samuel Warren Scott

Gas Chemistry of the Hellisheidi Geothermal Field

60 ECTS thesis submitted in partial fulfillment of a
Magister Scientiarum degree in Sustainable Systems (Earth Sciences)

Advisor(s)
Ingvi Gunnarsson
Andri Stefánsson
Stefán Arnórsson

External Examiner
Dr. Thráinn Fridriksson

Faculty of Science
School of Engineering and Natural Sciences
University of Iceland
Reykjavík, January 2011

Gas Chemistry of the Hellisheidi Geothermal Field
Gas Chemistry of Hellisheidi
60 ECTS thesis submitted in partial fulfillment of a *Magister Scientiarum* degree in Sustainable Systems (Earth Sciences)

Reykjavík Energy Graduate School of Sustainable Systems
Orkuveita Reykjavíkur
Baejarháls 1 110 Reykjavík

Faculty of Science
School of Engineering and Natural Sciences
University of Iceland
Sturlugötu 7, 101 Reykjavík
Iceland

Telephone: 525 4000

Abstract

A geochemical assessment of the Hellisheidi high-temperature geothermal field is presented based on the analysis of 21 wet-steam well discharges. Emphasis is placed on the chemical and physical processes that account for the concentrations of the major gases (CO_2, H_2S, H_2 and N_2). Aquifer chemical compositions were calculated from surface water and steam phase analyses and discharge enthalpies using the WATCH speciation program and phase segregation model. Under this model, discharge enthalpies in excess of that of vapor-saturated liquid at the aquifer temperature are accounted for by retention of liquid in the formation at a single pressure. Sensitivity analyses carried out to evaluate the effect of assumed phase segregation pressure on calculated concentrations of chemical components in initial aquifer fluids indicate the calculated concentrations of non-volatile components are insensitive to assumed phase segregation pressure for wells with discharge enthalpies below 2500 kJ kg^{-1}, while those of volatile components are observed to be very sensitive to the selected phase segregation pressure even at low excess enthalpies. A phase segregation pressure approximately half-way between the initial aquifer fluid and wellhead pressure is selected because the liquid saturation at this pressure corresponds well with a residual liquid saturation of 0.2-0.3.

The calculated chemical compositions of initial aquifer fluids show a close approach to equilibrium with the hydrothermal alteration minerals calcite, wollastonite, epidote, clinozoisite and prehnite. The concentrations of H_2S and H_2 generally seem to be controlled by a mineral assemblage consisting of pyrite, pyrrhotite, prehnite and epidote. The elevated H_2 concentrations found in most total aquifer fluids relative to equilibrium with liquid water indicate the presence of a small equilibrium vapor fraction in the initial aquifer fluid, approximately 0.2% by mass. In general, calculated H_2 and H_2S concentrations are higher in the proximity of two proposed upflow zones: 1) near the eruptive fissure of ~1100 b.p., in alignment with the axial fissure swarm from Reykjafell towards the NE 2) on the southern margin of Skardsmýrarfjall, to the southeast of Hamragil. In contrast to H_2S and H_2, the concentrations of CO_2 and N_2 are source-controlled, and the high N_2 and low Cl in liquid enthalpy wells to the north define the location of a recharge zone.

Útdráttur

Þessi ritgerð fjallar um jarðefnafræðilega athugun á borholuvökva í háhitakerfinu á Hellisheiði. Hún er byggð á efnagreiningum á 21 sýnum af vatni og gufu úr vinnsluholum á svæðinu. Áhersla var lögð á að greina þau efna- og eðlisfræðilegu ferli sem ráða styrk algengustu gastegunda (CO_2, H_2S, H_2 og N_2) í borholuvökva. Styrkur efna í aðfærsluæðum borhola var reiknaður út frá efnagreiningum af vatns- og gufusýnum sem safnað var á holutoppi með WATCH-forritinu. Reiknað var með að aðskilnaður hama í æð væri orsök hávermis í mörgum holanna. Samkvæmt þessum reikningum er vermi holuvökva umfram vermi gufumettaðs vatns við hita í æð talinn orsakast af því að hluti vatns í þeim vökva sem upphaflega flæðir að borholu sitji eftir í æðinni með því að loða við yfirborði steinda en að öll gufan flæði inn í borholur. Gert var ráð fyrir að þessi aðskilnaður hama yrði við einn ákveðinn þrýsting. Næmisreikningar sem gerðir voru til að meta áhrif valins þrýstings fyrir aðskilnað hama á reiknaðann styrk efna í upprunalegum vökva í æð sýna að áhrifin eru lítil fyrir uppleyst steinefni, allt upp í vermi sem nemur 2500 kJ/kg. Á hinn bóginn er reiknaður styrkur gastegunda í æð næmur fyrir vali að aðskilnaðarþrýstingi. Valinn var þrýstingur fyrir aðskilnað sem liggur mitt á milli gufuþrýstings við sýnatöku annars vegar og í æð hins vegar. Ástæðan er sú að vatnsmettun við þennan þrýsting liggur á bilinu 0,2 til 0,3 en þau gildi teljast raunhæf.

Reiknaður styrkur efna í vökva í æð sýna að vökvinn er nálægt efnajafnvægi við ummyndunarsteindir eins og kalsít, wollastónít, epídót og prenít. Styrkur H_2S og H_2 í djúpvatni virðist yfirleitt ráðast af efnajafnvægi við steindafylkið pýrít-pýrrótít-prenít-epídót. Hinn tiltölulega hái styrkur H_2 í djúpvökva margra borhola er talinn stafa af djúpgufu í æð, u.þ.b. 0,2% miðað við þunga að meðaltali. Yfirleitt er reiknaður styrkur H_2 og H_2S hæstur í djúpvökva nálægt megin-uppstreymisrásum, þ.e.a.s. 1) nálægt sprungunni sem gaus árið 1000 frá Reykjafelli í norðausturátt, 2) við suðurrætur Skarðsmýrarfjalls í suðaustur frá Hamragili. Andstætt þessu ræðst styrkur CO_2 og N_2 í aðfærsluæðum borhola af flæði þeirra í jarðhitavökvann og hinn hái styrkur N_2 og lágur styrkur Cl in holum með vökvavermi nyrst á vinnslusvæði Hellisheiðar er talinn endurspegla írennsli í svæðið.

Dedicated to my grandfather, Warren Culbertson.

Table of Contents

List of Figures

List of Tables

Abbreviations

D_s^e	Distribution coefficient for volatile species s at the point of phase segregation
D_s^f	Distribution coefficient for volatile species s in initial aquifer fluid
$h^{d,l}$	Enthalpy of saturated liquid at sampling pressure p^s (kJ kg^{-1})
$h^{d,t}$	Total enthalpy of well discharge (kJ kg^{-1})
$h^{d,v}$	Enthalpy of saturated vapor at sampling pressure p^s (kJ kg^{-1})
$h^{e,l}$	Enthalpy of saturated liquid at phase segregation pressure p^e (kJ kg^{-1})
$h^{e,t}$	Total enthalpy of two-phase fluid immediately before phase segregation (kJ kg^{-1})
$h^{e,v}$	Enthalpy of saturated vapor at phase segregation pressure p^e (kJ kg^{-1})
$h^{f,l}$	Enthalpy of saturated liquid at initial aquifer fluid conditions (kJ kg^{-1})
$h^{f,t}$	Total enthalpy of initial aquifer fluid. If $X^{f,v}$ is assumed to be 0, $h^{f,t} = h^{f,l}$ (kJ kg^{-1})
$h^{f,v}$	Enthalpy of saturated vapor at initial aquifer fluid conditions (kJ kg^{-1})
$h^{g,t}$	Total enthalpy of two-phase fluid immediately after phase segregation (kJ kg^{-1})
$K_{H,s}$	Henry's Law solubility constant for volatile species s
$L^{e,v}$	Latent enthalpy of vaporization at phase segregation pressure p^e (kJ kg^{-1})
$L^{f,v}$	Latent enthalpy of vaporization at initial aquifer fluid conditions (kJ kg^{-1})
$m_i^{d,l}$	Concentration of chemical component i in liquid phase at sampling pressure p^s (moles kg^{-1})
$m_i^{d,t}$	Concentration of chemical component i in total well discharge (moles kg^{-1})
$m_i^{d,v}$	Concentration of chemical component i in vapor phase at sampling pressure p^s (moles kg^{-1})
$m_i^{e,l}$	Concentration of chemical component i in liquid phase at phase segregation pressure p^e (moles kg^{-1})
$m_i^{e,t}$	Concentration of chemical component i in total fluid immediately before phase segregation (moles kg^{-1})
$m_i^{e,v}$	Concentration of chemical component i in vapor phase at phase segregation pressure p^e (moles kg^{-1})
$m_i^{f,l}$	Concentration of chemical component i in liquid phase of initial aquifer fluid (moles kg^{-1})
$m_i^{f,t}$	Concentration of chemical component i in initial aquifer fluid. If $X^{f,v} = 0$, $m_i^{f,t} = m_i^{f,l}$ (moles kg^{-1})
$m_i^{g,t}$	Concentration of chemical component i in total fluid immediately after phase segregation (moles kg^{-1})
$m_r^{d,l}$	Concentration of non-volatile r in liquid phase at sampling pressure p^s (moles kg^{-1})
$m_r^{d,t}$	Concentration of non-volatile r in total well discharge (moles kg^{-1})
$m_r^{e,l}$	Concentration of non-volatile r in liquid phase at phase segregation pressure p^e (moles kg^{-1})
$m_r^{e,t}$	Concentration of non-volatile r in total fluid immediately prior to phase segregation (moles kg^{-1})
$m_r^{e,v}$	Concentration of non-volatile r in vapor phase at phase segregation pressure p^e (moles kg^{-1})
$m_r^{f,l}$	Concentration of non-volatile r in liquid phase of initial aquifer fluid (moles kg^{-1})
$m_r^{f,t}$	Concentration of non-volatile r in total initial aquifer fluid. If $X^{f,v} = 0$, $m_r^{f,t} = m_r^{f,l}$
$m_s^{d,l}$	Concentration of volatile species s in liquid phase at sampling pressure p^s (moles kg^{-1})
$m_s^{d,t}$	Concentration of volatile species s in total well discharge (moles kg^{-1})
$m_s^{d,v}$	Concentration of volatile species s in vapor phase at sampling pressure p^s (moles kg^{-1})
$m_s^{e,l}$	Concentration of volatile species s in liquid phase at phase segregation pressure p^e (moles kg^{-1})
$m_s^{e,t}$	Concentration of volatile species s in total fluid immediately prior to phase segregation (moles kg^{-1})
$m_s^{e,v}$	Concentration of volatile species s in vapor phase at phase segregation pressure p^e (moles kg^{-1})
$M^{d,l}$	Mass flow of liquid in wet-steam well discharge (kg s^{-1})
$M^{d,t}$	Mass flow of liquid and steam in wet-steam well discharge (kg s^{-1})
$M^{d,v}$	Mass flow of steam in wet-steam well discharge (kg s^{-1})
$M^{e,lr}$	Mass flow of boiled aquifer liquid which separates from steam flowing into well (kg s^{-1})
$M^{f,t}$	Mass flow of total initial aquifer fluid into well (kg s^{-1})

p^e	Vapor pressure at which phase segregation is assumed to occur (bar-a)
$p^{e,mid}$	Approximate mid-point phase segregation pressure, determined by specific method described in text (bar-a)
p^f	Saturation pressure at initial aquifer fluid temperature T^f (bar-a)
p^{wh}	Vapor pressure as read from gauge attached to well-head (bar-g)
p^s	Vapor pressure as read from gauge atop Webre separator (bar-g)
$S^{e,l}$	Liquid saturation (volume fraction of liquid phase) phase segregation pressure p^e
T^e	Saturation temperature at phase segregation pressure p^e (°C)
T^f	Temperature of initial aquifer fluid (°C). For most wells in this study, equal to $T_{qtz,GA}$.
$T_{qtz,GUD}$	Fluid temperature (°C) as determined using the silica geothermometer of Gudmundsson and Arnórsson (2002).
$T_{qtz,GA}$	Fluid temperature (°C) as determined using the quartz geothermometer of Gunnarsson and Arnórsson (2001).
$T_{Na/K}$	Fluid temperature (°C) as determined using the Na/K geothermometer of Arnórsson (2000).
$X^{d,v}$	Mass fraction of vapor at sampling pressure p^s
$X^{e,v}$	Mass fraction of vapor immediately prior to phase segregation
$X^{f,v}$	Vapor mass fraction present in the initial aquifer fluid (see Section 3.3)
$X_{H2}^{f,v}$	Calculated equilibrium vapor fraction assuming equilibrium H_2 concentrations in liquid phase (see text)
$X_{H2S}^{f,v}$	Caclulated equilibrium vapor fraction assuming equilibrium H_2S concentrations in liquid phase (see text)
$X^{g,v}$	Mass fraction of vapor immediately after phase segregation
$V^{e,lr}$	Relative mass of boiled water retained in aquifer upon phase segregation to well discharge ($M^{e,lr}/M^{d,t}$)
$V^{f,t}$	Relative mass of total inflowing initial aquifer fluid to well discharge ($M^{f,t}/M^{d,t}$)

Acknowledgements

1 Introduction

Geochemical investigations of well discharge fluids can be a valuable tool for characterizing and managing the complex heat and fluid resources of hydrothermal systems. The high-temperature, high-pressure, volatile-rich two phase fluids expelled from wet-steam wells in volcanic geothermal systems pose unique challenges in terms of chemical analysis and modeling of initial aquifer fluid compositions. Early studies provided compelling evidence that fluid compositions were controlled by equilibrium with select hydrothermal alteration minerals commonly identified in well cuttings (e.g. Arnórsson et al., 1983a). Due to the relatively high abundance and reactivity of the main geothermal gases (CO_2, H_2S, H_2 and to a lesser extent, CH_4), these components were viewed as of particular interest for their ability to elucidate the physical nature of hydrothermal systems (e.g. Ármannsson et al., 1982; Gudmundsson and Arnórsson, 2002). Many studies have shown that the aquifer fluid concentrations of H_2S and H_2 closely approach equilibrium specific hydrothermal mineral assemblages (e.g. Arnórsson and Gunnlaugsson, 1985; Arnórsson et al., 2010). This may also be the case with CO_2, but in some settings its concentration in aquifer fluids is source controlled. In the abscence of organic sediments, the source of N_2 and Ar in hydrothermal fluids is equilibration of recharging, meteoric waters with the atmosphere.

In Iceland, it is common to encounter wells whose discharge enthalpies are higher than that of steam-saturated water at the feedzone temperature. Wells with excess discharge enthalpies pose a particular challenge for those interested in modeling aquifer fluid compositions, and several non-isolated system models accounting for the boiling processes between aquifer and wellhead have been developed (e.g. Arnórsson et al., 1990; Arnórsson et al., 2007). In some settings, the excess discharge enthalpies are dominantly attributed to the process of phase segregation, the result of the adhesion of liquid water to mineral grain surfaces due to capillary forces. This study attempts to apply and explore the sensitivity of calculated aquifer fluid compositions to assumed phase segregation pressure for 21 wet-steam well discharges that have recently been sampled at the Hellisheidi geothermal field in southwestern Iceland. The state of chemical equilibria between the main hydrothermal alteration minerals and solution will be assessed; for the reasons given above, more attention will be given to gaseous components. Additionally, physical explanations will be proposed to account for several of the observed trends in the distribution of these components on the scale of the geothermal field.

Section 2 provides a detailed background of the Hellisheidi field and the Hengill geothermal area of which it is a part. It provides a fairly detailed account of the many geophysical investigations that have been performed in the area, which have allowed the deep structure of the hydrothermal system to become clearer. Additionally, it will describe the lithology and alteration mineralogy and will review existing chemical studies of the area. It will conclude with a summary of basic conceptual model for the area that can serve as a framework for the present chemical studies. Section 3 describes the methodology employed in this study. It begins by briefly reporting the sampling and analytical techniques. However, the heart of this section is a description of phase segregation and its application in modeling aquifer fluid compositions, including both a physical description of the process of phase segregation, evidence for the occurrence of phase segregation in the

1

Hellisheidi field, a mathematical description of the phase segregation model and the procedure to incorporate phase segregation calculations into modeling using WATCH. A mathematical account of the way in which equilibrium vapor fraction is determined is provided. This section will also account for the thermodynamic database used to model aquifer fluid compositions. Section 4 presents and discusses the results obtained from the modeling described in Section 3. In addition to assessing the state of equilibria with respect to mineral-solution and mineral-gas reactions, this section will describe the field-scale distribution of the gases and attempt to correlate this distribution with physical processes, such as upflow, recharge and outflow. Section 5 will offer my conclusions and discuss directions for future work.

2 Hengill Geothermal Area

The Hellisheidi geothermal field is one of four sub-fields making up the greater Hengill geothermal field, along with Nesjavellir, Bitra and Hverahlid. Hengill is one of the largest in extent and most heavily exploited high-temperature geothermal fields in Iceland. Early interest in large-scale development of Hengill field was focused on the Nesjavellir subfield, with extensive drillings beginning in 1982 and the construction of the Nesjavellir geothermal co-generation plant in 1987 with the first stage, 100 MW$_{th}$, coming on-line in 1990. Thermal power capacity was expanded to 150 MW$_{th}$ in 1992, followed by a further expansion to combined generation of 200 MW$_{th}$ and 60 MW$_e$ in 1998. A series of successive additions up to 2005 have brought the Nesjavellir plant to its current production capacity of 290 MW$_{th}$ and 190 MW$_e$. Development of the Hellisheidi subfield has progressed at a rapid rate since the decision to commence exploratory drilling in 2001. The results of the first seven deep wells drilled by 2003 indicated the existence of an attractive hydrothermal resource (Gunnlaugsson and Gíslason, 2005). Subsequently, a major drilling campaign was mounted. Electricity production in two 45 MW$_e$ units began at Hellisheidi in 2006 and was further expanded in 2007 with a 33 MW$_e$ low-pressure turbine and again in 2008 with two additional 45 MWe units. Current electricity production stands at 213 MW$_e$, with an additional 90 MW$_e$ scheduled to come online in 2011.

Due to the importance of the geothermal resource at Hengill and its proximity to Reykjavík, the field is the most well-studied in Iceland (see e.g. Einarsson, 1960; Björnsson et al., 1986; Foulger and Toomey, 1989; Saemundsson, 1995a, b; Arnórsson, 1995; Árnason et al., 2010; Franzson et al., 2010; Gunnarsson et al., 2010, Jousset et al., 2011). In this section, the broad insights into the nature of the Hengill system gained from these investigations are reviewed. The discussion begins with an overview of its tectonic setting and geologic structure, as revealed by geological mapping, geochemical surveys and various methods of geophysical exploration. This is followed by a description of the lithology and alteration mineralogy observed at Hengill, which also help inform the understanding of the nature of the geothermal system. Next, insight gleaned from past investigations of the fluid and gas geochemistry at Hengill is summarized. In conclusion, a conceptual model of the geothermal system is proposed on the basis of this existing evidence; this will serve as a baseline upon which this study can build. Emphasis is placed on aspects of the geothermal system that are currently unresolved and might be able to be better understood through the application of geochemistry.

2.1 Geologic Background

The Hengill Central Volcano Complex (HCVC) is located on the North American-Eurasian plate boundary, at a triple junction where an axial rift zone (the Western Volcanic Zone, WVZ) and an oblique spreading ridge (the Reykjanes Peninsula Volcanic Zone, RPVZ) meet a seismically active transform zone (the South Iceland Seismic Zone, SISZ). Primary elements of the geology of Iceland and the position of the HCVC astride the Mid-Atlantic Ridge are shown in Figure 2.1. While Hengill itself is a presently active central volcano system, two other overlapping and successive subsidiary central volcanic systems
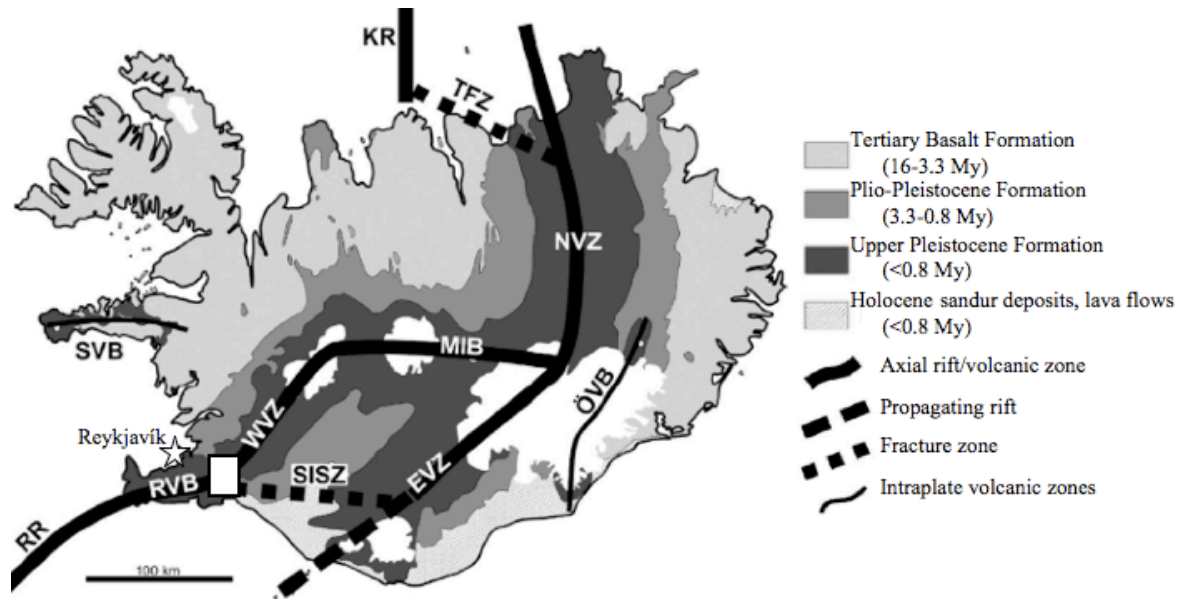
Figure 2.1. Principal elements of the geology of Iceland, outlining the major geological subdivisions, main fault structures and volcanic zones. Includes the approximate locations of Reykjavík and the Hengill geothermal field. Modified after Thordarson and Larsen (2007). RR, Reykjanes Ridge; RVB, Reykjanes Volcanic Belt; SISZ, South Iceland Seismic Zone; WVZ, West Volcanic Zone; MIB, Mid-Iceland Belt; EVZ, East Volcanic Zone; NVZ, North Volcanic Zone; TFZ, Tjörnes Fracture Zone; KR, Kolbeinsey Ridge; ÖVB, Öræfi Volcanic Belt; SVB, Snæfellsnes Volcanic Belt.

are usually grouped within the HCVC on the basis of a common locus of crustal accretion (Foulger and Toomey, 1989; Árnason et al., 1987) (see Figure 2.2). The oldest of these systems is Grensdalur (also referred to as Graendalur), located about 10 km to the southeast of the Hengill massif. This extinct central volcano was active between 700 and 30 ky, but has since been deeply eroded (Saemundsson and Arnórsson, 1971). It is associated with a NNE-trending fissure swarm, and is the heat source for the Reykjadalur and Hveragerdi subfields. The Hrómundartindur central volcano system is located approximately parallel to and between the Hengill and Grensadalur systems. This system is believed to be the heat source for the Bitra subfield. In contrast to the other two systems, no fissure swarm or central graben structure visible on the surface is associated with this system (Árnason et al., 1987). Although this system remains dynamic, with surface eruptions occurring as recently as 11 ky, the eruptive activity here is relatively minor as compared to Hengill, the present center of westward-migrating crustal accretion since the demise of Grensadalur (Foulger and Toomey, 1989).

Development of rifting in the WVZ was initiated at around 6-7 Ma, preceded by a southeastward jump of the rift zone (Jóhanneson, 1980). The subsequent southwestern propagation of spreading and accommodation of the seafloor spreading along the NE-oriented plate boundary opened up a system of swarms of tension fractures, normal faults and tectonic fissures, which in turn sometimes developed volcanic centers. Since the commencement of the southward propagation of the Eastern Volcanic Zone (EVZ) at about 1.5-3 Ma, rifting has been partitioned episodically between the two zones (Sigmundsson et al., 1995). GPS monitoring indicates a present extension rate of 3-7 mm/yr along the WVZ (LaFemina et al., 2005) compared to ~18-20 mm/yr across the entire plate boundary in Iceland (Geirsson et al., 2006), suggesting only 20-30% of the total opening across Iceland is being accommodated along the WVZ (Sinton et al, 2005). Eventually, another southeastward ridge jump is expected, and the EVZ will become the center of extension in

4

South Iceland (e.g. Einarsson, 1991). Until then, the left-lateral transform motion between the RPVZ and the EVZ is accommodated in the SISZ by motion on many parallel, NS-oriented, dextral transverse faults and counterclockwise rotation of the blocks between the faults in a mechanism described as "bookshelf faulting" (e.g. Einarsson, 2008).

The stress field in Hengill, presumed to be controlled by tensional stress parallel to the direction of spreading along the axial rift zone (e.g. Björnsson et al., 1986), is complicated by the transform character of the SISZ. The SISZ is manifested by seismically-active transverse lineaments that intercept the fissure swarm to the east (e.g. Árnason and Magnússon, 2001). Structurally, the main component of the HCVC is a 40-80 km long NNE/SSW-striking fissure/fault swarm sub-parallel to the rifting axis of the WVZ which together constitute a 3-5 km wide graben bounded on the west by two major faults with a total throw of about 300 m (e.g. Árnason et al., 1986; Saemundsson, 1995a; Franzson et al., 2010). The major faults bounding the eastern margin of the graben, along with the minor faults in the center, have not been as accurately placed due to the lack of reliable horizontal marker horizons. These are assumed to have a similar overall throw to the western margin faults, although taken up by larger number of step-faults (Franzson et al., 2005; Helgadóttir et al., 2010; Hardarson et al., 2010). The fissure swarm was last active in 1789, with extensive rifting and subsidence, but without any extrusive volcanic activity (Saemundsson, 1992). While the interaction between dilationary rifting of the fissure swarm and the transform component related to the SISZ is not very well understood, the role of these transverse faults is clearly important to the geothermal system as a whole, as extrusive and intrusive volcanic production is highest and overall geothermal activity is more intense on the southern and northern margin of the zone where these faults intersect the fissure swarm (Árnason and Magnúson, 2001).

Early geologic study of Hengill began by mapping of major geological units, locations of hot springs and fumaroles, fault traces, and thermally altered ground (Einarsson, 1960; Saemundsson, 1967), followed by a regional geophysical survey carried out between 1975-1986. Direct-current (DC) resistivity measurements showed extensive zones of high conductivity elongated along the main fissure swarm and connecting the Hengill and Grensadalur central volcanoes perpendicular to the main fissure swarm, with an areal extent of approximately 110 km^2 (Björnsson et al., 1986; Árnason et al., 1987). An aeromagnetic study revealed the presence of a distinct magnetic low within the positive anomaly of the normally-magnetized Brunhes epoch lavas of the Neovolcanic zone that coincided with the orientation of the fissure/fault swarm, fumaroles and hot springs of the HCVC (Björnsson and Hersir, 1981). This was taken to indicate that magnetite was unstable within this zone as a result of interaction with high-temperature geothermal fluids. Additionally, a gravity survey revealed an elongate NNE trending gravity low along the axis of the volcanic zone, presumably caused by low-density, high-porosity hyaloclastites of the Hengill system and high temperature at depth (Thorbergsson et al., 1984). Positive gravity anomalies above the extinct Grensadalur system and Húsmúli systems were attributed to the presence of dense, cool intrusions and a high-degree of alteration. These were also correlated with anomalously high P-wave velocities inferred from teleseismic studies (Foulger, 1984).

Extensive central-loop transient electromagnetic (TEM) resistivity studies of the Hengill system were carried out between 1986 and 2000 (Árnason and Magnúson, 2001) and subsequently used to correct large near-surface resistivity heterogeneities that hampered the interpretation of magnetotelluric (MT) soundings performed in 2000-2006 (Árnason et al., 2010). The resistivity structure of Hengill as determined by these investigations is displayed at sea level and 500 m b.s.l. in Figure 2.2 (see Figure 21 in

Árnason et al. (2010) for the resistivity structure to depths >10 km b.s.l.). In addition to the widespread low-resistivity anomaly found in the previous studies, a high-resistivity zone stretching SE from Hengill to Grensadalur volcanic center was identified at 400-800 m depth. At depths >500 m b.s.l., this high-resistivity zone gradually spreads to the SW along the fissure swarm; by 1200 m b.s.l., it extends across nearly the entire Hengill area. The transition between the high- and low- resistivity layers corresponds to the shift in an alteration mineralogy regime dominated by smectite clays, which can freely conduct cations along the charged surfaces of the clay, to one dominated by chlorite, where cations are locked in crystal structures. Since alteration minerals persist even after temperature conditions change, it is important to keep in mind that resistivity measurements can only serve to indicate the maximum extent of high-temperature geothermal activity.

On the basis of MT measurements, a second underlying low-resistivity zone was identified at >3 km b.s.l. beneath the prominent WNW/ENE-oriented high-resistivity layer centered on Mt. Hengill; similar to the pattern observed for the high-resistivity layer, the low-resistivity zone extends to the SW around 4.5 km b.s.l. and is widespread by 6.5 km b.s.l. This deep conductive layer is believed to be important to the nature of the geothermal system as a whole (Árnason et al., 2010). Seismic tomography has provided no convincing signs of *S*-wave attenuation beneath Hengill and, in fact, has revealed that the reduction in seismic wave velocities observed >3 km depth is stronger for *P*- than *S*-waves, contrary to what would be expected if a shallow magma chamber were present (Foulger et al., 1995; Tryggvason et al., 2002). Hence, it is unlikely that the deep conductive layer can be attributed to the presence of molten rock. Microearthquake relocations using broadband (Jousset et al., 2010) and permanent (Vogfjörd and Hjaltadóttir, 2007) seismic networks have shown that the depth range of events is generally confined to 2-5 km depth. On the basis of these findings and previous studies of the structure of oceanic crust, Árnason et al.
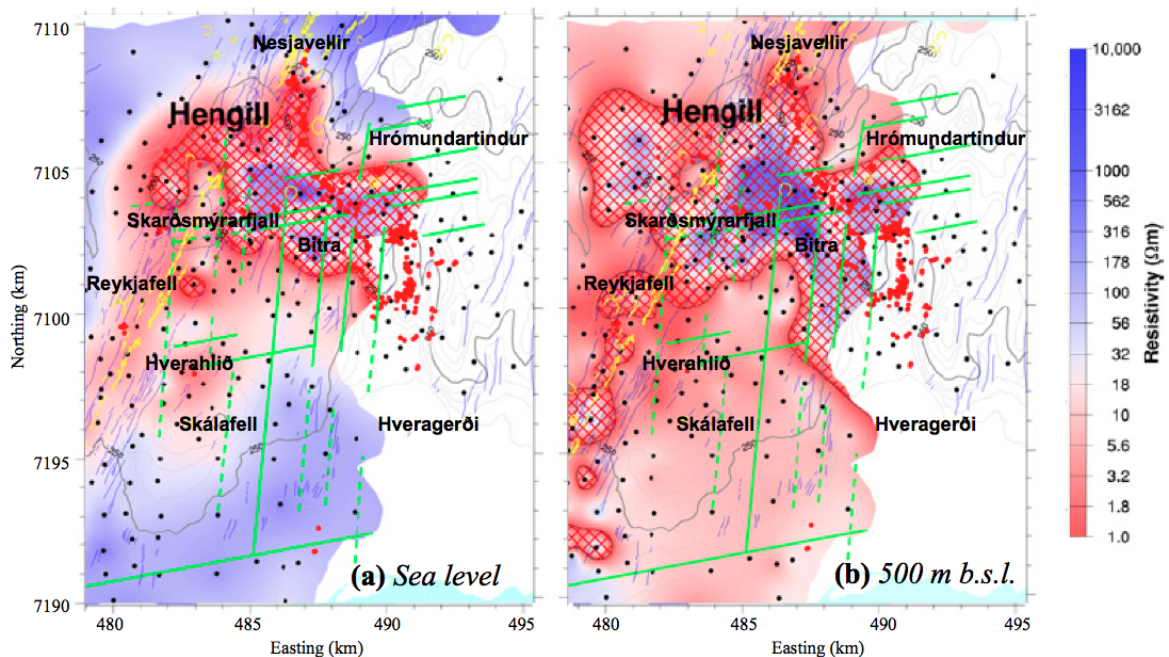
Figure 2.2: Resistivity in the Hengill area based on 1-D inversion of TEM data **(a)** *at sea level elevation and* **(b)** *at 500 m b.s.l. Faults and fractures mapped on the surface are shown in blue, faults inferred from seismicity in green, geothermal surface manifestations as red dots, TEM sounding stations as black dots and topographic contour lines (m a.s.l.) as black lines. The red-hatched area represents the resistive core. Modified after Árnason et al. (2010).*

6

(2010) considered the onset of the low-resistivity anomaly at >3 km depth to represent the transition from a dominantly extrusive, brittle lithology to a hotter, more ductile regime of solidified dykes and intrusions (a sheeted dyke complex). The high conductivity observed at this depth was explained as the result of accumulation of dissolved incompatible ions (Cl), as the sudden and periodic formation of vertical fractures in the intensely strained rock reservoir reduced fluid pressures from lithostatic to hydrostatic, resulting in boiling of previously trapped "magmatic waters" and subsequent escape of "supercritical hydrous fluids". Similarly, the V_p/V_s reduction at >3 km depth was attributed to "supercritical" fluids (Foulger et al., 1995; Tryggvason et al., 2002). This theory was supported by accounts of superheated steam (>380°C) encountered during the drilling of Nesjavellir well NJ-11 at a depth of 2265 m (Steingrímsson et al., 1986; Steingrímsson et al., 1990). The potential for harnessing supercritical fluids at depth in Hengill attracted the interest of the Iceland Deep Drilling Project (IDDP) (Fridleifsson et al., 2003). The critical point of pure water is exceeded at ~374°C and 221 bars, corresponding to a hydrostatic head of ~3500 m. Due to practical drilling limitations, sufficient well depths have not been attained.

The model proposed by Árnason et al. (2010) implies that the basaltic dikes and intrusions that make up the ductile, conductive layer act as the heat source for the geothermal system. During major rifting episodes, these dikes and intrusions extend to the surface, resulting in fissure eruptions. As stated previously, the deep-conductive layer appears at shallowest depth SE of Hengill in the Hrómundartindur/Bitra region lying near the intersection of several E/W- and N/S- oriented faults, where the most intense seismicity was measured throughout the 1991-2001 episode and near the center of uplift after the injection of ~0.1 km^3 magma in 1994-1995 (Sigmundsson et al., 1997). However, downhole temperature measurements from well ÖJ-1, drilled directly above this area, indicate temperatures <200°C at 1 km depth, seemingly contradicting the notion of an intensive heat source existing at 3-4 km depth (Árnason and Magnússon, 2001). Árnason et al. (2010) accounted for this by proposing the existence of two separate thermal regimes within the reservoir, where the impermeable dikes and intrusions act as permeability barrier between a shallower, lower temperature convective cell and deeper, much hotter geothermal reservoir. The broad shape of the resistivity anomaly may be indicative of a sill-shaped intrusion emplaced at relatively shallow depth (3-4 km). This model for the Bitra subfield contrasts somewhat with that for Hellisheidi and Nesjavellir subfields, where the shallow intrusive activity at >1.5 km depth consists of predominantly subvertical dikes.

2.2 Lithology and Alteration Mineralogy

While the surface geology of the Hengill area has been extensively mapped and studied (Einarsson, 1960; Saemundsson, 1967; Saemundsson, 1995a), the lithology and alteration mineralogy of the subsurface reservoir is less well described, especially in the Hellisheidi sector. According to Helgadóttir et al. (2010), well cuttings from approximately half of the Hellisheidi wells have been studied in detail, with only preliminary data available. The borehole geology of the Nesjavellir subfield has been studied intensively by Franzson (1988, 1994, 1998). While much of the existing data is in Icelandic or not open to the public, several studies of the reservoir geology of individual Hellisheidi wells to 800 or 1200 m depth have been made available by the United Nations University Geothermal Training Program (Getahneh, 2001; Eshaghpour, 2003; Haranto, 2005; Pendon, 2006; Koestono, 2007; Gebrehiwot et al., 2010; Mesfin, 2010).

The main rock types observed at the Hengill area are intimately related to its volcanic and glacial setting. The driving force of rifting has been attributed to magma

pressurization in elongate, deep-seated reservoirs situated at the base of the crust (>20 km) and subsequent, periodic injection of subvertical dykes into the upper crust (Gudmundsson, 1995). Recurrent eruptive activity and the maintenance of a long-lived plumbing system can result in the formation of central volcano structures. As is common for many of the volcanic systems in Iceland, much of the eruptive activity at Hengill has been sub- and intra-glacial (Jakobsson and Gudmundsson, 2008). These eruptions typically produce pillow basalt at the base, where water pressure is sufficient to prevent mixing or fragmentation of lava, and are overlain by hyaloclastite, variably consolidated and stratified fine- to coarse-grained pillow, breccia, tuff and tephra fragments formed by the rapid quenching of lava upon mixing with external water. When an eruptive vent emerges above the water level and becomes effusive, foot-flow breccias composed of sub-aerial eruptive products accumulate on the flanks of the sloping hyaloclastite deposits. When this succession of eruptive products is covered by a thick cap lava, the geologic structure is known as a tuya (also referred to as a table mountain). As indicated by the geologic map shown in Figure 2.3, the aforementioned eruptive products form the majority of the lithologic units observed in the Hellisheidi area. Minor, but nonetheless significant, quantities of rhyolite are also observed on the eastern margins of the Hengill graben.

There is a high degree of variability in the petrological and physical properties of hyaloclastite (Franzson et al., 2001). In the reports mentioned above describing the borehole geology of individual Hellisheidi wells, several 50-300 m thick hyaloclastite units, divided on the basis of textural or compositional distinctions, are sub-divided into 20-100 m thick breccia, tuff and pillow subunits, with minor scoria and tuffaceous sediments also described. These units are generally compositionally characterized as tholeiitic basalt dominantly composed of palagonite, the primary alteration product of volcanic glass, with highly variable olivine, plagioclase and pyroxene (augite) phenocrysts as well as accessory magnetite and ilmenite. Porosity can be quite variable for hyaloclastite, ranging from 0 to >40%, depending on the grain size and vesicle intensity of the intergranular fragments and, especially, on the degree of alteration and vesicular infilling (Franzson et al., 2001). Although porosity can be quite high, the permeability of hyaloclastite is generally low unless it is found in a highly fractured environment.

Intercalated within the hyaloclastite are a series of subaerial lava flows, representing eruptive activity during interglacial periods. While four distinct layers can be found in the Hellisheidi subfield, lava sequences are generally more numerous and thicker in Nesjavellir; Franzson (1988) suggested the possibility that these could be at least partly derived from the Grensadalur central volcano. Stratigraphic cross-sections reveal that sporadic hyaloclastite formations can still be found within the thick lava sequences of Nesjavellir below ~300 m b.s.l., extending to roughly 900-1500 m b.s.l. (Franzson, 1988). This corresponds well with the thick lava series identified at Hellisheidi around this depth that has been interpreted as the base of the Hengill volcano. The thickness of the hyaloclastites is greater in Hellisheidi than Nesjavellir, extending to ~1000-1400 m b.s.l. (Helgadóttir et al., 2010) as compared to ~300 m b.s.l. (Franzson, 1998); in addition to suggesting that volcanism has been more intense in Hellisheidi, this discrepancy led to the current estimate for the age of the Hengill central volcano of >0.4 my, revised from a prior estimate of <0.3 my based on Nesjavellir (Franzson et al., 2005). These fine- to medium-grained lava flows are the subaerial equivalent of the hyaloclastite units, and thus exhibit a similar range of compositional variability. Porosity is generally lower in lava flows, controlled primarily by the degree of magma degassing rather than the fragment size in the
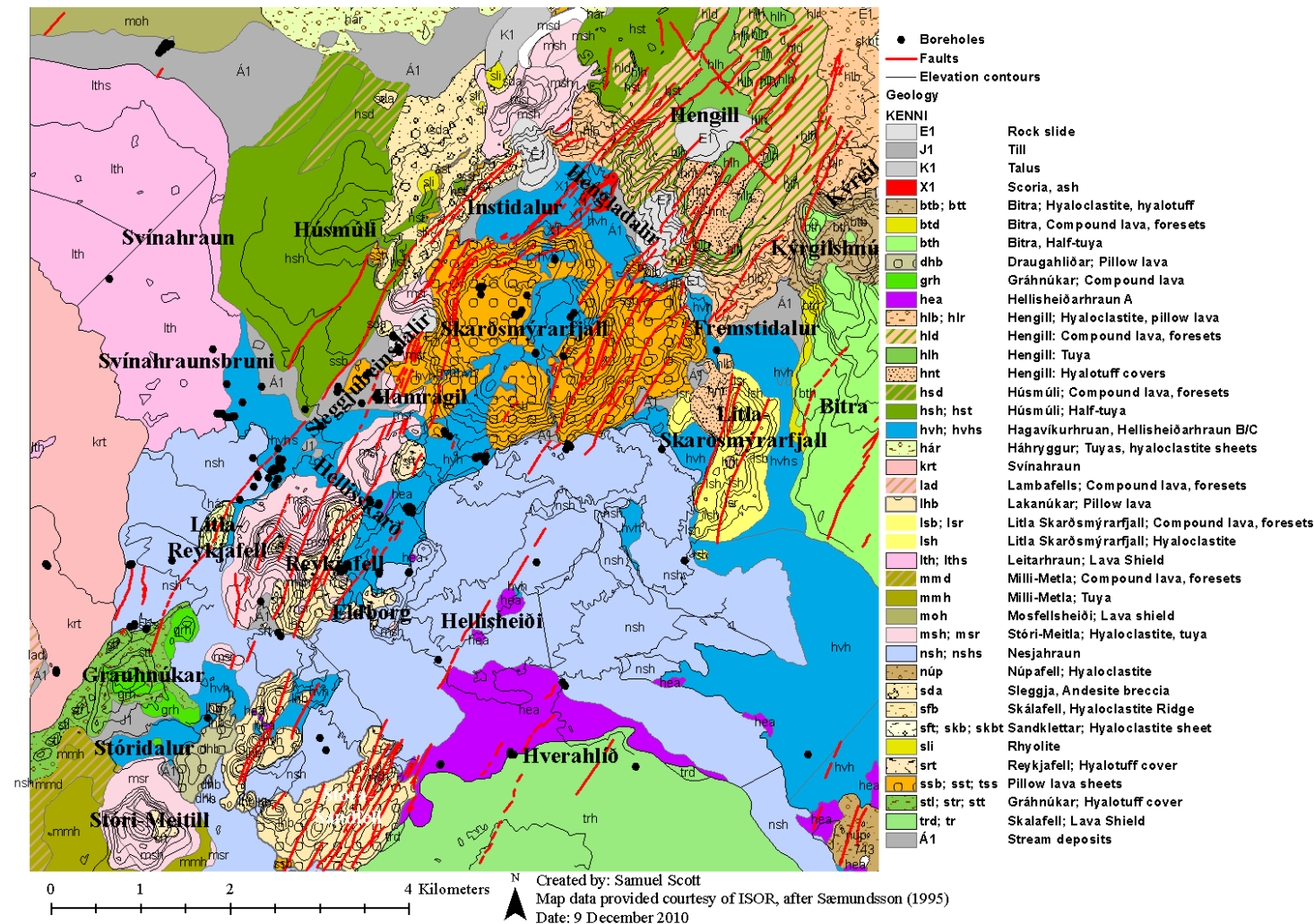
Figure 2.3: Geologic map of the Hellisheidi sub-field, showing lithologic units, surface fault traces, locations of boreholes, and elevation contours (contour interval = 10 m). Prepared in ArcMap using data obtained from ISOR. Classifications modified slightly after Saemundsson (1995a).

pyroclastic hyaloclastites, as well as the extent of alteration (Franzson et al., 2001). The locations of producing aquifers are often closely linked to stratigraphic boundaries between lava flow and hyaloclastite units.

Postglacial volcanism at Hengill has been confined to three fissure eruptions referred to as the Hellisheidihraun, Hagavíkurhraun and Nesjahraun, dated at ~10,300, ~5,700 and ~1,800 years b.p., respectively (Sinton et al., 2005). Additionally, two other post-glacial lava units – the Svinahraun (~1000 A.D.) and Leitahraun (~5200 b.p) - are located on the western margin of the Hengill graben. The geologic map in Figure 2.3 shows that these post-glacial lavas are major rock units observed in the Hellisheidi area. In the case of the Hagavíkurhraun and Nesjahraun, a lava of olivine tholeiitic composition was erupted from two nearly coincident ~10 km long, NNE oriented fissures, separated by a 9 km gap corresponding with the central part of Mt. Hengill. In the former eruption, approximately 0.4 km^3 was erupted over an area of ~41 km^2, much of which may have been overflowed by the younger Nesjahraun (Saemundsson, 1992), in which ~0.4 km^3 was erupted over an area of approximately 38 km^2 (Sinton et al., 1995). These fissure eruptions have been suggested to open up new flow paths and locally intensify the geothermal system (Franzson et al., 2010), and as potential major outflow zones for the field have been the main targets of drilling efforts, along with the faults bounding the western edge of the Hengill graben

Although intrusive activity has been intensively studied at Nesjavellir by Franzson (1988, 1998), similarly detailed analysis from Hellisheidi is still forthcoming. At Nesjavellir, intrusives are scarce above 400 m b.s.l. but rapidly increase in intensity to ~20% around 1000 m b.s.l., 40% by 1200-1400 m b.s.l., and 80-100% by 1500-1600 m b.s.l. Distinction was made between three types of intrusions: shallow dipping 10-12 m thick intermediate-to-acid dykes, interpreted as representing an early intrusive phase linked to low-volume acidic extrusives observed at Húsmúli; <6 m thick, altered basaltic dykes, which made up the majority of the intrusions below 1.5 km depth; and relatively unaltered basaltic intrusions that represented the near-surface extensions of the sheeted dyke complex. The fracture networks created by the emplacement of dioritic dykes and fresh basaltic intrusions were described as a major control on aquifer permeability below 400 m b.s.l.; permeability around the altered basalt intrusions was noticeably lower than the latter two types (Franzson, 1988). Preliminary evidence from Hellisheidi suggests intrusions become very common below 1500-1600 m b.s.l., consisting of sub-vertical sheeted dyke complexes composed of mostly fine-grained basalts with minor more evolved rock types, similar to Nesjavellir (Gunnarsson and Kristjánsson, 2003; Franzson et al., 2010).

Water-rock interaction at elevated temperatures leads to hydrothermal alteration, an irreversible process where unstable primary rock-forming minerals are continuously dissolved and less-soluble secondary minerals precipitate in their place. Numerous studies have suggested that fluid-mineral equilibrium in high-temperature fields (>150°C) is attained for all major components except Cl and B (ex. Arnórsson et al., 1983a); in Icelandic basalt, equilibrium has been demonstrated at temperatures as low as 40°C (Arnórsson and Andrésdóttir, 1995). The alteration mineralogy is subject to the influence of a variety of factors, including the system age, temperature, the supply of acids to the system (mainly reactive gases), the reactivity of the primary rock forming minerals, the contact area between water and rock, the concentrations of soluble salts in the rocks and the water through-flow rate (Arnórsson and Andrésdóttir, 2000). Commonly encountered mineral assemblages have been grouped into five basic depth and temperature related alteration zones. The smectite-zeolite zone (1), initiated around 40°C, reflects the alteration of the most unstable primary minerals, namely volcanic glass and olivine, into smectite

clays (Fe-rich saponites) and a variety of low-temperature Ca-Si zeolites including scolesite, analcime, mesolite and stilbite (Kristmansdóttir, 1979). The mixed-layer clay zone (2) is defined by the point at which smectite starts to become unstable (~200°C) and is gradually replaced by an interstratified smectite-chlorite (Schiffman and Fridleifsson, 1991). The underlying chlorite zone (3) is characterized by the presence of discrete chlorite, which begins to form around 230°C (Kristmansdóttir, 1979). The chlorite-epidote zone (4) correlates with the first appearance of epidote, believed to form at temperatures exceeding 230-250°C. Other temperature dependant minerals associated with the latter three zones include the high-temperature zeolite wairakite (>200°C), prehnite (>240°C) and wollastonite (>260°C). The first appearance of the amphibole actinolite, formed by the alteration of pyroxene at temperatures exceeding 280°C, defines the epidote-actinolite zone (5). At Nesjavellir, grossular garnet has also been sporadically identified within these zones (Steingrímsson, 1986), and at the deepest, hottest parts (>350°C), an Al-bearing amphibole (hornblende) has been found (Hreggvidsdóttir, 1987). In addition to the minerals described above, pyrite is widespread across the entire temperature range, its abundance believed to be controlled by the system permeability and supply of H_2S (e.g. Gunnlaugsson, 1977). Calcite is also abundant in well-cuttings, with its stability extending to temperatures around 290-300°C. Chalcedony and amorphous silica are observed at temperatures below 180°C, but at higher temperatures crystalline quartz is formed (Arnórsson, 1995). Other secondary minerals that are typically identified in high-temperature geothermal systems in Iceland include pyrrhotite, chalcopyrite, sphalerite, apatite, titanite and hedenbergite (Arnórsson, 1995).
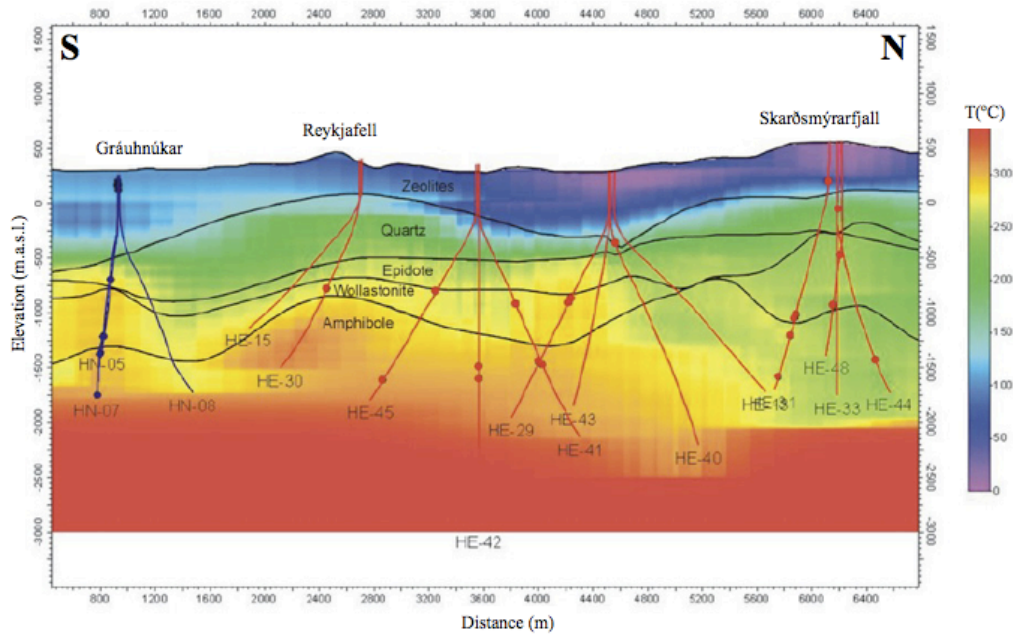
Figure 2.4: A northeast-southwest oriented cross-section through the center of the Hellisheidi subfield, showing depth to first appearance of select temperature dependent alteration minerals (zeolites, quartz, epidote, wollastonite, amphibole). Formation temperature is interpreted from downhole measurements. Modified after Helgadóttir et al. (2010).

Helgadóttir et al. (2010) described the depth-zonal distribution of some of the main temperature dependant alteration minerals thoughout the Hellisheidi subfield – quartz (>180°C), epidote (>230-250°C), wollastonite (>260°C), and Al-free amphibole (>280°C). A north-south cross-section spanning the Hellisheidi field from Gráuhnúkar to Skardsmýrarfjall showing the depth to first appearance of these minerals is displayed in Figure 2.4. The cross-section shows that most high of these minerals are encountered at shallowest depths (1000 m b.s.l.) beneath Reykjafell and Skardsmýrarfjall. In general, formation temperatures are in excess of temperatures inferred from alteration mineralogy throughout the cross-section displayed in Figure 2.4. The zone of recent heating is nearly coincident with the western margin of the Holocene fissure eruptions, suggesting that the associated dykes may have opened up highly permeable fractures that acted as new up- or out- flow paths for the fluid (Franzson et al., 2010). The eastern and western flanks of Skardsmýrarfjall, Stóra Reykjafell and the Bitra subfield all appear to be affected by thermal mining at a depth of 1000-1500 m b.s.l.; Franzson et al. (2010) attributed this to enhanced permeability resulting from fracturing related to the SISZ allowing an influx of lower-temperature hydrothermal fluid, which was stronger throughout the northeastern part of the Hellisheidi field.

2.3 Fluid Chemistry

The chemical composition of aqueous fluids and gaseous steam in a geothermal fluid not only reflect thermal conditions at depth, but can also be used to improve the conceptual model of the reservoir by identifying the source of the fluid as well as zones of recharge, upflow and outflow (e.g. Arnórsson, 2000). While the chemistry of Hellisheidi fluids has been discussed to different extents in a number of studies (Stefánsson et al.,

2009; Remoroza, 2010; Mutonga, 2010; Arnórsson et al., 2010), in general, geochemical investigations have not caught up with the vigorous rate of drilling between 2003 and the present. Despite the lack of a thorough geochemical study of the Hellishedi geothermal field, a few prevailing characteristics of the geothermal fluids produced from Hellisheidi wells have emerged. In general accordance with observations from other non-saline Icelandic geothermal fields, these wells discharge dilute Na-Cl-HCO$_3$ type fluids, with total dissolved solids ranging from 1000-1500 ppm and Cl usually below 200 ppm (Mutonga, 2010). Isotopic studies have suggested that the source of Hellisheidi fluids is likely local precipitation. A limited number of analyses from high-temperature wells plot slightly to the left of the global meteoric water line, grouping around $\delta^{18}O$ and δ^2H values ranging from -7.3‰ to -6.5‰ and -62‰ to -65‰, respectively (Mutonga, 2010). In contrast, the fluid source for the Nesjavellir subfield is Lake Thingvallavatn to the north. Additionally, fluid produced in Nesjavellir is richer in ^{18}O and chemically more mature than Hellisheidi, suggesting more intense water-rock interaction.

Early studies of gas geochemistry in the Hengill area were performed using fumarole discharges, and involved the application of gas geothermometers to try to estimate reservoir temperatures (Ívarsson, 1998; Arnórsson and Gunnlaugsson, 1985). Although geothermal surface manifestations (including fumaroles) are generally scarce in the Hellisheidi area as indicated by Figure 2.2, the few discharges present were taken to indicate reservoir temperatures in the Hellisheidi and Nesjavellir areas in excess of 320°C. A decline in temperatures approaching 200°C was observed towards the east. Ívarsson (1998) was the first to clearly delineate the three different volcanic centers on the basis of chemical evidence, corresponding with the three systems mentioned in Section 2.1.

More recent analyses of produced fluids from Nesjavellir (Arnórsson et al., 1995; Giroud, 2008) and Hellisheidi (Remoroza, 2010; Arnórsson et al., 2010) have provided a more detailed view of aquifer fluid compositions. In general, there is marked variability in reactive gas concentrations which will be revealed in greater detail below. The concentrations of H$_2$S and H$_2$ in the initial aquifer fluid have been suggested to maintain close equilibrium with specific mineral-gas buffers, described below. Slightly elevated concentrations of these gases relative to equilibrium were taken to indicate a small initial vapor fraction, less than 0.5% by mass (Arnórsson et al., 2010). However, as will be discussed in detail later, the model used to determine deep-water compositions has a big effect on the calculated gas concentrations in initial aquifer fluids. Therefore, although the raw chemical analyses performed by the aforementioned studies of the Hellisheidi field will be retained in this study to provide a larger sample size, initial aquifer fluid chemical compositions will be recalculated.

2.4 Summary

Previously, the conceptual model of the geothermal system at Hengill implied a common upflow zone for both the Nesjavellir and Hellisheidi subfields located beneath the Hengill massif (e.g. Franzson et al., 2005; Björnsson et al., 2006). Based largely on this model, recent drilling efforts focused on the northern part of the Hellisheidi field, with many wells directionally drilled from the northern margin of Skardsmýrarfjall towards to the north in an attempt to tap hot upflowing fluids. However, downhole measurements indicated lower formation temperatures (200-250°C) than expected, and many of the wells were deemed insufficient to bring into production. Figure 2.5 displays formation temperatures at 1 km b.s.l. estimated from down-hole measurements, as well as across SSW-NNE and NWW-SEE cross sections through the main parts of the field. Figure 2.5

indicates a strong likelihood of at least two, and possibly as many as four, distinct upflow zones of fluid at temperatures >300°C. As will be described in later sections, currently producing wells analyzed in this study tap deep aquifers associated with two of these potential upflows: one located on the southern end of Skardsmýrarfjall towards the eastern margin of the graben (on the left side of cross section A-A'), and another beneath Reykjafell on the western margin of the graben, nearly coincident with the locations of the eruptive fissures from which the Hagavíkurhraun and Nesjahraun post-glacial lavas were erupted (towards the center of cross-section B-B'). In the case of the former, temperature profiles suggest a relatively broad, vertically-oriented upflow, with some heterogeneity in terms of the distribution of regions in excess of 300°C. In the case of the latter, a relatively narrow upflow is identified, with a pronounced reversal in temperature gradients to the north of this area and especially to the west. The reversal in temperature is suggestive of deep recharge associated with a convection cell. Alternatively, this could be explained by strong lateral discharge of upflowing fluids to the south, along the axis of the graben (Björnsson et al., 2003). In addition to the upflow zones mentioned above, temperature profiles reveal high temperatures in the Gráuhnúkar area to the south, currently being used for reinjection (Hardason et al., 2010), and in the proximity of a small fissure swarm in the Hverahlíd area to the east (Níelsson and Franzson, 2010).

The heat sources for geothermal activity at Hengill are associated with the sheeted dyke complex, or possibly also sills and stock-shaped intrusions, whose distribution becomes less homogenous the closer one approaches the surface. Large regions of partial melt are unlikely. Heat transfer from the cooling, crystalline intrusions is dominated by a thin zone of conduction, on the order of tens of meters (Arnórsson et al., 2007). The velocity and resisitivity anomalies underlying Hengill are believed to be caused by convecting 'supercritical' fluids within ductile, gabbroic intrusive bodies (Foulger et al.,
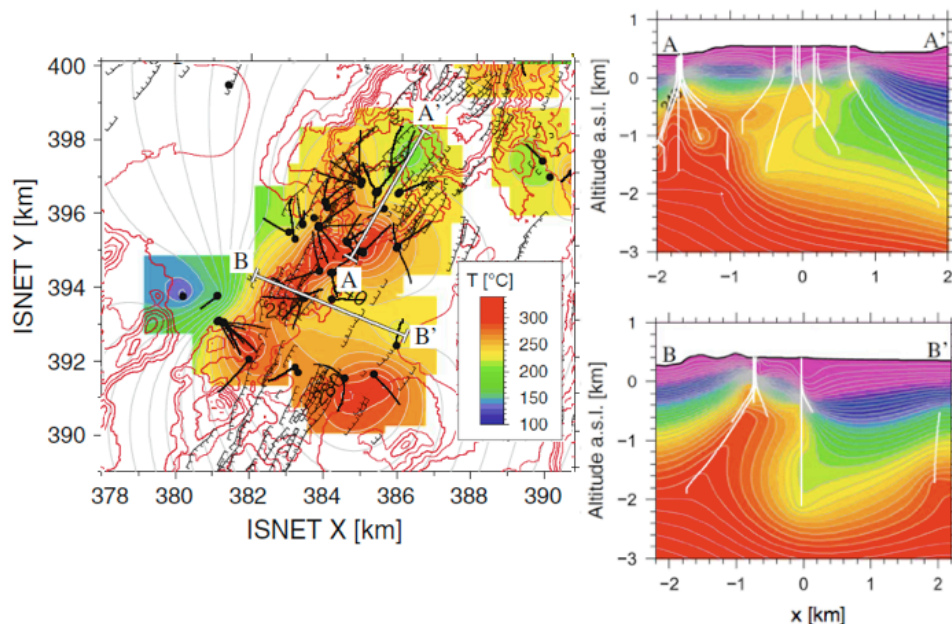
Figure 2.5. Temperature distribution in the Hellisheidi area as determined from downhole measurements. Figure at left displays formation temperature at 1000 m b.s.l. Thick black dots and lines represent well locations and tracks, thin black lines surface fault traces, red lines elevation contours and thick white lines locations of cross-sections displayed at right. White lines in figure at right represent well tracks. Modified after Gunnarsson et al. (2010).

14

1995; Tryggvason et al., 2002). If the rock cools sufficiently or the critical stress is overcome, sub-vertical fractures may form in the intensely strained rock, releasing gas-rich 'supercritical' fluids to shallower depths. Overlying the ductile rock is a separate and more extensive thermal regime with much lower temperatures (280-320°C). Interaction between the two zones would be limited, perhaps restricted to the kind of periodic input from below described above. The source of convecting fluid in the upper zone is meteoric water, whose temperature generally follows the boiling point curve with depth. Any vapor formed in the initial aquifer fluid would likely be minor, dependent on the rate of heat input into the system relative to recharge.

The sub-vertical, sub-parallel fractures associated with the axial rift zone serve as the main flow paths. If the hot fluid finds a path to the surface somewhere along these outflow zones, fumarole discharges, boiling hot springs and regions of thermally altered ground can be expected. Alternatively, if the fluid conducts a sufficient amount of heat to the surface or mixes with cold meteoric waters, it would begin to percolate downwards into the reservoir as part of the convection cell. As the percolating fluid is dominantly composed of air-saturated meteoric water, it would be expected to be relatively rich in N_2 and Ar, since these atmospherically-derived components are lost from meteoric waters after boiling in the geothermal system, and low in Cl, a conservative component derived mainly from rock dissolution.

The areas that the present study hopes to address may be summed up as follows: Where are the locations of upflow and recharge zones in the Hellisheidi geothermal reservoir? How are they manifested in the chemical compositions of fluids produced from geothermal areas? Where are the main areas in which upflow, outflow and recharge are occurring? Based on these considerations, what should be the main drilling targets in the future?

3 Methodology

Two principle steps are required to determine the chemical composition of aquifer fluids. The first involves sampling, treatment and chemical analysis of surface well discharge fluids. Secondly, initial aquifer fluid chemical compositions must be calculated based on a model for boiling and potential causes of the observed discharge enthalpy (in the case of excess enthalpy wells). This section describes the methods taken to complete these steps and focuses attention on the mathematical foundation for calculation of aquifer fluid chemical compositions. Additionally, the theoretical basis for different quantitative measures used to describe aquifer fluids is explained. Since the significance of results depends on the manner used to generate them, it is essential to explain and justify all aspects of the methodology.

3.1 Sampling and Analysis

The primary data used in this study were obtained from 18 samples of wet-steam well discharges obtained on 5 different days between March and September 2010. These samples are supplemented by 6 samples collected in February 2009 (Stefánsson et al., 2009), as well as 9 samples collected in October and September 2008 (Remoroza, 2010). Between these three data sets, 21 wells currently in production are represented, two of the wells three times (HE-06, HE-17) and eight wells twice (HE-03, HE-05, HE-07, HE-11, HE-12, HE-18, HE-29, HE-41). The sample locations are shown in Figure 3.1. Surface well discharge samples were collected using a webre separator. For the samples specifically collected for the present study, the steam phase of the discharge was sampled into a 125 or 250 ml glass sampling bulb with a stopcock at both ends. The atmospheric gases were expelled from the sampling bulb by allowing steam from the well to flow through the bulb for ~5 minutes. Afterwards, 5 or 10 ml of 50% w/v KOH (depending on the size of the bulb) was introduced into the bulb through a septum on the side of the bulb using a needle and a syringe for the purpose of dissolving the CO_2 and H_2S in the condensate, enriching the other gases (H_2, N_2, Ar and CH_4) in the gas phase of the sample bulb, thus making their analysis more precise. Other steam samples were collected into pre-evacuated 250 ml sampling bulbs containing 10 ml of 50% w/v KOH-solution. Liquid phase samples were cooled down in-line using a stainless steel spiral and filtered through a 0.2 μm cellulose acetate filter for most components. The samples were treated in various ways depending on component to be analyzed and analytical methods. Dissolved sulfide was titrated on-site in unfiltered samples. Samples for determination of dissolved inorganic carbonate were collected into amber glass bottles for analysis in the laboratory. Samples for major anion determination, Si and B were filtered into polypropylene (PP) bottles for later IC analysis, and samples for major cation determination were filtered into PP bottles and acidified (0.5 ml 67% HNO_3, Merck Suprapur®, into 100 ml sample) for later ICP-OES analysis. Samples for SO_4 analysis were treated with 0.1 M $Zn(CH_3COO)_2$, 2.5 ml in 100 ml sample and subsequently analyzed by IC. For further description of the methods the reader is referred to Arnórsson et al. (2000) and Arnórsson et al. (2006).
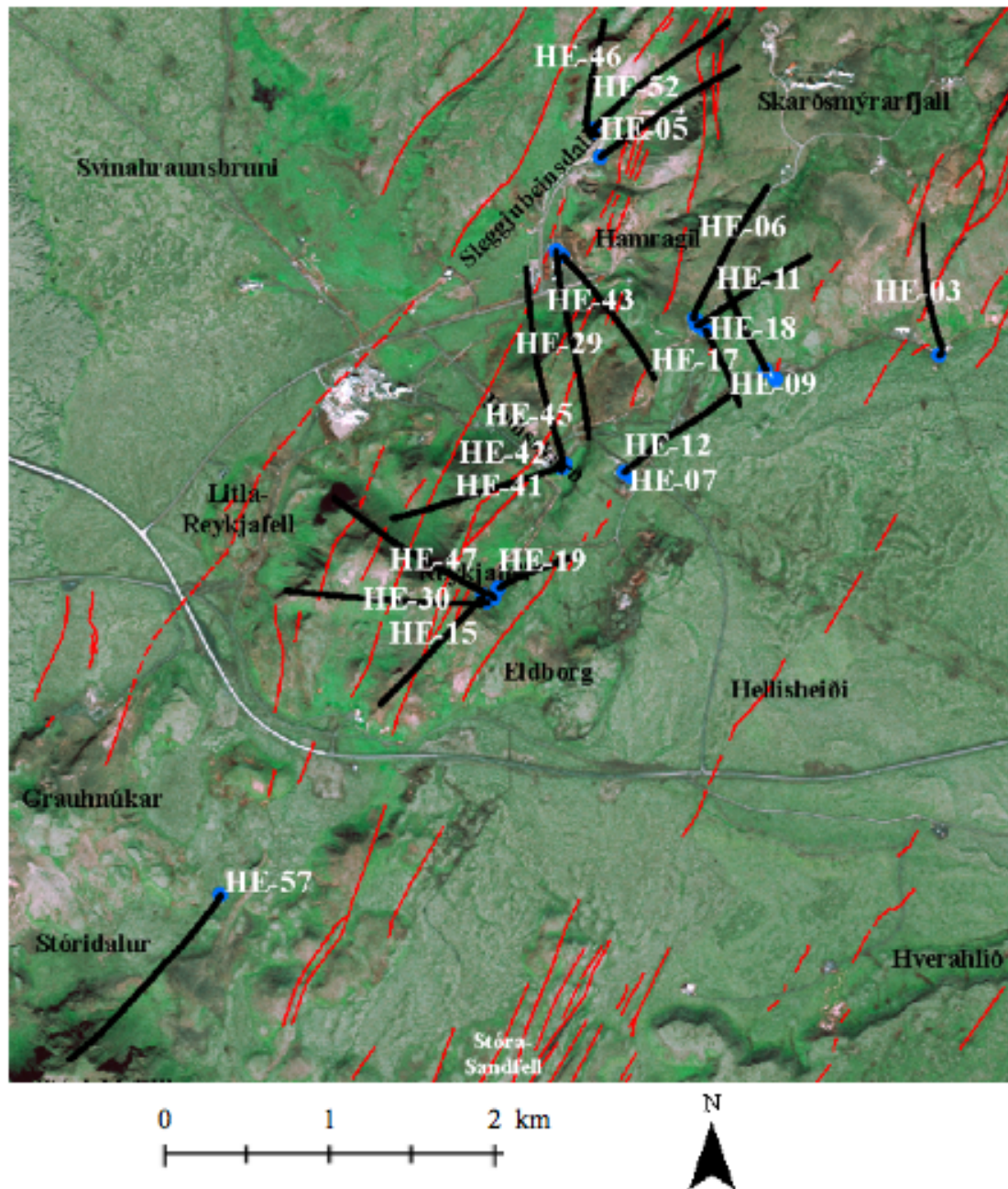
Figure 3.1: Locations and names of wells sampled in this study. Blue dots represent location of well heads, black lines the paths of directionally drilled wells. Red lines represent surface faults.

18

Table 3.1: Summary of analytical methods used for liquid and steam phase samples and precision obtained for duplicate (liquid phase) or replicate (steam phase) samples.

Component	Analytical Method	Measured Concentration Range (ppm)	Mean % Deviation[a]	Standard Deviation[b]
Liquid Phase				
CO_2	Titration	9.96-87.8	4.8	3.4
H_2S	On-site titration	22.9-75.1	1.0	0.7
Si	ICP-OES	626-1012	0.5	0.27
B	ICP-OES	0.38-2.52	0.9	0.5
Na	ICP-OES	137.9-256.9	0.9	0.6
K	ICP-OES	25.5-47.8	0.6	0.3
Ca	ICP-OES	0.22-1.29	2.4	1.9
Mg	ICP-OES	<0.001 - 0.0065	16.7	11.2
Fe	ICP-OES	<0.005-0.072	4.4	2.9
Al	ICP-OES	1.19-2.01	0.5	0.4
Cl	IC	101.3-205.0	0.5	0.2
SO4	IC	6.3-19.1	0.9	0.5
F	IC	0.5-1.4	2.7	1.4
Steam Phase				
CO_2	Titration	1191-7259	4.1	1.6
H_2S	Titration	190-1183	4.6	2.4
H_2	GC	0.6-68.7	3.8	2.3
CH_4	GC	0.6-15.2	4.7	2.9
N_2	GC	14.6-577	10.6	6.2
Ar	GC	0.38-19.39	17.4	9.1

[a] Mean percentage difference between duplicate/replicate determinations
[b] Standard deviation of mean percentage deviation.

Table 3.2: Collected liquid phase analyses for all samples utilized in this study. Hyphen indicates no data available due to steam-contamination. All component concentrations are given in ppm.

Date	Sample #	Well	$h^{d,t}$ (kJ/kg)	p^s (bar-g)	p^{wh} (bar-g)	pH/°C	TCC[a]	TSS[b]	B	SiO_2	Na	K	Mg	Ca	F	Cl	SO_4	Al	Fe
27.05.2010	10-5079	HE-47	2139	11.0	24.0	8.14/20.9	46.7	22.9	1.804	1009.7	148.4	36.3	0.0013	0.27	1.07	202.5	6.4	1.58	0.0080
27.05.2010	10-5080	HE-19	1599	10.7	20.2	8.80/22.6	10.0	66.8	1.197	632.3	196.4	31.2	0.0013	0.58	1.06	186.6	8.2	1.53	0.0151
01.06.2010	10-5081	HE-30	2173	9.6	16.1	8.25/21.9	22.1	35.0	1.450	974.4	164.2	36.0	0.0011	0.34	1.06	202.6	9.7	1.60	0.0093
01.06.2010	10-5082	HE-15	1597	9.8	22.5	8.79/19.7	16.4	55.5	1.129	683.9	181.9	30.0	0.0019	0.49	1.07	167.0	9.6	1.56	0.0082
04.06.2010	10-5083	HE-17	2054	9.5	21.8	8.48/22.6	13.7	64.5	1.484	783.5	188.6	36.6	0.0037	0.32	1.09	205.0	12.0	1.71	0.0145
04.06.2010	10-5084	HE-11	2047	9.6	19.0	8.71/21.5	47.4	52.1	1.065	744.4	172.7	32.9	0.0016	0.22	0.97	161.2	11.9	2.01	0.0065
04.06.2010	10-5085	HE-06	1548	9.6	18.5	8.67/22.5	87.8	57.3	0.666	627.8	161.5	25.7	0.0063	0.49	1.02	101.4	9.1	1.93	0.0703
07.06.2010	10-5086	HE-46	1177	8.0	16.0	9.26/21.5	29.5	33.3	0.387	668.3	177.2	30.8	0.0030	0.52	1.16	62.8	42.5	1.96	0.0153
07.06.2010	10-5087	HE-52	1169	4.0	9.6	9.22/27.1	20.1	26.4	0.478	678.2	178.2	28.5	0.0012	1.27	1.44	77.6	30.5	1.87	0.0076
27.08.2010	10-5163	HE-18	1385	10.1	13.7	8.92/21.4	34.9	52.0	0.879	678.0	170.2	29.5	0.0007	0.31	0.98	143.6	19.7	1.90	<0.005
27.08.2010	10-5164	HE-09[d]	2757	10.5	13.0	7.25/186.1	29.4	74.7	2.665	819.2	171.5	34.6	0.0100	1.18	0.89	204.0	-	1.20	0.1412
27.08.2010	10-5165	HE-57	1043	6.2	12.5	9.14/20.0	46.7	50.9	1.059	742.8	195.3	36.4	0.0005	0.99	0.50	154.8	19.1	1.57	<0.005
27.08.2010	10-5166	HE-03	1216	11.3	12.7	8.80/20.4	10.0	45.3	1.083	664.6	255.3	47.7	0.0004	0.73	0.87	362.2	11.1	1.19	<0.005
16.09.2010	10-5168	HE-12	1746	10.2	19.5	8.66/24.0	22.1	73.4	1.330	783.3	193.2	36.7	<0.001	0.32	0.95	193.2	17.9	1.90	0.0072
16.09.2010	10-5169	HE-07	1372	10.2	21.0	8.89/23.7	16.4	73.6	1.235	636.3	197.9	33.2	<0.001	0.36	1.13	185.4	8.3	1.68	<0.005
16.09.2010	10-5170	HE-45[c]	2498	10.0	24.5	-	-	-	2.514		27.5	5.4				178.5	-		
20.09.2010	10-5171	HE-42	2489	10.1	24.5	8.35/18.5	13.6	35.0	2.501	874.2	138.6	30.0	0.0014	0.24	1.35	168.6	3.1	1.75	0.0224
20.09.2010	10-5172	HE-41[c]	2704	10.2	24.5	-	-	-	0.533		22.6	4.9				25.7	-		
02.02.2009	09-5189	HE-43	1466	4.6	16.1	8.42/24	33.0	50.0	1.536	877.0	142.7	28.1	0.0016	1.05	1.10	90.2	10.6	2.29	0.0100
02.02.2009	09-5190	HE-05	1194	10.8	17.0	9.20/22	66.8	46.0	0.407	676.0	160.6	29.1	0.0008	0.40	1.72	77.1	16.2	1.91	<0.01
09.02.2009	09-5198	HE-06	1548	11.6	16.0	8.70/23	74.8	60.1	0.685	613	159.8	25.4	0.0013	0.49	0.70	104.3	11.3	1.87	<0.01
09.02.2009	09-5199	HE-17	2319	12.5	25.0	8.37/23	15.4	68.7	1.639	786.0	189.9	37.3	0.0016	0.35	0.78	215.6	5.6	1.69	<0.01
09.02.2010	09-5197	HE-29	2399	11.0	20.5	8.67/22	18.1	52.1	5.631	885.0	132.1	27.6	0.1350	0.59	1.61	105.1	2.8	2.35	0.0420
09.02.2009	09-5200	HE-41[c]	2704	12.2	17.0	8.70/15	93.3	57.6	1.016	710.0	71.7	14.7	0.0046	0.17	1.05	40.7	2.9	2.29	0.0370
08.10.2008	08-3001	HE-07	1372	8.5	20.0	9.13/17	7.38	76.1	1.230	659.0	201.0	32.7	0.0120	0.35	1.10	199.0	7.5	1.74	0.0110
08.10.2008	08-3002	HE-12	1746	9.5	17.0	8.66/19	11.0	77.4	1.360	816.0	188.0	35.5	0.0050	0.28	1.26	196.0	13.7	1.90	0.0300
08.10.2008	08-3003	HE-17	2319	10.0	20.8	8.47/17	10.6	68.0	1.470	796.0	177.0	36.2	0.0020	0.27	1.00	207.0	5.5	1.68	0.0090
08.10.2008	08-3004	HE-11	2047	9.5	18.0	8.74/17	22.9	55.7	1.040	754.0	168.0	31.8	0.0010	0.17	1.08	158.0	8.6	2.03	0.0240
09.10.2008	08-3005	HE-29	2399	15.0	20.8	8.71/21	11.9	57.5	5.920	931.0	128.0	25.7	0.0020	0.23	1.89	104.0	3.9	2.17	0.0050
09.10.2008	08-3006	HE-05	1194	8.8	16.2	9.42/20	33.1	37.7	0.400	698.0	157.0	27.9	0.0004	0.32	2.08	77.0	19.2	2.01	0.0110
10.10.2008	08-3007	HE-06	1548	9.5	18.0	8.82/21	34.5	56.9	0.680	633.0	160.0	24.9	0.0006	0.37	0.91	107.0	10.4	1.95	0.0040
10.10.2008	08-3008	HE-03	1396	9.8	13.0	8.81/19	4.3	24.3	1.010	670.0	246.0	45.9	0.0003	0.72	0.84	354.0	11.4	1.21	0.0160
10.10.2008	08-3009	HE-18	1385	9.4	15.2	8.97/19	18.9	57.9	0.840	682.0	165.0	27.6	0.0010	0.31	1.16	144.0	8.8	1.93	0.0060

[a] TCC = Total carbonate carbon, expressed as ppm CO_2

[b] TSS = Total sulfide sulfur, expressed as ppm H_2S

[c] 'Dry steam' wells. Uncontaminated liquid phase could not be obtained. Analyses of Na, K and B, Cl shown for ratio determination.

[d] 'Dry steam' well. Liquid phase from 24/06/2004 sample (Ingvi Gunnarsson, pers. comm.), recalculated at new discharge enthalpy and sampling pressure.

Table 3.3: Collected gas phase analyses for all samples analyzed in this study. All component concentrations are given in mmol kg^{-1}.

Date	Sample #	Well	CO$_2$	H$_2$S	H$_2$	CH$_4$	N$_2$	O$_2$	Ar	N$_2$/Ar
27.05.2010	10-5079	HE-47	51.83	22.51	14.13	0.120	0.771	0.0000	0.0161	47.97
27.05.2010	10-5080	HE-19	52.40	25.54	15.89	0.132	0.575	0.0000	0.0141	40.75
01.06.2010	10-5081	HE-30	84.90	25.39	14.06	0.176	0.749	0.0000	0.0158	47.36
01.06.2010	10-5082	HE-15	83.17	24.14	9.27	0.207	1.990	0.0175	0.0311	63.90
04.06.2010	10-5083	HE-17	66.76	36.07	27.92	0.208	0.919	0.0000	0.0258	35.58
04.06.2010	10-5084	HE-11	98.89	21.62	17.62	0.232	1.013	0.0000	0.0278	36.44
04.06.2010	10-5085	HE-06	172.39	21.22	17.83	0.191	1.129	0.0000	0.0264	42.74
07.06.2010	10-5086	HE-46	96.72	6.03	0.33	0.432	7.429	0.0000	0.1553	47.85
07.06.2010	10-5087	HE-52	89.13	3.48	1.00	0.949	16.340	0.0000	0.5547	29.46
27.08.2010	10-5163	HE-18	55.32	18.76	12.81	0.410	2.503	0.0000	0.0441	56.75
27.08.2010	10-5164	HE-09	58.92	41.41	28.69	0.062	0.523	0.0000	0.0149	35.19
27.08.2010	10-5165	HE-57	65.98	11.88	1.20	0.477	9.084	0.0000	0.2200	41.28
27.08.2010	10-5166	HE-03	22.67	11.67	1.14	0.124	9.659	0.0000	0.1597	60.49
16.09.2010	10-5168	HE-12	56.89	27.38	18.32	0.227	0.922	0.0000	0.0191	48.26
16.09.2010	10-5169	HE-07	37.22	22.12	12.97	0.188	7.646	0.0047	0.0937	81.63
16.09.2010	10-5170	HE-45	40.57	25.11	13.69	0.036	0.563	0.0000	0.0143	39.45
20.09.2010	10-5171	HE-42	17.22	30.22	19.28	0.066	0.694	0.0000	0.0183	37.94
20.09.2010	10-5172	HE-41	48.24	22.57	14.99	0.043	0.540	0.0000	0.0110	49.15
02.02.2009	09-5189	HE-43	88.30	28.32	13.11	0.254	20.590	0.0000	0.2452	83.97
02.02.2009	09-5190	HE-05	83.40	7.19	0.31	0.423	4.820	0.0000	0.0706	68.27
09.02.2009	09-5198	HE-06	163.00	21.56	10.91	0.150	0.950	0.0000	0.0141	67.38
09.02.2009	09-5199	HE-17	63.40	46.54	25.35	0.154	1.180	0.0000	0.0184	64.13
09.02.2009	09-5197	HE-29	58.00	32.77	20.35	0.348	7.680	0.0000	0.1036	74.13
09.02.2009	09-5200	HE-41	45.00	21.22	12.84	0.046	1.960	0.0000	0.0234	83.76
08.10.2008	08-3001	HE-07	29.74	24.12	12.98	0.247	3.300	0.0000	0.0540	61.11
08.10.2008	08-3002	HE-12	52.84	33.65	24.68	0.342	10.060	0.0000	0.1460	68.90
08.10.2008	08-3003	HE-17	71.83	47.14	33.98	0.283	10.350	0.0000	0.1360	76.10
08.10.2008	08-3004	HE-11	99.36	27.92	21.38	0.356	6.740	0.0000	0.0910	74.07
09.10.2008	08-3005	HE-29	55.58	27.29	17.96	0.177	1.480	0.0000	0.0300	49.33
09.10.2008	08-3006	HE-05	80.86	6.17	0.61	0.660	8.880	0.0000	0.1480	60.00
10.10.2008	08-3007	HE-06	155.23	19.19	13.86	0.216	1.640	0.0000	0.0290	56.55
10.10.2008	08-3008	HE-03	9.56	3.11	0.77	0.074	1.150	0.0000	0.0190	60.53
10.10.2008	08-3009	HE-18	64.82	18.09	12.12	0.446	4.920	0.0000	0.0660	74.55

All samples were analyzed in duplicate. A summary of the analytical methods and the precision of duplicate/replicate analyses for each component is provided in Table 3.1. For the steam phase, the values reported in Table 3.1 represent the precision between two separate samples taken consecutively on-site, while those for the liquid phase represent duplicate analysis of the same sample. The largest uncertainty in steam phase analyses due to slight variations in the relative volumes of gas and condensate collected for replicate samples. For duplicate analyses of steam samples by gas chromatography (GC), precision is generally very high for all components analyses (<1% mean percent deviation); for TCC and total H_2S, the precision of duplicate analyses is similar to what is reported for these components in the liquid phase.

For the liquid phase, total suphide sulfur (TSS) was determined on-site because of possible degassing and/or oxidation of H_2S upon storage using a precipitation titration method with standard $Hg(CH_3COO)_2$-solution and dithizone indicator. For total carbonate carbon (TCC), an unfiltered sample was collected in an amber pyrex glass bottle with specially designed taps to prevent entrapment of air and degassing and analyzed in the laboratory within 3-4 days by titration from pH 8.3 to 4.5 with 0.1 M HCl followed by degassing with N_2 for 10 minutes and back titration from pH 4.5 to 8.3 with 0.1 M NaOH. The pH was measured on-site and in-line at ~20°C using a flow-through cell. This was considered important as pH may change upon storage due to silica polymerization. The flow rate through the dual cooling coils was adjusted until temperature of the fluid at the electrode was approximately ~20°C, near the calibration temperature. Major anions were determined by ion chromatography (IC) in filtered untreated samples. Dissolved sulfate analyses were carried out separately from Cl^- and F^-, on $Zn(CH_3COO)_2$ treated samples. Major and minor cations (Al, B, Ca, Fe, K, Li, Na, Mg, Si) were determined by Inductively Coupled Plasma Optical Emission Spectroscopy (ICP-OES). All samples were analyzed in duplicate. The total liquid phase analyses are displayed in Table 3.2.

The concentrations of gases in the steam phase was analyzed using wet chemical methods and gas chromatography (GC) at the University of Iceland. The non-condensable gases (H_2, N_2, O_2, Ar and CH_4) were analyzed on a Perkin Elmer GC using two runs, the light gas analysis (LGA) for determination of H_2, CH_4, N_2, and O_2/Ar and argon analysis (AA) for determination of O_2, Ar and N_2. For most light gas analyses, the sum of the calculated percentages add up to within 5% of 100%, suggesting relatively high accuracy. TCC and TSS in the steam phase were determined in the condensate of the gas sampling bulb by the titration methods previously described for each component in the liquid phase, except that a back titration was not performed in the TCC determination. The complete gas phase chemical analyses are displayed in Table 3.3.

3.2 Modeling of Aquifer Fluid Compositions

Four of the twenty-one well discharges considered in this study have liquid enthalpy, i.e. the enthalpy of the discharge is the same (within the limit of measurement error) to that of steam saturated liquid at the aquifer temperature. The other wells display variable degrees of 'excess' enthalpy, with three of the wells considered discharging almost dry steam. For liquid enthalpy wells, it is a reasonable assumption to take the total well discharge composition to represent the initial aquifer fluid. For excess enthalpy wells, on the other hand, a model needs to be selected that explains the cause of the elevated well enthalpy by considering the effects of depressurization boiling, possible phase segregation in the depressurization zones around wells, conductive heat transfer from the aquifer rock to the flowing fluid that enhances boiling as well as loss of gaseous steam from the fluid
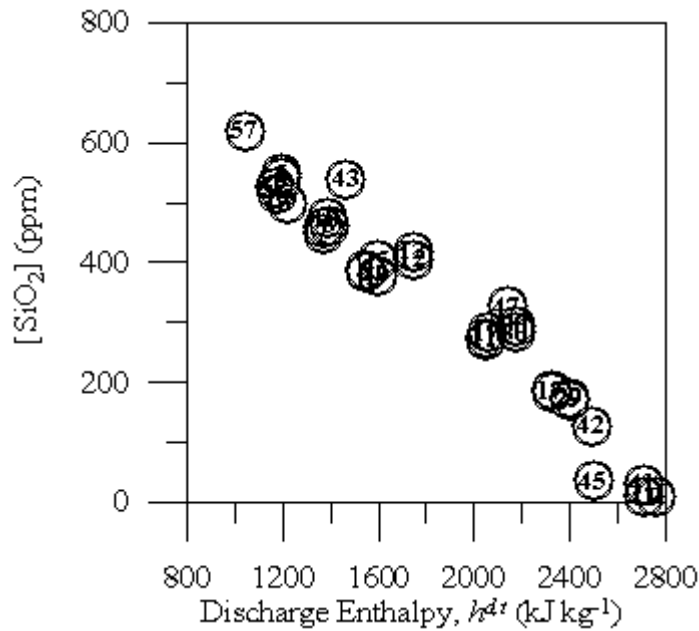
Figure 3.2. The concentration of SiO₂ (ppm) in the total discharge as a function of discharge enthalpy (kJ kg⁻¹).

flowing into wells, likely during horizontal flow. The basic models that have been considered were described by Arnórsson et al. (2007, 2010).

Stefánsson et al. (2009) and Arnórsson et al. (2010) concluded that the the excess enthalpies of well discharges at Hellisheidi collected in 2008 could be accounted for by phase segregation alone and conductive heat transfer from the aquifer rock to the fluid flowing into wells was insignificant. This was further substantiated by Remoroza (2010). The above conclusions were based on the observation that the concentrations of dissolved solid components, such as silica, decreased in total well discharges with increasing discharge enthalpy and approached zero as the discharge enthalpy approached that of dry steam (Figure 3.2). The same correlation is seen in the samples collected for this study in 2010. For that reason, the phase segregation model has been adopted to calculate initial aquifer fluid compositions for all Hellisheidi well samples. By the phase segregation model, the excess enthalpies of well discharges (steam to water ratio) is explained by the retention of liquid by the aquifer due to its adsoprtion onto mineral grain surfaces by capillary forces. All of the models considered by Arnórsson et al. (2007, 2010) assume that chemical reactions in the depressurization zones do not change fluid component concentrations, neither by mineral dissolution nor by precipitation. This appears to be a reasonable approximation for components present in high concentrations in the fluid. On the other hand, minor reactive components, such as Ca, Al and Fe may change their concentrations considerably in the fluid between undisturbed aquifer and wellhead. While the open system considers loss of liquid from the aquifer-well system, no gain or loss of chemical components due to mineral precipitation or dissolution is considered. Additional assumptions describing the nature of the initial reservoir fluid include the selection of a single "reference" temperature at which composition and speciation is calculated, as well as the presence (or lack thereof) of a vapor phase in the initial reservoir fluid. Due to the significant uncertainty associated with many of these assumptions, the approach chosen for this study is to calculate aquifer fluid compositions under a range of different assumptions and investigate the sensitivity of key conclusions to different assumptions.

To be able to calculate aquifer fluid compositions from wellhead data by the segregation model two parameters need to be selected, the pressure at which phase segregation occurs, symbolized as p^e and the temperature of the initial aquifer fluid T^f. The phase segregation model is discussed in some detail in the following section.

3.2.1 Phase Segregation

Geothermal reservoirs contain fluid consisting of liquid, vapor or a mixture thereof. In one-component, two-phase systems at equilibrium, the Gibbs phase rule dictates that only one independent variable is necessary to completely describe the system. In the production zone of a geothermal reservoir, this variable is pressure, specifically, the hydrostatic head exerted on the fluid mixture at a given depth. Upon entering the production zone of a discharging well, the pressure of the aquifer fluid is greatly reduced. In a liquid-dominated aquifer, this pressure drop may be insufficient to initiate boiling in the aquifer itself, and the depth level of first boiling takes place in the well, even in its cased portion. However, for fluids already near or on the boiling point, as in two-phase systems, intensive boiling will follow immediately after a sudden pressure drop.

Phase segregation may occur at some point as the two-phase fluid flows through the geothermal reservoir towards the production zone of the well as the result of the increased relative permeability of the vapor phase. The steam and water flows can be defined in terms of a modified expression of Darcy's Law for each phase:

$$Q_i = k_{ri} \cdot \frac{k_a}{\mu_i} \cdot A \left(\frac{\Delta p}{L} \right) \qquad [1]$$

where Q_i, μ_i and k_{ri} are the mass flow, dynamic viscosity and relative permeability of phase i, k_a is the intrinsic permeability, A the cross-sectional area and $\frac{\Delta p}{L}$ the pressure gradient. The lower viscosity of the vapor phase allows it to rise faster than a liquid phase in response to buoyant forces. Throughout most of the pressure range of interest in geothermal systems, the liquid phase dynamic viscosity is 5-10 times that of the vapor phase. In addition, the two phases are exposed to different pressure gradients. This difference is attributed to capillary forces that retain water in the rock matrix, the result of the hydrophilic nature of most mineral surfaces and the surface tension of liquid water. The strength of these effects varies based on temperature, the degree of liquid saturation, the geometry of the pore space and the connectivity of a pore network.

Relative permeabilities are commonly determined for porous media in experimental settings (e.g. Horne et al., 2000). Recently, more attention has been given to model steam-liquid relative permeabilities in a fracture (e.g. Chen et al., 2004). Relative permeabilities are usually described in terms of liquid saturation, the volume fraction of liquid, rather than the mass fraction. Liquid saturation is related to vapor mass fraction by consideration of the density of each phase at a given vapor saturation pressure, as described in equation 2:

$$S^l = 1 - \frac{X^v \cdot \frac{1}{\rho^v}}{X^v \cdot \frac{1}{\rho^v} + (1 - X^v) \cdot \frac{1}{\rho^l}} \qquad [2]$$

where S^l represents liquid saturation, X^v vapor mass fraction, and ρ^v and ρ^l the densities of the vapor and liquid phases, respectively, determined at a given vapor saturation pressure. Due to the low density of vapor compared to liquid water, even a small vapor mass fraction significantly reduces the liquid saturation. Two models are typically used to model steam-water relative permeabilities, as exemplified by the Corey-type curves and the X-type curves displayed in Figure 3.3. The X-curve model assumes that there is no
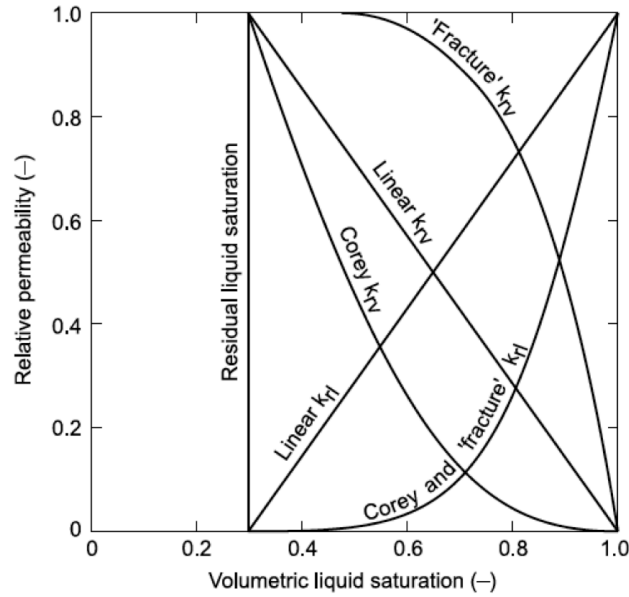
Figure 3.3. Typical relative permeability curves.
Adopted from Ingebritsen et al. (2010).

interference between phases, and that relative permeability is a simple function of liquid saturation ($k_{r,i} = S^l$). The Brooks-Corey model assumes substantial phase interference at $S^l > 0.8$, such that $k_{r,l} + k_{r,v} < 1$. The residual 'saturation' is the minimum volumetric saturation level below which a given phase is immobile; for the example curves in Figure 3.3, the residual liquid saturation is 0.3 and the residual vapor saturation is close to 0 (or $S^l = 1$).

The Corey model generally matches experimentally determined relative permeabilities in porous media. Conceptually, this is due to the effect of capillary pressures in a network of pore channels with a range of different aperture sizes; upon an initial reduction in liquid saturation, the liquid phase relative permeability decreases strongly as liquid-containing pore channels with larger apertures are rapidly desaturated (Pruess, 2002). As depressurization boiling proceeds, an increasing fraction of the remaining water is retained in pore channels with increasingly smaller radii. The isolated small vapor bubbles formed during early depressurization boiling are thought to be immobile as the result of surface tension effects and the geometry of the pore channels and flow space. The relative permeability of the steam phase starts to increase rapidly as the vapor saturation becomes high enough for it to form a continuous flowing phase; above a vapor saturation around ~0.75, the relative permeability of the steam phase is thought to be constant (~1). Due to the lack of understanding about the geometry of fractured reservoir rock and difficulty to reproduce such environments, vapor-liquid relative permeabilities in fractures are less well constrained by experimental data. However, the fracture can be expected to contribute much more to the total permeability of a geothermal reservoir than the rock matrix. In general, experimental simulations suggest that the relative permeability of vapor is considerably higher in fractured media compared with porous media (Chen et al., 2004).

3.2.2 Mathematical Description of Phase Segregation Model

Various researchers have modeled aquifer fluid compositions in high-temperature geothermal reservoirs from wellhead data applying the phase segregation model (e.g. Arnórsson et al., 1990; Arnórsson and Stefánsson, 2005; Arnórsson et al., 2007; Arnórsson

et al., 2010; Angcoy, 2010; Karingithi et al., 2010; Remoroza, 2010). In what follows, the symbology of Arnórsson et al. (2007) is adopted. Under this system, the first superscript indicates the location, or point, between the aquifer and discharge point considered in the model. Thus, f refers to the feed zone beyond the zone of depressurization (initial aquifer fluid) and d to the discharge at the wellhead. Additionally, in the open system phase segregation model considered, e represents the intermediate zone of evaporation (depressurization zone) wherein liquid is retained by the aquifer; the letters e and g refer to this fluid immediately before and following phase segregation. The second superscript denotes the fluid phase(s) considered – l representing liquid, v vapor, and t the total two-phase fluid mixture. The subscript refers to the species or components considered - s to gaseous components, r to non-volatile components and i to either.

Under isolated system conditions, conservation of fluid mass and enthalpy between the aquifer and the point of discharge can be expressed by equations 3 and 4:

$$M^{f,t} = M^{d,t} = M^{d,v} + M^{d,l} \qquad [3]$$

$$h^{f,t} = h^{d,t} = h^{d,v} \cdot X^{d,v} + h^{d,l}(1 - X^{d,v}) \qquad [4]$$

Conservation of mass for chemical components is described by:

$$m_i^{f,t} = m_i^{d,t} = m_i^{d,v} \cdot X^{d,v} + m_i^{d,l}(1 - X^{d,v}) \qquad [5]$$

However, under the assumption of phase segregation, a mass of the boiled liquid ($M^{e,lr}$) is retained in the formation, and the above conservation of mass and energy equations are modified by a term accounting for this "outflow" stream:

$$M^{d,t} = M^{f,t} - M^{e,lr} \qquad [6]$$

$$h^{d,t} \cdot M^{d,t} = h^{f,t} \cdot M^{f,t} - h^{e,l} \cdot M^{e,lr} \qquad [7]$$

Taking equation 6 relative to $M^{d,t}$:

$$1 = V^{f,t} - V^{e,lr} \qquad [8]$$

$V^{f,t}$ and $V^{e,lr}$ are defined as the relative mass of the total two-phase fluid inflowing into the production zone of a well and the mass of boiled and degassed liquid retained in the formation, respectively, in relation to the mass flow of the well discharge. Dividing equation 7 by $M^{d,t}$, substituting $V^{f,t} - 1$ for $V^{e,l,r}$ and isolating $V^{f,t}$, one can find an alternate expression for $V^{f,t}$:

$$V^{f,t} = \frac{h^{d,t} - h^{e,l}}{h^{f,t} - h^{e,l}} \qquad [9]$$

Under the assumption of a steam fraction of zero ($h^{f,t} = h^{f,l}$), $V^{f,t}$ can be obtained from steam tables once initial aquifer and phase segregation p/T conditions have been selected. To illustrate how $V^{f,t}$ changes under the assumptin of different phase segregation conditions and discharge enthalpy, the value of this parameter was calculated for selected discharge enthalpies ranging from 1400-2700 kJ kg^{-1} at phase segregation p/T conditions greater than 10 bars for a saturated liquid aquifer fluid at a temperature of 300°C (corresponding to a initial fluid pressure of ~86 bars-a). The results of these calculations are displayed in semi-log coordinates in Figure 3.4.

Figure 3.4 shows that for the example aquifer fluid described above, the ratio of inflowing initial aquifer fluid to the discharge mass flow is less than two under most assumptions (phase segregation pressures and discharge enthalpy). Calculated $V^{f,t}$ values
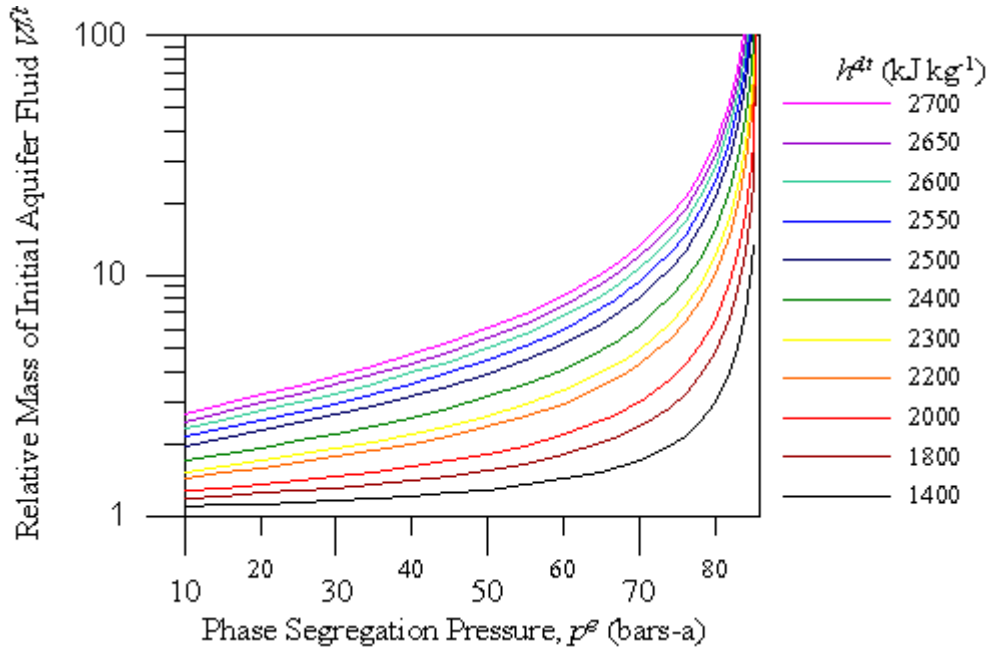
Figure 3.4. Calculated relative mass $V^{f,t}$ of initial, inflowing aquifer fluid relative to discharge mass flow as a function of phase segregation pressure p^e (bar-a) and discharge enthalpy $h^{d,t}$ (kJ kg^{-1}). The aquifer fluid was assumed to have liquid enthalpy at initial temperature $T^f =300°C$.

increase rapidly at higher discharge enthalpies ($h^{d,t} > 2400$ kJ kg^{-1}) and when phase segregation pressures close to the initial aquifer pressure (within ~5 bar) are assumed. It is worth considering why larger $V^{f,t}$ values are calculated assuming higher phase segregation pressures. At phase segregation pressures closer to the initial aquifer fluid, less vapor has been generated by boiling. In order to account for a given observed 'excess' discharge enthalpy, the increase in the vapor/liquid mass ratio upon phase segregation must be greater for assumed phase segregation pressures closer to the initial aquifer fluid pressure. Figure 3.4 broadly indicates that a considerable amount of liquid may be retained in the rock formation in the producing zone in a well of a boiling geothermal system by the process of phase segregation, especially for wells discharging high excess enthalpies.

Liquid saturation is the appropriate parameter for evaluating what phase segregation pressures are logical to select. For the aquifer fluid considered in Figure 3.4, depressurization boiling from 300°C/~86 bars will result in the residual liquid saturation displayed by the example relative permeability curves in Figure 3.3 (0.2) at ~50 bars. If phase segregation is believed to occur dominantly at the pressure where the liquid phase is completely immobile, 50 bars-a may be considered a reasonable phase segregation pressure to assume. For the present study, aquifer compositions were calculated at multiple assumed phase segregation pressures, but a pressure approximately in between the initial aquifer fluid and wellhead pressures was taken to be the most logical assumption in light of the above consideration. The relationship between the most logical assumed phase segregation pressure and the considered residual liquid saturation is not straightforward, since phase segregation likely occurs across a pressure interval rather than a single pressure. For the fractured volcanic rocks of the Hellisheidi reservoir, it is likely that this interval is well approximated by the 'mid-point' phase segregation pressure. In hyaloclastites and vesicular tops of basalt lavas, phase segregation may be expected to occur at higher liquid saturations than in tectonic and contraction fractures where fluid

flows must be concentrated. However, it seems unlikely for phase segregation to be found close to the initial aquifer fluid or wellhead pressure. As much of the variability in $V^{f,t}$ becomes more apparent at assumed phase segregation pressures closer to the initial aquifer fluid pressure, it is concluded that the uncertainty associated with $V^{f,t}$ is fairly low.

The principal objective of the present study is to assess the chemical composition of the feedzone fluid from wellhead data. Below a sensitivity analysis is given, describing how selection of p^e affects the the calculated concentrations of chemical components in an initial aquifer fluid. The calculations for volatile and non-volatile components differ somewhat. For a non-volatile component, the total mass of a non-volatile component at discharge is equal to the mass contained in the initial aquifer fluid minus the mass in the retained liquid at the point of phase segregation. This is expressed in terms of relative mass as:

$$m_r^{f,t} \cdot V^{f,t} - m_r^{e,l} \cdot V^{e,lr} = m_r^{d,t} \qquad [10]$$

Further, because it is assumed that no loss of non-volatile component r occurs between the aquifer and the point of phase segregation ($m_r^{f,t} = m_r^{e,t}$), $m_r^{e,l}$ can be written as:

$$m_r^{e,l} = m_r^{f,t} \left(\frac{1}{1-X^{e,v}} \right) \qquad [11]$$

where $X^{e,v}$ is the vapor mass fraction of flowing fluid after depressurization boiling to phase segregation pressure p^e, but before retention of liquid in the aquifer, given by:

$$X^{e,v} = \frac{h^{f,t}-h^{e,l}}{h^{e,v}-h^{e,l}} \qquad [12]$$

Once initial aquifer and phase segregation p/T conditions have been selected, the terms described above can be combined in a single relationship (after substituting $V^{f,t} - 1$ for $V^{e,lr}$) to calculate the concentration of a non-volatile in the initial aquifer fluid from measurements taken at the point of discharge:

$$m_r^{f,t} = m_r^{d,t} \cdot \left[V^{f,t} \left(1 - \frac{1}{1-X^{e,v}} \right) + \frac{1}{1-X^{e,v}} \right]^{-1} \qquad [13]$$

The sensitivity of model outcomes to assumed phase segregation pressure can be obtained from equation 13 above (Figure 3.5). It can be seen from this figure that the selected phase segregation pressure does not significantly affect the calculated concentration of a non-volatile in the initial aquifer fluid, especially across the middle of the pressure range where phase segregation is most likely to occur and for wells with discharge enthalpies below 2400-2500 kJ kg^{-1}.

The calculated concentrations of gaseous components are markedly more sensitive to the selected phase segregation pressure. This is because the assumed phase segregation pressure greatly impacts the composition and relative mass of the retained liquid. Assuming that the concentration of gaseous components in the retained liquid is neglible, the calculated aquifer concentration is simply inversely proportional to $V^{f,t}$, expressed by:

$$m_s^{f,t} = \frac{m_s^{d,t}}{V^{f,t}} \qquad [14]$$

However, assuming that the retained liquid represents an 'outflow' stream, equation 15 is modified to:

$$m_s^{d,t} = m_s^{f,t} \cdot V^{f,t} - m_s^{e,l} \cdot V^{e,lr} \qquad [15]$$
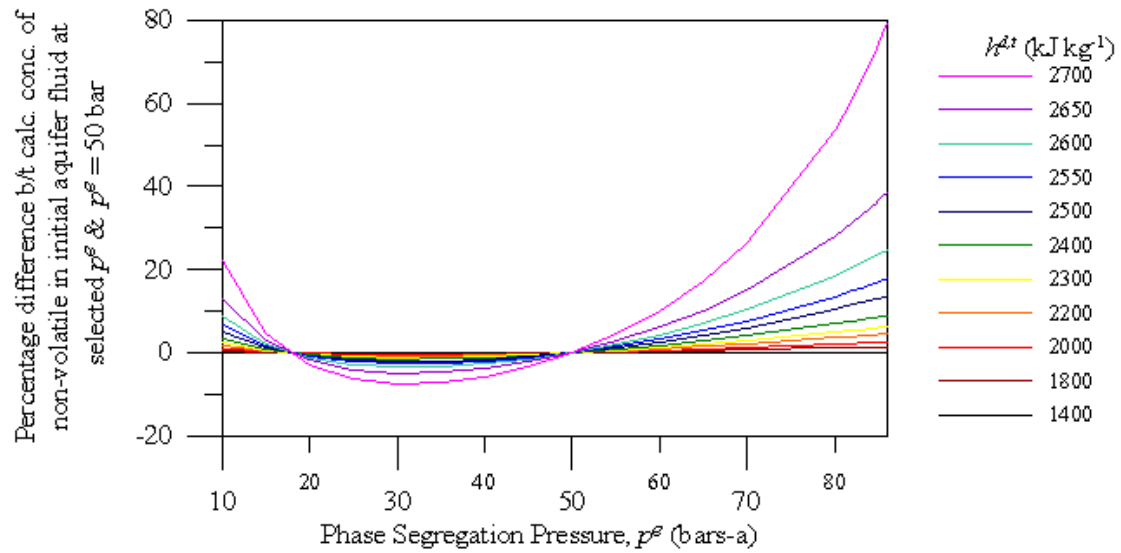
Figure 3.5. Percentage difference between calculated concentration of a non-volatile component in initial aquifer fluid at selected phase segregation pressure p^e (bars-a) and calculated concentration at $p^e = 50$ bars-a for different discharge enthalpies $h^{d,t}$. The aquifer fluid was assumed to have liquid enthalpy at an initial temperature $T^f = 300°C$.
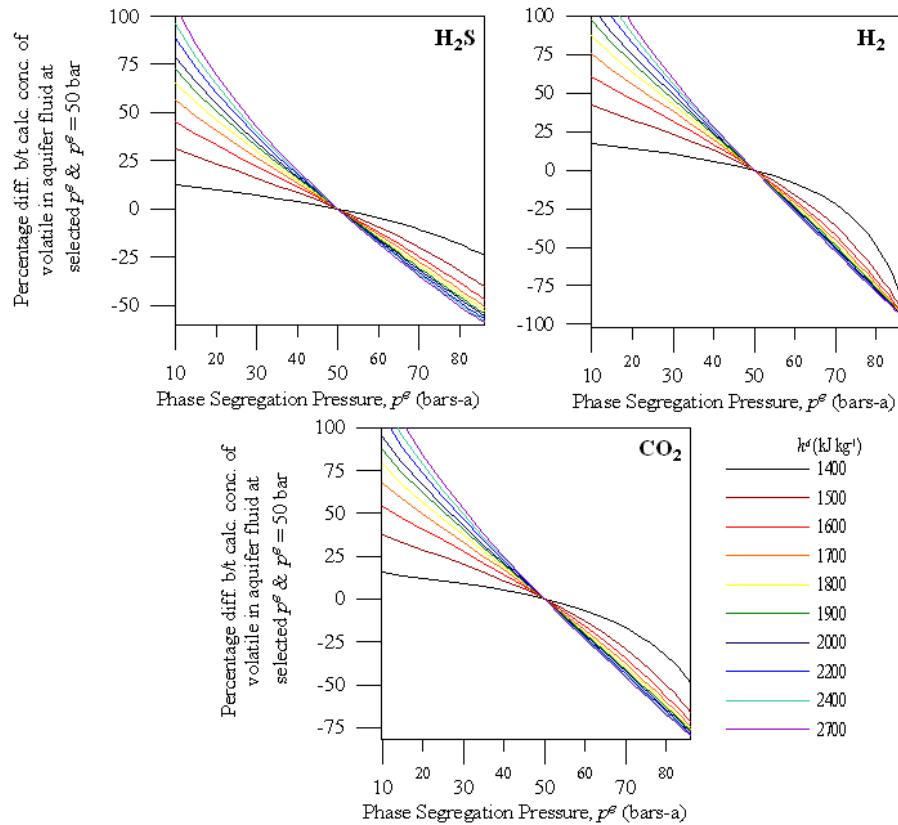

Figure 3.6. Percentage difference between calculated concentration of volatile components (H_2S, H_2 and CO_2) in initial aquifer fluid at selected phase segregation pressure p^e (bar-a) and calculated concentration at $p^e = 50$ bar-a for different discharge enthalpies. Same assumptions as Figures 3.4 and 3.5.

29

where $m_s^{e,l}$ is the concentration of a volatile species in the retained liquid. Assuming its total concentration in the two phase fluid at the point p^e, prior to phase segregation is equal to to its total concentration in the initial aquifer fluid ($m_s^{f,t} = m_s^{e,t}$), $m_s^{e,l}$ can be approximated by the formulation:

$$m_s^{e,l} = \frac{m_s^{f,t}}{[X^{e,v}(D_S^e - 1) + 1]} \qquad [16]$$

where D_S^e is the distribution coefficient of a gaseous species between vapor and liquid, calculated at the phase segregation pressure. The coefficient D_s is a function of gas solubility and fluid pressure, defined:

$$D_s = \frac{m_s^v}{m_s^l} \cong \frac{55.508}{p_{tot} \cdot K_{H,s}} \xi \qquad [17]$$

where $K_{H,s}$ is the Henry's Law coefficient (moles kg^{-1} bar^{-1}) for a certain gas species, p_{tot} (bars-a) the vapor pressure p_{H_2O} plus the sum of partial pressures of all gaseous components (since the partial pressures of non-condensable gas species contribute little relative to vapor pressure, $p_{tot} \approx p_{H_2O}$), ξ a degassing factor (assumed to be unity, representing equilibrium degassing) and 55.508 a factor for converting 1 kg of H_2O into moles of H_2O (see Arnórsson et al. (2007) for complete derivation). After combining equations 15 and 16 and substituting $V^{f,t} - 1$ for $V^{e,lr}$, one can obtain the following equation for the concentration of a volatile component in the initial aquifer fluid from discharge measurements and selection of phase segregation and initial aquifer p/T conditions:

$$m_s^{f,t} = m_s^{d,t} \cdot \left[V^{f,t}\left(1 - \frac{1}{[X^{e,v}(D_S^e - 1) + 1]}\right) + \frac{1}{[X^{e,v}(D_S^e - 1) + 1]} \right]^{-1} \qquad [18]$$

Using equation 18, a sensitivity analysis similar to Figures 3.5 was performed to examine the effect of assumed phase segregation pressure on calculated initial aquifer fluid gas concentration (Figure 3.6). It can be seen from this figure that the calculated concentration of a gaseous component is quite sensitive to the assumed phase segregation pressure. Equations 16 and 18 assume that the non-volatile components are found in the liquid phase as a single species, whose solubility is described by the Henry's law constant. However, CO_2 and H_2S can exist in deprotonated forms; thus, the magnitude of pH change between the initial aquifer fluid and the phase segregation pressure affects the distribution of these components. Under the WATCH calculation procedure, the concentration and speciation of gaseous components in the retained liquid is taken into consideration when calculating aquifer fluid compositions .

The WATCH program (Arnórsson et al., 1982), version 2.4, was used to calculate the aquifer fluid composition from data on surface well discharges and the phase segregation model outlined above. For liquid enthalpy wells, the program assumes that the total well discharge represent the initial aquifer fluid. For excess enthalpy wells, the calculations involve two main steps. In the first step component concentrations and speciation distribution is calculated at the point p^g, the selected phase segregation pressure immediately after phase segregation has occurred, using the measured discharge enthalpy value. The second step uses the computed composition and pH of the liquid and vapor phases at p^e and calculates the composition and speciation distribution at temperature T^f and enthalpy of the feedzone fluid. This enthalpy can either be selected as liquid enthalpy at T^f or as a higher enthalpy that accounts for the presence of equilibrium vapor in the
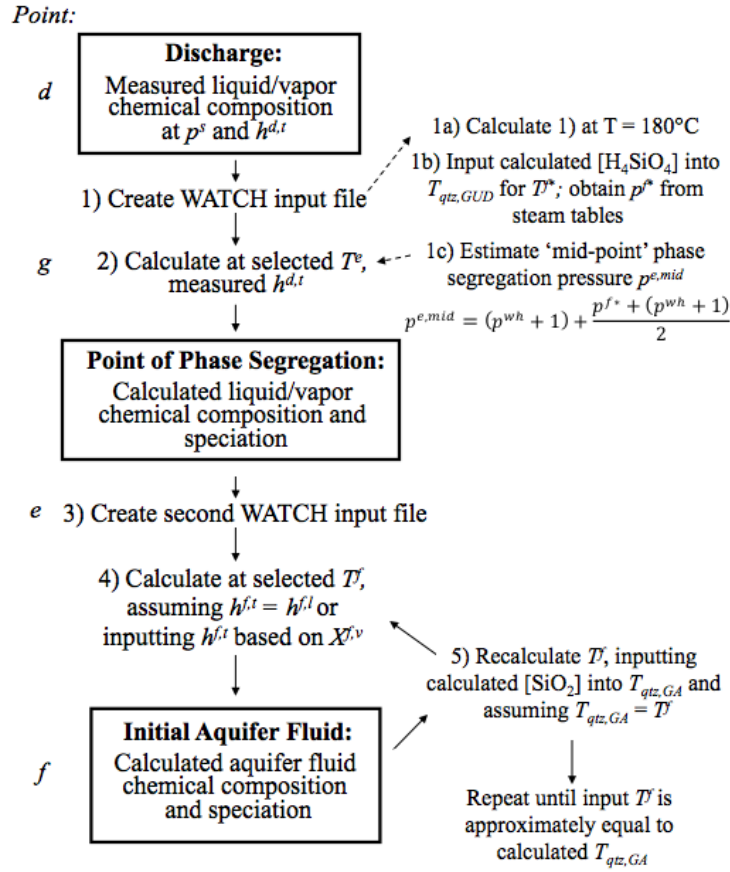
Figure 3.7. Procedure used to calculate aquifer fluid compositions for 'excess' enthalpy wells using WATCH under the phase segregetation model. The 'mid-point' phase segregation pressure can be assumed optionally.

initial feedzone fluid. The process just described for excess enthalpy wells is depicted for clarification in Figure 3.7.

The details of the calculations in WATCH have been summarized below. Assuming conservation of enthalpy and chemical components between discharge and the point of phase segregation, the concentration of a chemical component in the discharge can be expressed as:

$$m_i^{d,t} = m_i^{g,t} = m_i^{d,l}\left(1 - X^{d,v}\right) + m_i^{d,v} \cdot X^{d,v} = m_i^{e,l}(1 - X^{g,v}) + m_i^{e,v} \cdot X^{g,v} \qquad [19]$$

where point g represents the fluid immediately after phase segregation and $X^{g,v}$ the steam fraction at this point, given by:

$$X^{g,v} = \frac{h^{d,t} - h^{e,l}}{h^{e,v} - h^{e,l}} \qquad [20]$$

One should note the differences between point g and point e; the former represents a two-phase fluid at discharge enthalpy and total chemical composition, while the latter a two-phase fluid with initial aquifer fluid enthalpy and the same chemical composition as the aquifer fluid. The fluid mixture is transformed from point e to point g by retention of
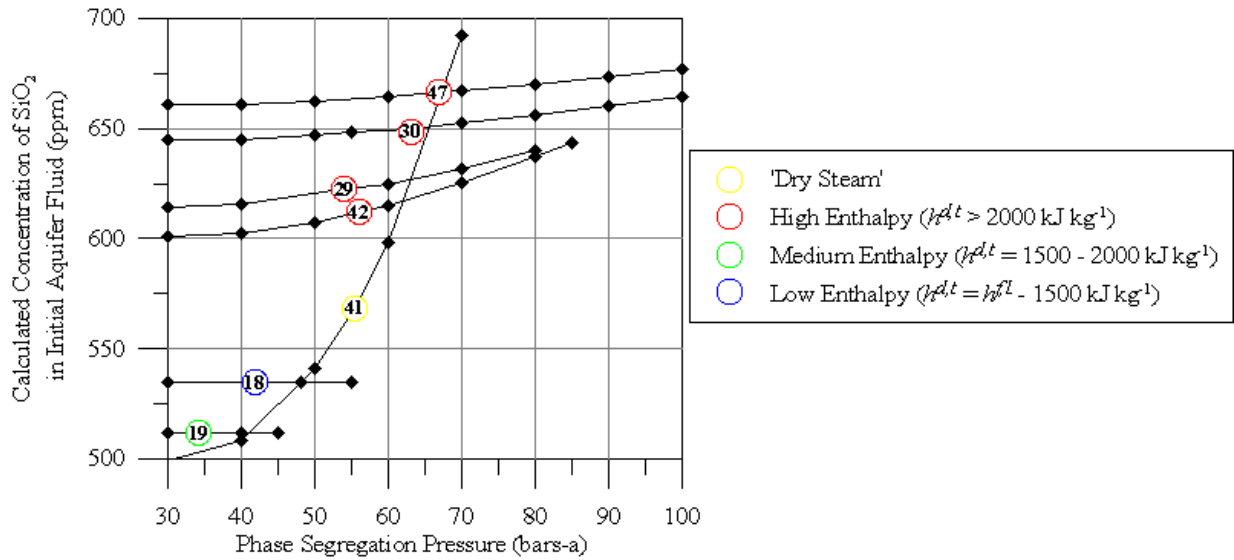
Figure 3.8. Calculated concentration of SiO₂ in initial aquifer fluid as a function of selected phase segregation pressure. Black markers designate selected phase segregation pressures assuming which initial aquifer fluid compositions were calculated.
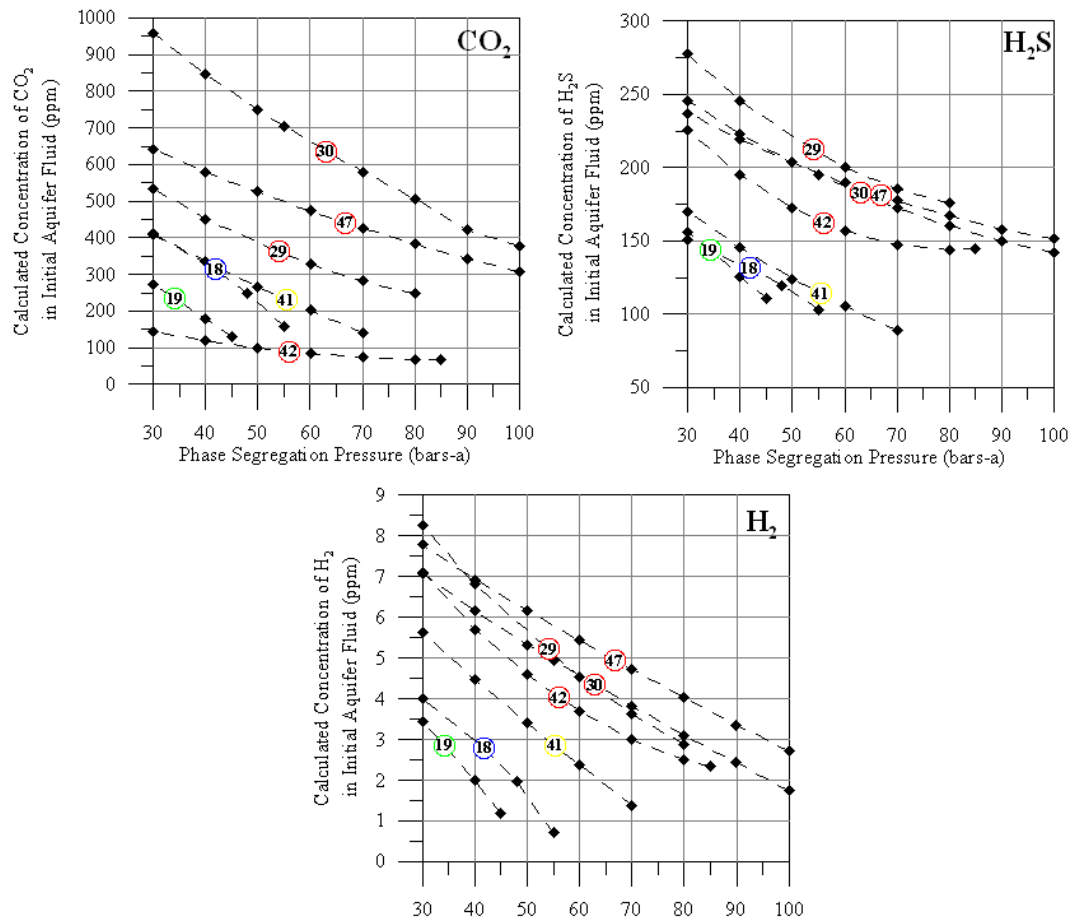
Figure 3.9. Calculated concentration of CO₂, H₂S and H₂ in initial aquifer fluid as a function of selected phase segregation pressure for selected wells. Symbology same as above.

liquid at a single p^e/T^e (to use consistent notation). Thus, $m_i^{e,l} = m_i^{g,l}$ and $m_i^{e,v} = m_i^{g,v}$, and all specific enthalpies are the same at both points.

The liquid/vapor compositions of the initial aquifer fluid, assuming conservation of enthalpy and chemical components between point e and the initial aquifer fluid is given by:

$$m_i^{f,t} = m_i^{e,t} = m_i^{e,l}(1 - X^{e,v}) + m_i^{e,v} \cdot X^{e,v} \qquad [21]$$

For comparison with Figures 3.5 and 3.6, the aquifer fluid concentrations of silica and the main reactive gases (CO_2, H_2S, H_2) at different assumed phase segregation pressures are shown for a few representative well discharges in Figures 3.8 and 3.9, respectively. Figure 3.7 shows that, unless the discharge enthalpy of the well approaches that of dry steam (ex. HE-41), the assumed phase segregation pressure makes a relatively insignificant difference to the calculated concentration of SiO_2 in the initial aquifer fluid, and thus the selected reference temperature using quartz geothermometry. For all wells except the dry-steam wells, the quartz geothermometer of Gunnarson and Arnórsson (2000) was used to determine T^f. After 5-10 iterations of the process outlined in Figure 3.7, there is less than 0.2°C discrepancy between input T^f and the resultant quartz geothermometer $T_{qtz,GA}$. The largest error in estimated initial aquifer fluid temperatures can be attributed to inaccurate thermodynamic data for quartz at >300°C. Since the quartz solubility curve flattens out above this temperature, relatively small differences in calculated SiO_2 concentrations correspond to relatively large differences in $T_{qtz,GA}$. The calculated SiO_2 concentrations in the 'dry-steam' wells are extremely sensitive to assumed phase segregation pressure; therefore, Na/K geothermometry was used to determine T^f, since the elemental ratio of non-volatile components is not affected by phase segregation or steam contamination. The Na/K geothermometer used in this study can be found in Arnórsson (2000), and is based on the feldspar solubility constants of Arnórsson and Stefánsson (1999). Due to systematic discrepancy between the Na/K temperature and the quartz temperature, with the latter corresponding better to feedzone temperatures (see Figure 4.1 and Table 4.1), 15°C was added to the Na/K temperature to determine the reference temperature for the dry-steam wells. The equations for the geothermometers used in this study are shown in Table 3.4.

From Figure 3.9 it is evident that the calculated concentration of a gaseous component in the initial aquifer fluid is quite sensitive to the assumed phase segregation pressure, even at relatively low excess discharge enthalpies. Thus, phase segregation pressures should be selected with care. The 'mid-point' phase segregation pressure described in Figure 3.7 is a fairly reasonable assumption in light of consideration of the liquid saturation after boiling from T^f to that pressure. Using equation 2, these values were calculated for all the wells considered in the present study (Figure 3.10). This liquid saturation at the 'mid-point' phase segregation pressu fairly consistent between all of the well discharges (~0.2-0.3), approximately the residual liquid saturation predicted by the

Table 3.4: Geothermometer equations used in this study. Valid at p_{sat} at 0-350°C.

Geothermometer	Equation (T°C)	Source
$T_{qtz,GA}$ (SiO_2)[a]	$-54.8 + 0.3729 \cdot X - (5.602 \cdot 10^{-4}) \cdot X^2 + (5.719 \cdot 10^{-7}) \cdot X^3 + 73.917 \cdot \log(X)$	(1)
$T_{qtz,GUD}$ ($H_4SiO_{4,aq}$)[b]	$-132.2 + 0.036206 \cdot Y + (55.865 \cdot 10^{-6}) \cdot Y^2 - (2.699 \cdot 10^{-8}) \cdot Y^3 + 128.277 \cdot \log(X)$	(2)
$T_{Na/K}$ (Na/K)[c]	$+733.6 - 770.551 \cdot Z + 378.189 \cdot Z^2 - 95.753 \cdot Z^3 + 9.544 \cdot Z^4$	(3)

(1) Gunnarsson and Arnórsson (2000) (2) Gudmundsson and Arnórsson (2002) (3) Arnórsson (2000)
[a] X is SiO_2 in ppm. [b] Y represents the concentration of $H_4SiO_{4,aq}$ in ppm in equilibrium with quartz after adiabatic boiling to 10 bars-a vapor pressure (180°C). [c] Z denotes the logarithm of the molar Na/K ratio.
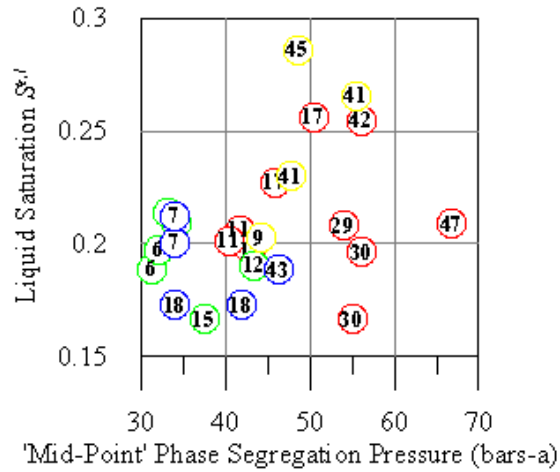
Figure 3.10. Calculated liquid saturation at the 'mid-point' phase segregation pressure for all excess enthalpy well discharges considered in this study. Symbology same as above.

example curves in Figure 3.3. However, a slight degree of phase segregation may be expected to occur before the residual liquid saturation has been reached during depressurization boiling, at pressures 10-20 bar below the initial aquifer fluid pressure. In that case, the 'mid-point' phase segregation pressure may overestimate initial aquifer fluid gas concentrations. Relative to the order of magnitude differences in the calculated concentrations between the different main gases, the uncertainty associated with the phase segregation model is relatively small. As will be seen in Section 4, modeled aquifer fluid compositions assuming the 'mid-point' phase segregation pressure generally correspond closely to equilibrium values with specific hydrothermal mineral assemblages.

3.2.3 Equilibrium Vapor Fraction

Throughout the previous discussion, the focus has been on modeling the chemical composition of feedzone fluids from wellhead data and to assess how sensitive the calculations are to the choice of phase segregation pressure. In reservoirs where temperatures follow the boiling point curve with depth, some vapor may be present in the initial aquifer fluid. The physical vapor fraction is defined as

$$X^{f,v} = \frac{h^{f,t} - h^{f,l}}{h^{f,v} - h^{f,l}} \qquad [22]$$

It is not possible to obtain a value for $X^{f,v}$ in equation 22 as $h^{f,t}$ is not known. However, by assuming reactive gas concentrations in the initial aquifer fluid to be fixed by equilibrium according to specific reactions, it is possible to obtain a value for $h^{f,t}$ to circumvent this problem. Vapor fractions obtained by chemical methods is termed equilibrium vapor fraction to distinguish it from the physical vapor fraction.

Published methods to calculate equilibrium vapor fractions vary based on the chemical reactions for which equilibria are assumed, either specific gas-gas (e.g. D'Amore and Celati, 1983, D'Amore and Truesdell, 1985) or mineral-gas (e.g. Arnórsson et al., 1990, Arnórsson et al., 2007) equilibria. The former methodology utilizes redox reactions, for which systematic disequilibrium has been observed in Icelandic geothermal fluids

34

(Stefánsson and Arnórsson, 2002). In addition, these methods assumed the total discharge chemical composition to be representative of the aquifer fluid, which is not true for well discharges that have undergone phase segregation.

The primary advantage of mineral-gas equilibria to estimate initial fractions is that chemical equilibrium between hydrothermal mineral assemblages and reactive gas concentrations in the aquifer liquid is generally assumed to be closely approached (e.g. Arnórsson and Gunnlaugsson, 1985). The gas species typically used for equilibrium vapor calculations are H_2 and H_2S, since CO_2 is often source rather than equilibrium controlled. Both H_2 and H_2S partition into the vapor phase, as determined by Henry's constants and the total vapor pressure. Thus, if initial aquifer fluid concentrations of these gases, particularly H_2, are calculated to be in excess of equilibrium, this can be attributed to the presence of a vapor phase. The vapor fraction calculated in this way can be derived from equation 23, which relates the total aquifer fluid concentration of a gas species with its concentration in the liquid phase:

$$m_s^{f,t} = m_s^{f,l}\big[X^{f,v}\big(D_s^f - 1\big) + 1\big] = m_s^{f,l}\left[\left(\frac{h^{f,t}-h^{f,l}}{h^{f,v}-h^{f,l}}\right)\big(D_s^f - 1\big) + 1\right] \qquad [23]$$

Due to the lower solubility of H_2 in liquid water compared to H_2S, H_2 is more sensitive to the presence of a vapor phase than H_2S, and is considered a more reliable indicator of the equilibrium vapor fraction.

In the original derivation of the equilibrium vapor calculation methodology (Arnórsson et al., 2007), the concentration of gases in the retained aquifer liquid water was neglected ($m_s^{d,t} \cdot M^{d,t} = m_s^{f,t} \cdot M^{f,t}$). However, this is not so when using WATCH to recalculate the composition and speciation of the retained liquid and the initial aquifer fluid after inputting a higher $h^{f,t}$ based on equilibrium vapor fraction calculations.

The basic equation used when taking gas concentrations in the retained liquid to be zero $M^{f,t} = V^{f,t} \cdot M^{d,t}$ is thus modified to become:

$$m_s^{d,t} \cdot M^{d,t} = m_s^{f,t} \cdot M^{f,t} - m_s^{e,l} \cdot M^{e,lr} \qquad [24]$$

This equation is expressed in term of relative mass in equation 25, below:

$$m_s^{d,t} = m_s^{f,t} \cdot V^{f,t} - m_s^{e,l} \cdot (V^{f,t} - 1) \qquad [25]$$

By solving for $m_s^{f,t}$, one obtains

$$m_s^{f,t} = \frac{(m_s^{d,t}-m_s^{e,l})}{V^{f,t}} + m_s^{e,l} = (m_s^{d,t} - m_s^{e,l})\left(\frac{h^{f,t}-h^{e,l}}{h^{d,t}-h^{e,l}}\right) + m_s^{e,l} \qquad [26]$$

If a phase segregation pressure is selected, allowing $m_s^{e,l}$ to be calculated by means of equation 16, all variables in equations 23 and 26 are known except for $h^{f,t}$. The $h^{f,t}$ value that provides the same $m_s^{f,t}$ in both equations can be determined by an iterative process. When $m_s^{f,t}$ has been obtained so has $h^{f,t}$, allowing $X^{f,v}$ to be obtained either using H_2 or H_2S. Alternatively, it is possible to obtain a value for p^e by finding a common solution for both gases (Arnórsson et al., 2010). This method is, however, not considered to be as reliable as is the selection of p^e.
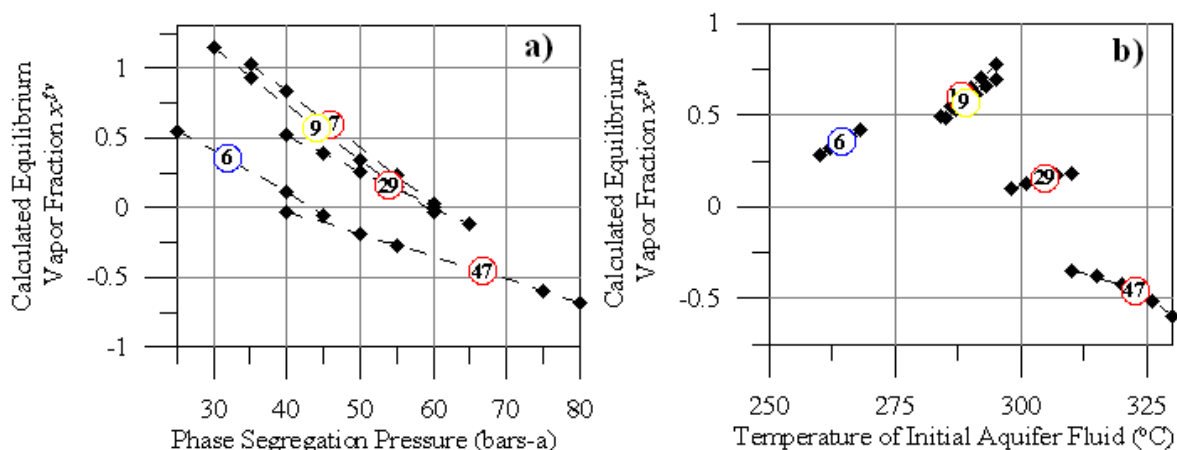
Figure 3.11. Calculated equilibrium vapor fractions for representative well discharges (HE-06, HE-09, HE-17, HE-29, HE-47) as a function of a) assumed phase segregation pressure a) and b) selected initial aquifer fluid temperature. Symbology same as above.

Based on the assumption of liquid phase hydrogen concentrations at equilibrium with a mineral assemblage consisting of pyrite, pyrrhotite, prehnite and epidote (see Table 3.6, below), a sensitivity analysis was conducted to evaluate the sensitivity of calculated equilibrium vapor fractions for a few representative wells to selected phase segregation pressure and reference temperature (Figure 3.11). For Figure 3.11 a), a constant initial aquifer fluid temperature was assumed (determined assuming the 'mid-point' phase segregation pressure) and the phase segregation pressure was varied; for Figure 3.11 b), the 'mid-point' phase segregation pressure was assumed and initial aquifer fluid temperature was varied. It is clear from this figure that calculated equilibrium vapor fractions are dependent on both the assumed phase segregation pressure and initial aquifer fluid temperature, but to a much lower extent for the latter than the former. If phase segregation occurs at pressures 10-15 bars above the 'mid-point' phase segregation pressure, the calculated equilibrium vapor fraction assuming mid-point phase segregation may overestimate the actual value by as much as a factor of 2. In comparison, an overestimation in the initial aquifer fluid temperature by $5^{\circ}C$ would result in a relatively small overestimation of equilibrium vapor fraction ($\sim 0.05 \ X^{f,v}$ units). Thus, there is substantial uncertainty in calculated equilibrium vapor fractions, even when using H_2 which is far more sensitive an indicator than H_2S. Calculated equilibrium vapor fractions for 'excess' enthalpy well discharges should be interpreted as order-of-magnitude, rather than absolute, indicators.

3.3 Thermodynamic Database and Solid Solution Mineral Composition

The thermodynamic database selected for this study plays an important role for both the speciation calculations performed by WATCH and to interpret the saturation state of the aquifer with respect to different mineral-fluid reactions that could potentially control the composition of aquifer fluids. The thermodynamic data base used for speciation calculations is that described in Arnórsson et al. (1982) with slight modifications. Gas solubility data was obtained from Fernandez-Prini et al. (2003). Al-hydroxide and ferrous and ferric hydroxide dissociation constants were taken from Arnórsson and Andrésdóttir (1999) and Arnórsson et al. (2002), respectively. The dissociation constant for $CaHCO_3^+$ is

based on the experimental data (0-90°C) of Plummer and Busenberg (1982) and extrapolated to higher temperatures using the electrostatic approach of Helgeson (1967). Finally, the Al-Si dimer of Pokrovskii et al. (1998) was included.

The saturation state of the aquifer liquid was assessed for hydrothermal alteration minerals, and several potential mineral pair and mineral assemblages were evaluated for their potential to control selected activity ratios and gas species concentrations in the initial aquifer fluid. The reactions considered and equations describing the temperature dependence of their equilibrium constants are shown in Tables 3.5 and 3.6, for the individual alteration minerals and the mineral pairs/assemblages, respectively. For all reactions, the equations shown in these tables assume unit activity for minerals and water and are valid from 0-350°C and at 1 bar below 100°C and at saturation pressure at higher temperaturesThe following thermodynamic data were used to obtain the equation in Tables 3.5 and 3.6; data on all minerals are from Holland and Powell (1998), except for pyrite and pyrrhotite which are from Robie and Hemingway (1995). Data for $H_2O_{(l)}$, Ca^{+2}, Fe^{+2} and OH^- are from SUPCRT92 (Johnson et al., 1992) using the slop98.dat dataset. The properties of $Fe(OH)_4^-$ and $Al(OH)_4^-$ were derived from Diakonov et al. (1999) and Pokrovskii and Helgeson (1995), respectively. The properties for $CO_{2,aq}$, H_2S_{aq} and $H_{2,aq}$ were retrieved from the gas solubility constants in pure water as given by Fernandez-Prini et al. (2003) and the thermodynamic properties as given in Robie and Hemingway (1995) assuming ideal behavior.

The equilibrium curves presented in Tables 3.5 and 3.6 assume that the activity of all mineral phases is unity. When a solid-solution mineral is present the activity of its end-member must be retrieved from its composition. In this study, new data based on analyses of six epidotes and seven prehnites obtained from well-cuttings from recently drilled wells HE-50 and HE-51 were used to obtain the mineral compositions. The compositions were using Energy Dispersive X-Ray Spectroscopy on a Scanning Electric Microscope (SEM-EDS). Primary data, given in weight percent oxide, was provided by Bragason (pers. comm.), and the calculated chemical formula and end-member activity for each individual mineral analyses as well as the average are provided in Table 3.7. End-member mineral activities were calculated assuming ideal solid-solution. As Table 3.7 shows, the average activities of epidote and prehnite were calculated to be 0.74 and 0.84, respectively, resulting in a clinozoisite activity of 0.26. This is similar to the average compositions of epidotes and prehnites in other geothermal systems in basaltic rocks in Iceland (Arnórsson et al., 2010). The fact that the activities of epidote and prehnite are so similar means that solid-solution mineral compositions will not significantly affect the equilibrium curve based on unit activities of all minerals.

Table 3.5: Alteration minerals, symbols, individual dissolution reactions and equations describing the temperature dependence of the equilibrium constant for the given reaction. Equations are valid in the range of 0-350°C at saturation pressure. Unit activity was selected for all minerals and liquid water.

Mineral	Symbol	Dissolution Reaction	LogK(T°K)	Source[a]
Calcite	cal	$CaCO_3 + 2H^+ \leftrightarrows Ca^{+2} + H_2O_{(l)} + CO_{2,aq}$	$-68.271 + 4385.24/T - 0.007525 \cdot T + 25.856 \cdot \log(T)$	(1)
Wollastonite	wol	$CaSiO_3 + H_2O_{(l)} + 2H^+ \leftrightarrows Ca^{+2} + H_4SiO_4^o$	$-127.096 + 8151.38/T - 0.02981 \cdot T + 49.282 \cdot \log(T)$	(1)
Clinozoisite	czo	$Ca_2Al_3Si_3O_{12}(OH) + 12H_2O_{(l)} \leftrightarrows 2Ca^{+2} + 3Al(OH)_4^- + 3H_4SiO_4^o + OH^-$	$+36.052 - 6854.78/T + 0.13236 \cdot T - (1.3749 \cdot 10^{-4}) \cdot T^2 - 33.508 \cdot \log(T)$	(1)
Epidote	epi	$Ca_2Al_2FeSi_3O_{12}(OH) + 12H_2O_{(l)} \leftrightarrows 2Ca^{+2} + Fe(OH)_4^- + 2Al(OH)_4^- + 3H_4SiO_4^o + OH^-$	$+893.547 - 27077.4/T + 0.54124 \cdot T - (3.022 \cdot 10^{-4}) \cdot T^2 - 398.38 \cdot \log(T)$	(1)
Prehnite	pre	$Ca_2Al_2Si_3O_{10}(OH)_2 + 10H_2O_{(l)} \leftrightarrows 2Ca^{+2} + 2Al(OH)_4^- + 3H_4SiO_4^o + OH^-$	$+833.95 - 25642.8/T + 0.5035 \cdot T - (2.941 \cdot 10^{-4}) \cdot T^2 - 369.297 \cdot \log(T)$	(1)
Microcline	mic	$KAlSi_3O_8 + 8H_2O_{(l)} \leftrightarrows K^+ + Al(OH)_4^- + 3H_4SiO_4^o$	$-78.594 + 311970/T^2 - 6068.51/T - (27.776 \cdot 10^{-6}) \cdot T^2 + 30.308 \cdot \log(T)$	(2)
Sanidine	san		$-77.837 + 316431/T^2 - 5719.10/T - (27.712 \cdot 10^{-6}) \cdot T^2 + 29.738 \cdot \log(T)$	(2)
High-Albite	h-alb	$NaAlSi_3O_8 + 8H_2O_{(l)} \leftrightarrows Na^+ + Al(OH)_4^- + 3H_4SiO_4^o$	$-97.275 + 306065/T^2 - 3313.51/T - (28.622 \cdot 10^{-6}) \cdot T^2 + 35.851 \cdot \log(T)$	(2)
Low-Albite	l-alb		$-96.267 + 305542/T^2 - 3985.5/T - (28.588 \cdot 10^{-6}) \cdot T^2 + 35.790 \cdot \log(T)$	(2)
Pyrite	pyr	$FeS_2 + 2H^+ + H_{2,aq} \leftrightarrows Fe^{+2} + 2H_2S_{(l)}^o$	$+949.951 - 24258.2/T + 0.51474 \cdot T - (2.402 \cdot 10^{-4}) \cdot T^2 - 417.136 \cdot \log(T)$	(1)
Pyrrhotite	pyrr	$FeS + 2H^+ \leftrightarrows Fe^{+2} + H_2S_{(l)}^o$	$-3.043 + 1579.06/T + 0.001987 \cdot T + 0.12 \cdot \log(T)$	(1)
Magnetite	mag	$Fe_3O_4 + 4H_2O_{(l)} \leftrightarrows Fe^{+2} + 2Fe(OH)_4^-$	$+949.951 - 24258.2/T + 0.51474 \cdot T - (2.402 \cdot 10^{-4}) \cdot T^2 - 417.136 \cdot \log(T)$	(1)

[a] The source given is for the equation describing the temperature dependence of the equilibrium constant only. Thermodynamic data for minerals and aqueous species used to derive these equations is given in the text. (1) Karingithi et al. (2010) (2) Arnórsson and Stefánsson (1999)

Table 3.6: Mineral pair and mineral assemblage reactions that may control activity ratios or gas concentrations in solution, and equations describing temperature dependence of equilibrium constant. Equations are valid in the range of 0-350°C at saturation pressure. Unit activity was selected for all minerals and liquid water. Sources are same as in Table 3.5.

Species	Reaction	LogK (T°K)	Source
$Ca^{+2}/(H^+)^2$	$\frac{3}{2}pre + 2H^+ \leftrightarrows Ca^{+2} + \frac{4}{5}H_2O_{(l)} + \frac{2}{5}czo + \frac{3}{5}qtz$	$+2.643 + 335{,}608/T^2 + 1550.1/T + (6.563 \cdot 10^{-4}) \cdot T - (6.123 \cdot 10^{-6}) \cdot T^2 + 0.870 \cdot \log(T)$	(1)
$Ca^{+2}/(H^+)^2$	$wol + 2H^+ \leftrightarrows Ca^{+2} + qtz + H_2O_{(l)}$	$+3.047 + 302{,}461/T^2 + 3088.8/T - 0.004542 \cdot T - (2.571 \cdot 10^{-6}) \cdot T^2 + 0.748 \cdot \log(T)$	(1)
$H_2S_{aq}/(H_{2,aq})^{1/3}$	$\frac{1}{2}pyr + \frac{2}{3}H_2O_{(l)} + \frac{1}{3}H_{2,aq} \leftrightarrows H_2S_{aq} + \frac{1}{6}mag$	$+12.225 + 500{,}528/T^2 - 7{,}771.49/T - 0.038468 \cdot T + (2.424 \cdot 10^{-5}) \cdot T^2 + 4.546 \cdot \log(T)$	(1)
$H_2S_{aq}/H_{2,aq}$	$pyr + H_{2,aq} \leftrightarrows H_2S_{aq} + pyrr$	$+0.549 - 124{,}186/T^2 - 972.20/T + 0.0036744 \cdot T - (3.227 \cdot 10^{-6}) \cdot T^2 + 0.383 \cdot \log(T)$	(1)
$CO_{2,aq}$	$czo + cal + \frac{3}{2}qtz + H_2O_{(l)} \leftrightarrows CO_{2,aq} + \frac{3}{2}pre$	$+0.890 + 7{,}251.5/T^2 - 1{,}710.6/T + 0.004188 \cdot T - (2.683 \cdot 10^{-6}) \cdot T^2 + 0.064 \cdot \log(T)$	(1)
H_2S_{aq}	$\frac{1}{3}pyr + \frac{1}{3}pyrr + \frac{2}{3}pre + \frac{2}{3}H_2O_{(l)} \leftrightarrows H_2S_{aq} + \frac{2}{3}epi$	$+13.608 + 592{,}324/T^2 - 9{,}346.7/T + 0.043552 \cdot T - (2.9164 \cdot 10^{-5}) \cdot T^2 + 5.139 \cdot \log(T)$	(1)
H_2S_{aq}	$\frac{1}{4}pyr + \frac{1}{2}pyrr + H_2O_{(l)} \leftrightarrows H_2S_{aq} + \frac{1}{4}mag$	$+13.589 + 590{,}215/T^2 - 9{,}024.5/T + 0.044882 \cdot T - (2.978 \cdot 10^{-5}) \cdot T^2 + 5.068 \cdot \log(T)$	(1)
$H_{2,aq}$	$\frac{4}{3}pyrr + \frac{2}{3}pre + \frac{2}{3}H_2O_{(l)} \leftrightarrows H_{2,aq} + \frac{2}{3}epi + \frac{2}{3}pyr$	$-1.640 - 124{,}524/T^2 - 777.19/T - 0.0005501 \cdot T + (7.756 \cdot 10^{-6}) \cdot T^2 - 0.565 \cdot \log(T)$	(1)
$H_{2,aq}$	$\frac{2}{3}pyr + \frac{1}{2}pyrr + H_2O_{(l)} \leftrightarrows H_{2,aq} + \frac{1}{4}mag + \frac{3}{4}pyrr$	$-1.654 - 95{,}456.8/T^2 - 621.84/T - 0.001257 \cdot T + (7.569 \cdot 10^{-6}) \cdot T^2 - 0.600 \cdot \log(T)$	(1)

Table 3.7. Results of analyses of solid solution mineral chemical compositions, given in weight percent of main oxide components, calculated chemical formula and activity.

		Weight Percent Oxide					
EPIDOTE Well	SiO_2	Al_2O_3	CaO	Fe_2O_3	SUM	Chemical Formula	a_{epi}
HE-50	37.02	22.67	22.55	13.98	96.22	$Ca_{1.96}Al_{2.17}Fe_{0.85}Si_{3.00}O_{12}(OH)$	0.82
HE-50	36.82	24.54	23.55	11.35	96.26	$Ca_{2.03}Al_{2.33}Fe_{0.68}Si_{2.97}O_{12}(OH)$	0.70
HE-51	37.05	23.64	23.52	12.54	96.75	$Ca_{2.02}Al_{2.24}Fe_{0.76}Si_{2.98}O_{12}(OH)$	0.77
HE-50	37.08	24.52	23.80	11.74	97.14	$Ca_{2.03}Al_{2.31}Fe_{0.71}Si_{2.97}O_{12}(OH)$	0.71
HE-50	37.36	23.06	23.82	13.81	98.05	$Ca_{2.03}Al_{2.17}Fe_{0.83}Si_{2.98}O_{12}(OH)$	0.85
HE-50	38.97	26.41	24.82	9.81	100.01	$Ca_{2.04}Al_{2.40}Fe_{0.57}Si_{3.00}O_{12}(OH)$	0.60
					AVERAGE:	**$Ca_{2.02}Al_{2.27}Fe_{0.73}Si_{2.99}O_{12}(OH)$**	**0.74**
PREHNITE							a_{pre}
HE-50	42.96	22.64	27.30	1.94	94.84	$Ca_{2.04}Al_{1.87}Si_{3.00}O_{10}(OH)_2$	0.91
HE-50	43.11	20.37	26.88	5.94	96.30	$Ca_{2.00}Al_{1.67}Si_{3.00}O_{10}(OH)_2$	0.71
HE-50	43.57	23.40	27.42	2.39	96.78	$Ca_{2.01}Al_{1.89}Si_{2.99}O_{10}(OH)_2$	0.89
HE-50	42.82	23.44	27.14	1.30	94.70	$Ca_{2.03}Al_{1.93}Si_{2.99}O_{10}(OH)_2$	0.95
HE-50	42.24	19.80	26.92	6.17	95.13	$Ca_{2.04}Al_{1.65}Si_{2.99}O_{10}(OH)_2$	0.70
HE-51	43.13	22.68	26.91	1.11	93.83	$Ca_{2.02}Al_{1.88}Si_{3.03}O_{10}(OH)_2$	0.94
HE-51	42.47	20.91	26.77	4.25	94.40	$Ca_{2.03}Al_{1.74}Si_{3.00}O_{10}(OH)_2$	0.78
					AVERAGE:	**$Ca_{2.02}Al_{1.80}Si_{3.00}O_{10}(OH)_2$**	**0.84**

4 Results and Discussions

Any quantitative interpretations of the chemical compositions of high temperature aquifer fluids should be made in the context of the inherent uncertainty of the model calculations. Under the phase segregation model, the key assumption used to account for 'excess' discharge enthalpy was the retention of liquid at a single pressure between aquifer and wellhead conditions. Segregation is likely to occur over a range of pressure rather than at a single pressure and where it occurs depends on the properties of the rocks, namely the surface area between flowing fluid and mineral surface area in relation to relative permeability. Around pressures half way between that of the initial aquifer fluid and the wellhead, the volume fraction of liquid in the two-phase fluid approximates the minimum liquid saturation where phase segregation is most likely occur. It is unlikely that phase segregation will occur close to inflow into wells or undisturbed aquifer fluid, respectively, because liquid volume fractions of the flowing fluid will be too high and low, respectively, for phase segregation to occur to any extent. For that reason, the aquifer compositions shown in Table 4.1, calculated at the approximate 'mid-point' phase segregation pressure with the assumption of no equilibrium vapor, are considered to be reasonable.

The idea of local chemical equilibria within the context of a larger, open geothermal system has provided direction to many studies in the field of hydrothermal geochemistry (e.g. Helgeson, 1970; Arnórsson et al., 1983a; Gudmundsson and Arnórsson, 2005; Heinrich, 2005). To that end, much attention has been given to the minerals or mineral assemblages that could potentially control aquifer fluid chemistry. The state of chemical equilibria with respect to individual hydrothermal minerals will be described in Section 4.1. This will be followed by a discussion of the mineral assemblages that could potentially control reactive gas concentrations in Sections 4.2. Section 4.3 focuses on the distribution of chemical components, particularly reactive gases, on the scale of the geothermal field and will attempt to link observed trends or patterns to physical processes, such as upflow, outflow and recharge.

It is worth keeping in mind that the interpretations of the assessed state of chemical equilibria are dependent on the thermodynamic database used to derive equilibrium constants for different reactions, as well as for modeling the distribution of chemical components between different aqueous species. A further assumption is that samples taken at the wellhead are representative of fluids from individual deep aquifers that can be evaluated at a single assumed reference temperature and do not precipitate minerals or dissolve rocks or casing materials with which they could interact during production. However, there is reason to believe that the uncertainty associated with these assumptions does not prevent any useful quantitative interpretations to come from these calculations.

Table 4.1: Calculated initial aquifer fluid chemical compositions assuming 'mid-point' phase segregation pressure. Physical parameters associated with 'mid-point' phase segregation pressure are also provided. All concentrations given in ppm (mg kg^{-1}).

Sample #	Well	$h^{d,t}$ (kJ kg^{-1})	$p^{e,mid}$ (bars-a)	$X^{e,v}$ (wt. %)	$V^{f,t}$	T^f (°C)	pH	SiO$_2$	B	Na	K	Ca	Mg	Al	Fe	TCC^a	TSS^b	SO$_4$	Cl	F	H$_2$	CH$_4$	N$_2$
10-5079	HE-47	2139	66.8	15.0	3.88	322.7	7.34	666.2	1.19	97.9	24.0	0.18	0.001	1.04	0.005	441.0	181.0	4.2	133.6	0.706	4.94	0.33	3.74
10-5080	HE-19	1599	34.2	6.9	4.55	266.1	7.07	511.7	0.97	159.0	25.3	0.47	0.001	1.24	0.012	234.2	143.5	6.6	151.0	0.858	2.85	0.19	1.43
10-5081	HE-30	2173	55.0	15.5	3.98	315.2	7.11	648.5	0.97	109.3	24.0	0.23	0.001	1.06	0.006	704.9	195.4	6.5	134.8	0.705	4.96	0.49	3.67
10-5082	HE-15	1597	37.5	7.8	3.89	273.8	6.99	535.6	0.88	142.4	23.5	0.39	0.002	1.22	0.007	430.8	143.3	7.5	130.8	0.838	1.96	0.35	5.85
10-5083	HE-17	2054	45.8	9.1	6.10	288.0	7.05	577.7	1.09	139.1	27.0	0.24	0.003	1.26	0.011	346.7	200.9	8.9	151.2	0.804	5.89	0.35	2.69
10-5084	HE-11	2047	40.4	9.2	6.09	282.0	7.16	560.1	0.80	129.9	24.8	0.16	0.001	1.51	0.005	515.7	133.1	9.0	121.3	0.730	3.7	0.39	2.95
10-5085	HE-06	1548	32.0	5.1	5.48	264.3	6.91	505.7	0.54	130.1	20.7	0.39	0.005	1.55	0.057	821.2	128.3	7.4	81.6	0.822	3.37	0.29	2.96
10-5086	HE-46	1177	-	-	-	269.7	7.01	523.1	0.30	138.7	24.1	0.41	0.002	1.53	0.012	947.7	70.70	33.3	49.1	0.908	0.14	1.51	45.2
10-5087	HE-52	1169	-	-	-	265.6	7.04	510.0	0.36	134.0	21.4	0.96	0.001	1.41	0.006	785.4	42.8	22.9	58.3	1.083	0.21	1.63	41.1
10-5163	HE-18	1385	41.8	6.1	2.77	273.5	7.20	534.6	0.69	134.2	23.3	0.24	0.001	1.50		313.3	131.3	15.5	113.2	0.772	2.79	0.71	7.58
10-5164	HE-09	2757	44.1	10.0	9.77	288.9	6.88	365.9	1.19	76.6	15.5	0.53	0.005	0.54	0.063	290.7	202.7	3.1	91.4	0.399	5.86	0.10	1.48
10-5165	HE-57	1043	-	-	-	279.1	7.13	551.8	0.79	145.1	27.0	0.73	0.000	1.17		781.2	141.9	14.2	115.0	0.371	0.62	1.97	65.41
10-5166	HE-03	1216	-	-	-	272.7	7.21	531.9	0.87	204.3	38.2	0.58	0.000	0.95		130.8	100.1	8.9	289.8	0.696	0.11	0.10	10.96
10-5168	HE-12	1746	43.4	10.5	3.57	289.8	7.20	582.4	0.99	143.6	27.3	0.24		1.41	0.005	374.2	198.3	13.4	143.6	0.706	4.97	0.49	3.47
10-5169	HE-07	1372	33.9	7.2	2.61	266.6	7.09	513.2	0.93	159.6	26.8	0.29		1.35		209.7	157.7	6.7	149.5	0.911	2.94	0.34	24.06
10-5170	HE-45	2498	48.5	9.4	8.80	285.4	7.06	634.2	1.81	100.5	21.8	0.17	0.001	1.27	0.016	160.2	110.3	2.3	122.3	0.979	2.11	0.04	1.2
10-5171	HE-42	2489	56.0	9.9	8.24	300.6	7.15	611.9	1.75	97.0	21.0	0.16	0.001	1.22	0.016	90.1	162.2	2.2	118.0	0.945	4.03	0.11	2.01
10-5172	HE-41	2704	55.4	9.3	10.23	298.3	7.12	568.5	1.63	90.1	19.5	0.15	0.001	1.14	0.015	230.9	113.9	2.0	109.6	0.878	2.85	0.06	1.42
09-5190	HE-05	1194	-	-	-	274.0	7.23	536.4	0.32	127.4	23.1	0.32	0.001	1.52		811.2	87.10	12.9	61.2	1.365	0.13	1.40	27.89
09-5198	HE-06	1548	31.2	7.6	3.91	263.8	6.84	504.1	0.56	131.4	20.9	0.41	0.001	1.54		781.1	130.3	9.3	85.8	0.576	2.1	0.23	2.54
09-5199	HE-17	2319	50.4	8.7	8.13	291.8	7.07	588.0	1.23	142.1	27.9	0.26	0.001	1.26		304.4	239.6	4.2	161.3	0.583	4.86	0.23	3.14
09-5197	HE-29	2399	54.0	15.3	5.02	304.8	7.28	622.6	3.96	92.9	19.4	0.41	0.010	1.65	0.030	362.4	212.0	2.0	73.9	1.132	5.22	0.71	27.34
09-5200	HE-41	2704	47.7	9.4	10.09	290.9	7.46	483.0	0.69	48.8	10.0	0.12	0.003	1.56	0.025	223.5	140.6	2.0	27.7	0.714	2.46	0.07	5.21
09-5189	HE-43	1466	46.2	11.4	1.77	295.4	6.90	598.1	1.05	97.3	19.2	0.72	0.001	1.56	0.007	898.3	264.2	7.2	61.5	0.751	5.72	0.88	124.8
08-3001	HE-07	1372	34.0	7.7	2.44	268.5	7.16	519.1	0.97	158.3	25.8	0.28	0.009	1.37	0.009	183.1	180.8	5.9	156.8	0.867	3.29	0.50	11.61
08-3002	HE-12	1746	45.0	11.3	3.29	294.0	7.13	594.1	0.99	136.9	25.9	0.20	0.004	1.38	0.022	370.2	244.4	10.0	142.7	0.917	7.24	0.80	4.98
08-3003	HE-17	2319	43.0	8.9	8.04	287.8	6.93	575.7	1.06	128.0	26.2	0.20	0.002	1.22	0.007	380.0	254.0	4.0	149.7	0.724	7.4	0.49	31.25
08-3004	HE-11	2047	41.6	9.2	6.08	283.5	7.04	563.8	0.78	125.6	23.8	0.13	0.001	1.52	0.018	514.2	158.8	6.4	118.1	0.807	4.52	0.60	19.77
08-3005	HE-29	2399	52.0	15.7	4.88	306.0	7.31	624.3	3.97	85.8	17.2	0.16	0.002	1.46	0.003	379.1	192.3	2.6	69.7	1.267	5.08	0.40	5.8
08-3006	HE-05	1194				275.5	7.23	540.7	0.31	121.6	21.6	0.25	0.000	1.56	0.003	827.7	76.60	14.9	59.7	1.611	0.28	2.39	56.06
08-3007	HE-06	1548	33.1	7.0	4.16	264.6	6.91	506.7	0.54	128.1	19.9	0.30	0.001	1.56	0.003	725.1	111.3	8.3	85.7	0.728	2.62	0.32	4.3
08-3008	HE-03	1396	32.4	9.3	2.22	271.8	7.33	529.6	0.80	194.5	36.3	0.57	0.001	0.96	0.013	64.4	30.80	9.0	279.8	0.664	0.21	0.16	4.46
08-3009	HE-18	1385	34.0	9.1	2.13	273.4	7.06	534.1	0.66	129.2	21.6	0.25	0.001	1.51	0.005	444.3	142.0	6.9	112.8	0.909	3.49	1.02	19.68

^{a} Total carbonate carbon, expressed as ppm CO$_2$

^{b} Total sulfide sulfur, expressed as ppm H$_2$S

4.1 Mineral-Solution Equilibria

As was discussed in Section 2.2, the process of water-rock interaction leads to the dissolution of primary rock forming minerals and the precipitation of more thermodynamically stable secondary alteration minerals. Geothermal systems, like all systems are open. Such large systems may be divided into small sub-systems within which temperature, pressure and composition vary insignificantly. Local chemical equilibrium for some reactions may be closely approached within such subsystems. The concept of local equilibrium is the basis for studying equilibrium within open natural systems. For most of the wells considered in this study, initial aquifer fluid temperatures were determined by assuming equilibrium with respect to quartz. For the 'dry-steam' wells, initial aquifer fluid temperatures were determined assuming equilibrium with respect to feldspars. These serve as temperatures at which the thermodynamic state of the aquifer fluid with respect to other hydrothermal alteration minerals is assessed.

Figure 4.1 presents a comparison of the initial aquifer fluid temperature according to the quartz and Na/K geothermometers described in Section 3.2.3 and Table 3.4. Figure 4.1 shows that there is not a good correspondence between the two temperatures, the Na/K temperatures being systematically ~15°C lower. The discrepancy may be due to error in the thermodynamic data on the feldspars used to calibrate this geothermometer. However, the non-end member activity of both the Na- and K-feldspars may also contribute but compositional data are lacking to verify or disprove this. Data on quartz solubility at temperatures above 300°C is sparse and the various studies are in fairly poor agreement with one another. Since the solubility curve "flattens" out above 300°C, slight differences in the concentration of SiO_2 translate into large differences in quartz equilibrium temperature. Initial aquifer fluid temperatures derived from geothermometry are compared with temperatures measured downhole at the levels of main producing horizons in Table 4.2. The fluids whose temperatures are measured have cooled considerably by depressurization boiling from undisturbed conditions to wellhead. Even so, temperatures inferred from geothermometry are generally very close to measured
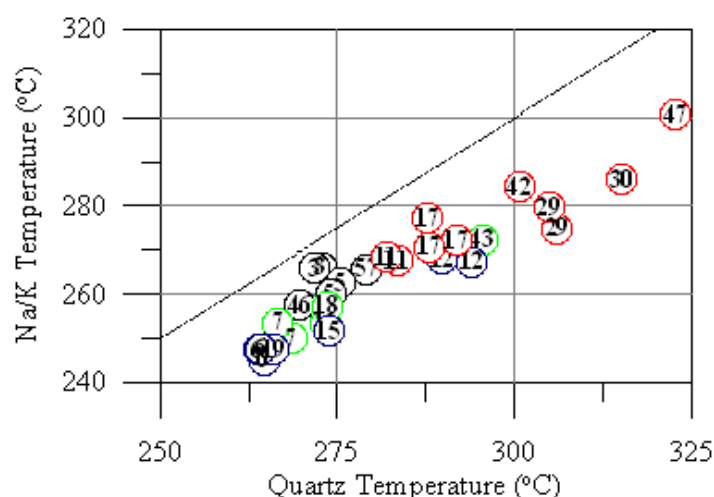

Figure 4.1. Na/K temperature of initial aquifer fluid as described by the formulation of Arnórsson (2000) compared with quartz temperature (Gunnarson and Arnórsson, 2000) under the phase segregation model. Symbology same as above.

42

Table 4.2. Temperatures derived from geothermometry and locations of producing aquifers (primary feedzone shown in italics) and approximate measured temperature in well logs.

Well	$T^f_{qtz,GA}$	$T^f_{Na/K}$	Locations of Productive Horizons (depth m/T °C)
HE-03	272.7	266.0	*950/275*, 1350/275
HE-05	274.0	260.1	*950/275*, 1350/280
HE-06	264.3	247.4	*950/275*
HE-07	266.6	253.5	*950/280*
HE-09	-	275.5	950/280, *1250/305*, 1500/320
HE-11	282	268.4	*900/270*, 1200/280
HE-12	289.8	268.0	900/270, *1250/295*
HE-17	288	270.6	*1150/290*
HE-18	273.5	257.2	*1050/280*
HE-29	304.8	279.7	1500/300, *2000/310*
HE-30	310.4	286.0	*>1800/310*
HE-41	-	277.4	*1850/290*
HE-42	300.6	284.3	*1600/305*
HE-43	295.4	272.4	*1350/290*
HE-46	269.7	257.5	*950/260*
HE-47	322.7	300.5	*850/275*, 2050/305
HE-52	265.6	248.1	*850/250*
HE-57	279.1	265.7	1000/220, *1900/260*

temperatures at the levels of main productive horizons in wells, in most cases, within 5°C, indicating insignificant reequilibration with respect to quartz.

Departure from equilibrium is quantitatively expressed as a saturation index (SI) which relates the reaction quotient/activity product Q with the equilibrium constant as follows:

$$SI = \log \left(\frac{Q}{K}\right)$$

The reaction quotient is defined as:

$$Q = \prod a_i^{v_i}$$

where a_i is the activity of the i-th mineral or aqueous species and v_i is the respective reaction stoichiometric coefficient, which is positive for products and negative for reactants. The thermodynamic database used is essential to the results; both the properties of the species and minerals used to derive the equilibrium constants of the dissolution reactions, as well the speciation calculations from which activity reaction quotients are obtained are dependent on it (Section 3.3).

Figure 4.2 depicts the saturation indices of the initial aquifer fluid with respect to the main calcium bearing minerals: calcite, wollastonite, clinozoisite, epidote and prehnite. The activity of solid-solution minerals was considered in the SI calculations, using analytical data on their compositions from the study area. Their activity was calculated as of 0.26, 0.74 and 0.84 for clinozoisite, epidote and prehnite, respectively (Section 3.3).
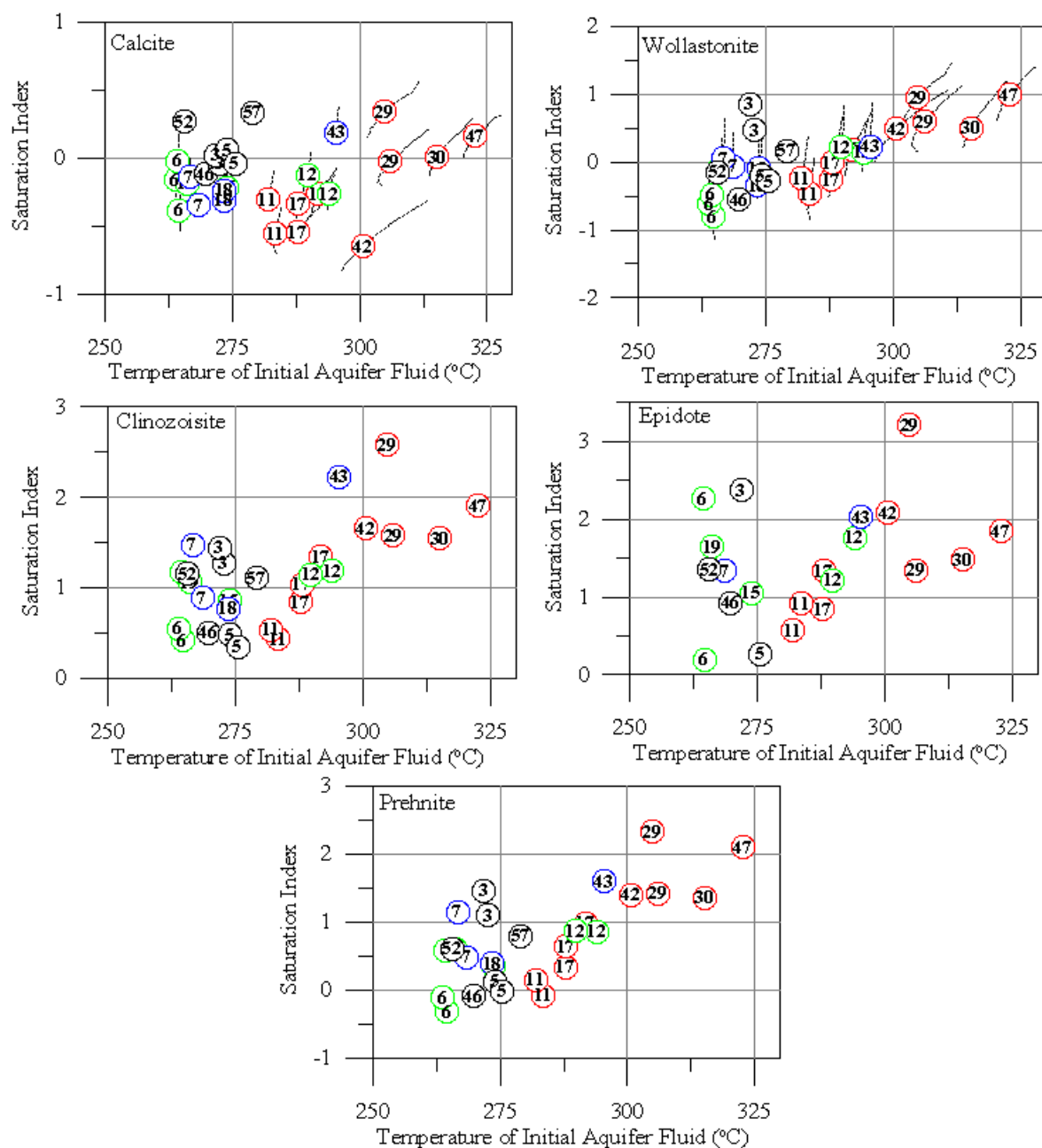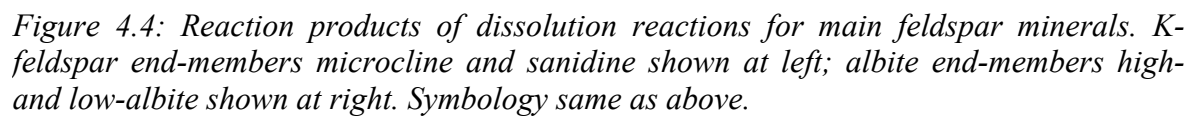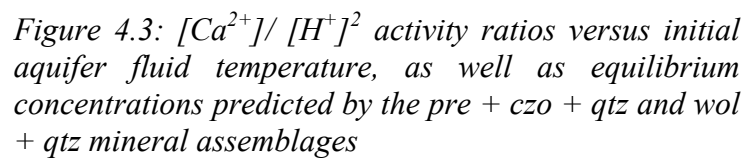
Figure 4.2. Saturation indices of main calcium bearing minerals: calcite, wollastonite, clinozoisite, epidote and prehnite. Symbology same as above. Dashed lines indicate calculation outcomes for different assumed phase segregation pressures.

In general, calculated initial aquifer fluid compositions demonstrate a close approach to equilibrium with respect to calcite, with all modeled aquifer compositions falling within 1 SI unit of equilibrium. The average SI $\pm$ one standard deviation assuming 'mid-point' phase segregation pressure is -0.14 $\pm$ 0.25. Since calcite displays retrograde solubility, an overestimation of the initial aquifer fluid temperature, as is possible for some of the wells $T^f > 300°C$, would result in an underestimation in K and thus an overestimation in SI. The slight systematic undersaturation observed for many of the other well discharges may be the result of the precipitation of calcite from initially saturated solutions during intensive depressurization boiling and cooling upon production. Since this process would deplete Ca^{+2} much, even for limited calcite precipitation, it would cause lower SI values to be calculated. Similar to calcite, wollastonite displays a close approach to equilibrium, although slightly less so, with almost all modeled aquifer compositions falling within 1 SI unit of equilibrium and an average SI of 0.12 $\pm$ 0.48.

Systematic oversaturation is observed for the Ca-Al silicates clinozoisite, epidote and prehnite (of the previously specified end-member activity), which show an average SI of 0.97 +/- 0.98, 1.22 +/- 1.22, and 0.55 +/- 1.06, respectively. For epidote, thermodynamic data on iron speciation may lead to an underestimation of Fe^{+2} activity and corresponding overestimation of $Fe(OH)_4^-$ activity. The systematic oversaturation observed in fluid compositions does not necessarily mean these minerals do not play a role in controlling aquifer fluid compositions; in contrast to calcite, mineral precipitation kinetics could be somewhat slower and the response to slight oversaturation not as pronounced. The role of epidote, clinozoisite and prehnite in the process of water-rock interaction is evidenced by their abundance in well cuttings, as well as by the fairly close correspondence of observed gas concentrations in the initial aquifer fluid to equilibrium concentrations based on mineral assemblages that could buffer these gases, discussed in detail below.

Consideration of the calcium-proton activity ratio allows the saturation state of calcium-bearing silicates to be evaluated by writing their dissolution/precipitation reactions without including Al- and Fe-hydroxy species. The calcium-proton activity ratios are shown in Figure 4.3. This figure indicates that the most of modeled initial aquifer fluid compositions show a close approach to equilibrium with respect to the pre + czo + qtz mineral assemblage, especially if a more Fe-rich clinozoisite composition is assumed. Since wollastonite is not a very abundant alteration mineral, this mineral assemblage is considered most likely to fix $[Ca^{+2}]/[H^+]^2$ activity ratios. The $[Ca^{+2}]/[H^+]^2$ activity ratios are slightly elevated for the high-temperature wells HE-29, HE-30, HE-42 and HE-47 than theoretically predicted, while for many of the other wells (except for HE-03) the ratios fall nearly directly on or slightly below the equilibrium curve. As described above, the latter may be explained, at least partially, by precipitation of calcite during the process of fluid degassing that would cause decrease in Ca^{+2} activities at discharge. The deviation observed in the >300°C wells could also result from a poorly selected reference temperature or errors in calculated pH values of aquifer fluids. The scatter among the rest of the data may also be explained as the result of variable clinozoisite activity between the reservoir.

Figure 4.3: [Ca^{2+}]/ [H^+]^2 activity ratios versus initial aquifer fluid temperature, as well as equilibrium concentrations predicted by the pre + czo + qtz and wol + qtz mineral assemblages

Figure 4.4: Reaction products of dissolution reactions for main feldspar minerals. K-feldspar end-members microcline and sanidine shown at left; albite end-members high- and low-albite shown at right. Symbology same as above.

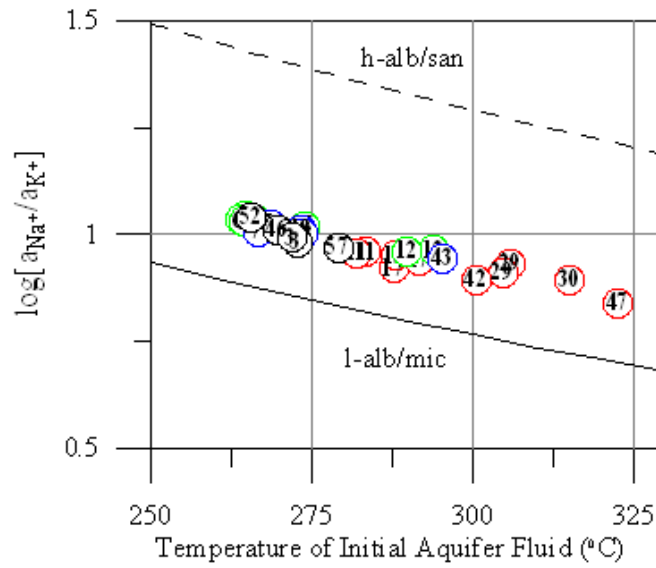*Figure 4.5: [Na+]/[K+] activity ratios versus initial aquifer fluid temperature, as well as equilibrium concentrations predicted by the l-alb/mic and h-alb/san mineral pairs.*
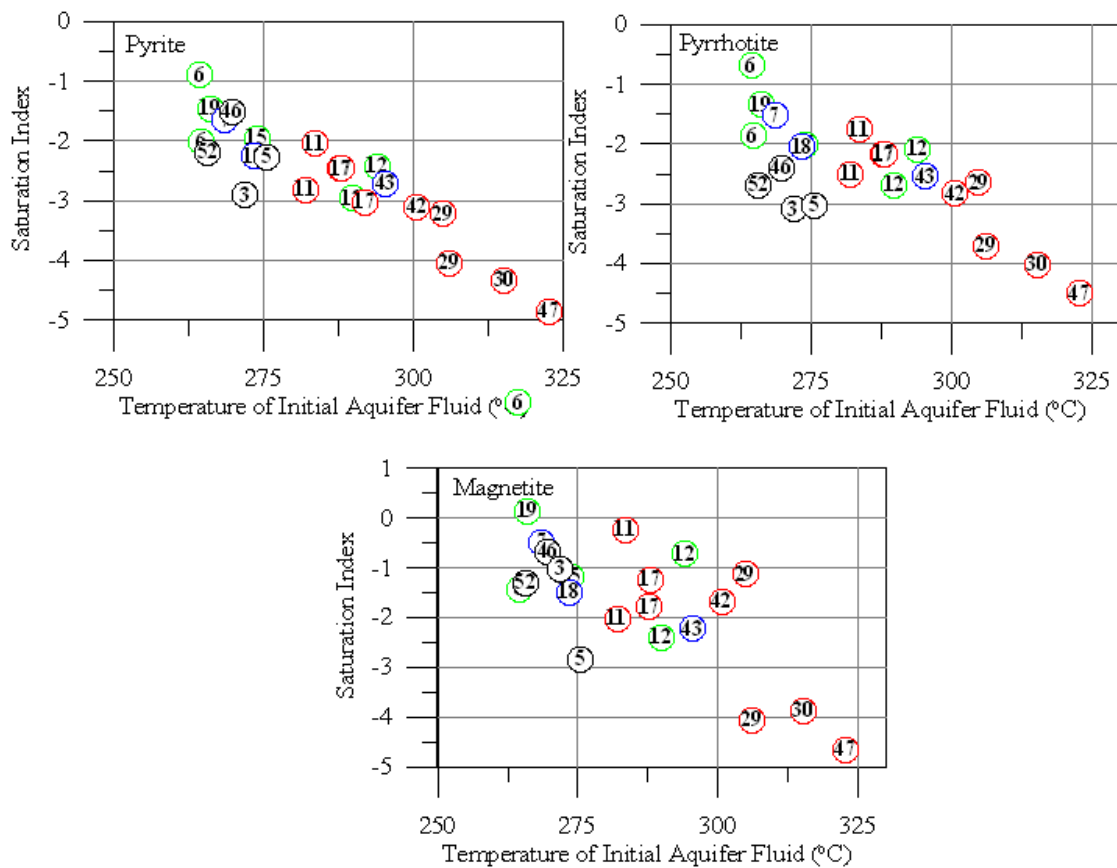

Figure 4.6: Saturation indices of main iron-bearing minerals (pyrite, pyrrhotite, magnetite) versus initial aquifer fluid temperature. Symbology same as above.

The calculated activity products for the dissolution reactions of the feldspar minerals are shown in Figure 4.4 and compared with the equilibrium concentrations based on the end members microcline and sanidine for K-feldspar and high- and low-albite. Most of the calculated activity products for these feldspar reactions fall directly below the equilibrium line for microcline and albite. The departure from equilibrium (~0.1 log units) is well within the limits of error associated with the thermodynamic data for the feldspar minerals. However, it may also be an indication that feldspars of intermediate Al-Si ordering or of non-end member composition are being formed. High-albite and sanidine have a disordered Al-Si arrangement (in contrast to low-albite and microcline), and being formed at temperatures $>800^o$C, are thus unlikely to control aquifer fluid compositions. Microprobe analyses of feldspars taken from well KhG-1 in Kolvidarhóll identify secondary K- and Na-feldspars ranging in composition from Or_{94}–Or_{99} and An_{10}-An_{16}, respectively (Larsson et al., 2002). Figure 4.5 shows the Na^+/K^+ activity ratio versus initial aquifer fluid temperature. The ratio falls in between the equilibrium concentrations predicted by low-albite/microcline and high-albite/sanidine mineral pairs, but closer to the former than the latter. In general, this strongly suggests that calculated Na and K concentrations in the aquifer fluids approach equilibrium with feldspar minerals.

The last group of minerals whose saturation is considered is the Fe-bearing sulfides and oxides, pyrite, pyrrhotite and magnetite, which are shown in Figure 4.6. Similar to the Ca-Al silicates, interpretation of these minerals is hampered by faulty thermodynamic data that leads to an overestimation of the activity of $Fe(OH)_4^-$, and a subsequent underestimation in the activity of Fe^{+2}, in terms of which all of the dissolution reactions for these minerals are written. Past studies of mineral saturation in geothermal systems (ex. Karingithi et al., 2010) have shown a similar trend to what is observed in Figure 4.6, with the minerals appearing to become more undersaturated at higher temperatures. However, this observed trend can be attributed to erroneous thermodynamic data which becomes more problematic at higher temperatures, rather than corresponding to any physical reality. The role of iron-bearing minerals in the process of water-rock interaction can also be evaluated by including these minerals in mineral buffers that control reactive gas concentrations; this will be described in greater detail in the following section.

4.2 Mineral Assemblage-Gas Equilibria

Previous studies have conclusively established that the concentrations of the reactive gases H_2S and H_2 are controlled by equilibrium with respect to specific mineral assemblages (e.g. Arnórsson et al., 2010). Various mineral assemblages may exercise this control. Carbon dioxide can be either equilibrium- or source-controlled in volcanic hydrothermal systems. One difficulty in making the determination of which mineral assemblage is involved is that the equilibrium concentrations of gas predicted by different possible mineral buffers fall within a narrow range, even within the range of uncertainty inherent in the process of fluid sampling and analysis. Additionally, different mineral assemblages have been identified to control reactive gas concentrations in geothermal fields of different geological settings. For example, Angcoy (2010) found that the H_2 concentrations in the silicic volcanics of the Mahanagdong geothermal field in the Philippines best corresponded to a mineral assemblage containing grossular, magnetite, quartz, epidote and wollastonite. However, Karingithi et al. (2010) described that H_2 concentrations in the silicic volcanics of the Olkaria geothermal field in the East African Rift Zone in Kenya best matched equilibrium with a mineral assemblage of either pyrite, pyrrhotite, epidote and prehnite or pyrite, pyrrhotite and magnetite. The latter two mineral

assemblages have been suspected to control reactive gas concentrations in Icelandic geothermal field containing dilute geothermal fluids (e.g. Arnórsson et al., 2010). However, for geothermal fields with saline aquifer fluids, a mineral assemblage containing grossular, quartz, calcite, clinozoisite and wollastonite has been found to control reactive gas concentrations (Giroud, 2007).

The equilibrium curves of the mineral assemblages that could potentially fix the concentrations of the main reactive gases H_2S, H_2 and CO_2 are plotted in Figure 4.7. As is evident in Figure 4.7 and was described above, the equilibrium gas concentrations given by the different mineral assemblages are quite similar throughout the temperature range of interest. For H_2S, the concentrations given by the pyr + pyrr + pre + epi and pyr + pyrr + mag mineral assemblages differ by only 0.13-0.29 log units; for H_2, this difference is only 0.07-0.13 log units. Further, the equilibrium gas concentrations given by the former mineral assemblage assuming unit activity for all minerals is not significantly affected by adjusting the curve for activities of the solid-solution minerals prehnite and epidote. The dashed lines in Figure 4.7 indicate the total variability in calculated gas concentrations as a result of assuming different phase segregation pressure is approximately 0.25-0.5 log units for the high excess enthalpy and dry-steam wells and is slightly less for wells with a lower "excess" enthalpy. For those reasons, it is difficult to distinguish whether the mineral assemblage pyr + pyrr + pre + epi or pyr + pyrr + mag is controlling H_2S and H_2 concentrations.

Past studies of Hellisheidi have concluded that the concentrations of the H_2S species and H_2 are fixed by the pyr + pyrr + pre + epi mineral assemblage (Arnórsson et al., 2010; Stefánsson et al., 2011), citing aeromagnetic studies of Hengill that suggest magnetite is unstable in the hydrothermal system (Björnsson and Hersir, 1981). While many of the wells considered in this study show gas concentrations that correspond closely with this mineral assemblage, many other wells have concentrations that are considerably lower than that predicted by this mineral assemblage. The anomalously low HE-03 point was obtained from Remoroza (2008) and is considered to be attributable to atmospheric contamination of the samples causing oxidation of the H_2S by atmospheric oxygen. There are four possible causes for the apparent low calculated initial aquifer fluid gas concentrations: 1) High estimated aquifer temperatures, 2) Cold recharge and insufficient reaction to bring the concentrations back to equilibrium, 3) Steam loss from the two-phase fluid flowing into wells (degassing), 4) 'Excess' enthalpy generation as a result of conductive heat transfer from the aquifer rock to the flowing fluid. The first cause may be responsible for part of the apparent deviation in calculated concentrations from equilibrium in the hottest well discharges (HE-29, HE-30, HE-42, HE-47), as initial aquifer fluid temperatures >300°C are likely significantly overestimated. As will become more clear in later discussion, some of the liquid enthalpy wells (HE-03, HE-05, HE-46, HE-52) are considered to be affected by the second cause; evidence for this can be seen in the large depletetion in H_2, the relatively high N_2 and the low Cl. The third factor may be impacting HE-03, as relatively low concentrations of all of the low solubility gases are calculated for these wells. As will be described in Section 4.3 in greater detail, the low calculated gas concentrations of the dry-steam wells (HE-41 and HE-45) as well as the wells with T^f>300°C could be a result of conductive heat transfer to the fluid flowing into wells.

With the exception of the well discharges affected by the processes described above, H_2 concentrations are slightly elevated relative to equilibrium with the pyrr + pre + epi + pyr mineral assemblage. One explanation for this is the presence of an equilibrium vapor fraction in the initial aquifer fluid. Table 4.3 shows the calculated equilibrium vapor fractions determined separately for H_2 and H_2S, assuming equilibrium with respect to the
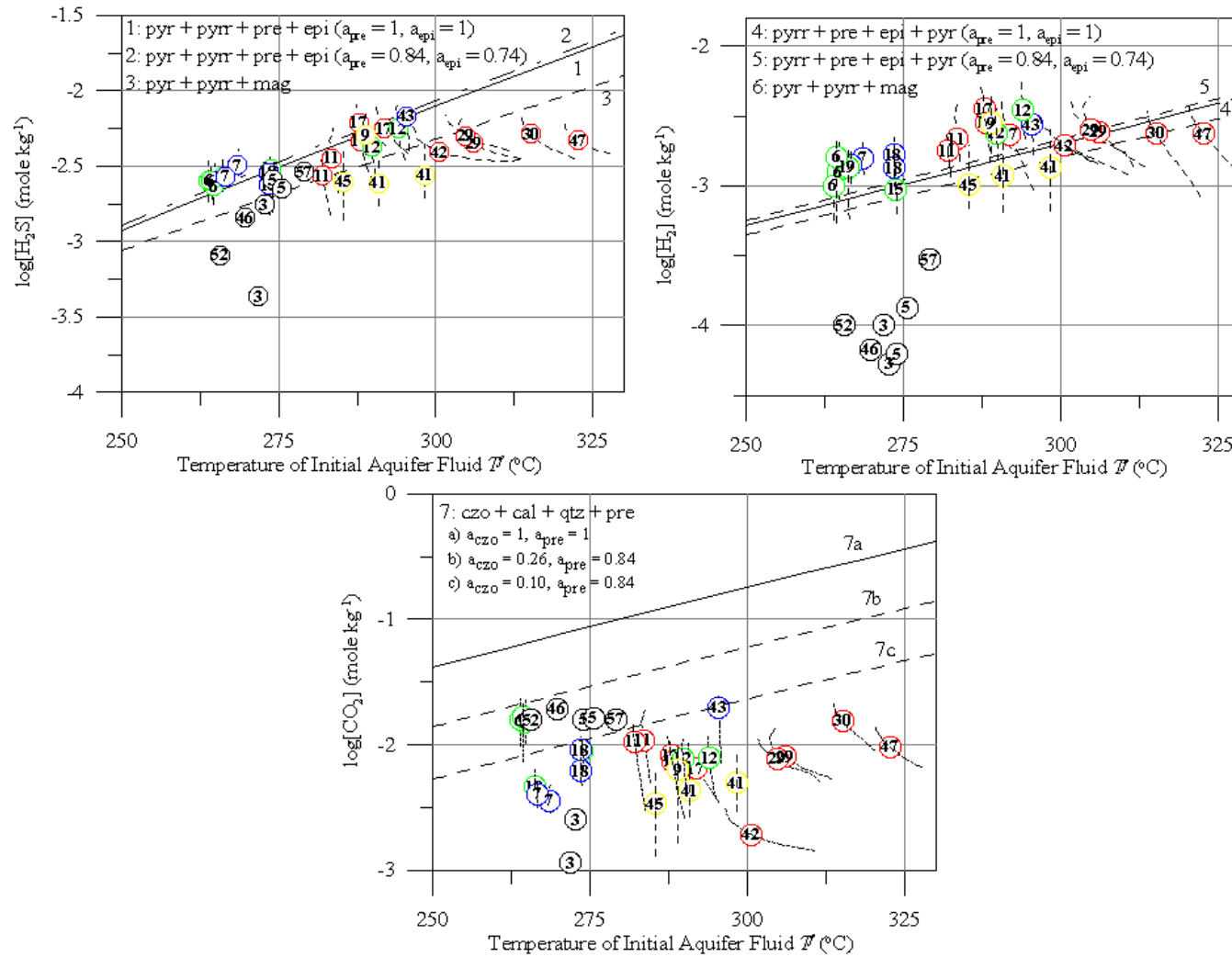
Figure 4.7: Calculated concentration of H₂S, H₂ and CO₂ in initial aquifer fluid under the phase segregation model. Initial aquifer fluids are assumed to be liquid saturated (no vapor fraction). Symbology same as above.

pyr + pyrr + pre + epi mineral assemblage with the previously stated mineral activities and calculated assuming the 'mid-point' phase segregation pressure. As described in Section 3.2.3, H_2 is a much more reliable indicator of equilibrium vapor than H_2S, due to its much lower solubility. As will become more clear in later discussion, some of the liquid enthalpy wells (HE-03, HE-05, HE-46, HE-52) are considered to be affected by cold recharge; evidence for this can be seen in the large depletetion in H_2 the relatively high N_2 and the low Cl. The third factor may be impacting HE-03, as relatively low concentrations of all of the low solubility gases are calculated for these wells. For the dry-steam wells HE-41 and HE-45, the relatively low H_2 concentrations could be a result of conductive heat transfer to the fluid flowing into wells.

With the exception of the well discharges affected by the processes described above, H_2 concentrations are slightly elevated relative to equilibrium with the pyrr + pre + epi + pyr mineral assemblage. One explanation for this is the presence of an equilibrium vapor fraction in the initial aquifer fluid. Table 4.3 shows the calculated equilibrium vapor fractions determined separately for H_2 and H_2S, assuming equilibrium with respect to the pyr + pyrr + pre + epi mineral assemblage with the previously stated mineral activities and calculated assuming the 'mid-point' phase segregation pressure. As described in Section 3.2.3, H_2 is a much more reliable indicator of equilibrium vapor than H_2S, due to its stronger tendency to partition into the vapor phase. Generally, hydrogen concentrations in the initial aquifer fluids suggest the presence of a small equilibrium vapor fraction; a field average of 0.19% by mass was calculated. Almost all samples (except for HE-09, HE-12 and HE-17) showed an $X_{H_2}^{f,v}$ of less than 0.5% by mass. Hydrogen sulfide concentrations indicate a negative equilibrium vapor fraction for many of the wells for which a positive $X_{H_2}^{f,v}$; an field average $X_{H_2S}^{f,v}$ of -1.27% by mass was determined. The only wells in which a negative equilibrium vapor fraction was derived from H_2 were HE-30, HE-41, HE-43, HE-45 and HE-47; these wells also showed the most negative $X_{H_2S}^{f,v}$ values.

It is also instructive to consider mineral buffers that could potentially control the H_2S/H_2 ratio, rather than the individual species concentration. Two potential mineral pairs are shown in Figure 4.8, pyr + mag and pyr + pyrr. The elevated H_2S/H_2 ratio observed in several liquid enthalpy well discharges (HE-03, HE-05, HE-46, HE-52) is attributed to the effects of recharging hydrogen depleted meteoric waters. The H_2S/H_2 ratio would be expected to be lower relative to theoretical equilibrium if the presence of a small equilibrium vapor fraction is included. According to this interpretation, the pyr + pyrr mineral pair better fits the data. Support for this conclusion can be found in the negative magnetic anomaly at Hengill (Björnsson and Hersir, 1981).

All of the carbon dioxide concentrations observed in Figure 5.7 fall well below the equilibrium curve based on the czo + cal + qtz + pre mineral buffer, even if clinozoisite activities as low as 0.1 are considered. This observation led Arnórsson et al. (2010) to conclude that CO_2 in Hellisheidi was source-controlled. The field-scale distribution of CO_2 and the other main gases will be investigated more thoroughly in Section 4.3.

Table 4.3. Calculated equilibrium vapor fractions based on theoretical equilibrium with the pyr + pyrr + pre + epi mineral assemblage with H_2 and H_2S. All "excess" enthalpy wells calculated assuming 'mid-point' phase segregation pressure.

| Sample #	Well	$h^{d,t}$ (kJ kg^{-1})	T^f (°C)	$X_{H_2}^{f,v}$ (wt. %)	$X_{H_2S}^{f,v}$ (wt. %)
10-5085	HE-06	1548	264.3	0.36	1.31
09-5198	HE-06	1548	263.8	0.44	0.78
08-3007	HE-06	1548	264.6	0.19	0.62
10-5169	HE-07	1372	266.6	0.24	3.07
08-3001	HE-07	1372	268.5	0.29	4.35
10-5164	HE-09	2757	288.9	0.57	-0.24
10-5084	HE-11	2047	282.0	0.24	-1.67
08-3004	HE-11	2047	283.5	0.38	-0.93
10-5168	HE-12	1746	289.8	0.38	-1.03
08-3002	HE-12	1746	294.0	0.79	-0.32
10-5082	HE-15	1597	273.8	0.00	0.53
10-5083	HE-17	2054	288.0	0.60	-0.46
09-5199	HE-17	2319	291.8	0.11	1.43
08-3003	HE-17	2319	287.8	0.90	1.79
10-5163	HE-18	1385	273.5	0.17	-0.02
08-3009	HE-18	1385	273.4	0.28	0.90
10-5080	HE-19	1599	266.1	0.23	1.79
09-5197	HE-29	2399	304.8	0.32	-0.30
08-3005	HE-29	2399	306.0	0.09	-4.64
10-5081	HE-30	2173	315.2	-0.19	-6.53
10-5172	HE-41	2704	298.3	-0.17	-4.45
09-5200	HE-41	2704	290.9	0.16	-4.04
10-5171	HE-42	2489	300.6	0.02	-4.00
09-5189	HE-43	1466	295.4	-0.11	-3.35
10-5170	HE-45	2498	285.4	-0.10	-2.56
10-5079	HE-47	2139	322.7	-0.46	-9.07
		AVERAGE		**0.19**	**-1.27**
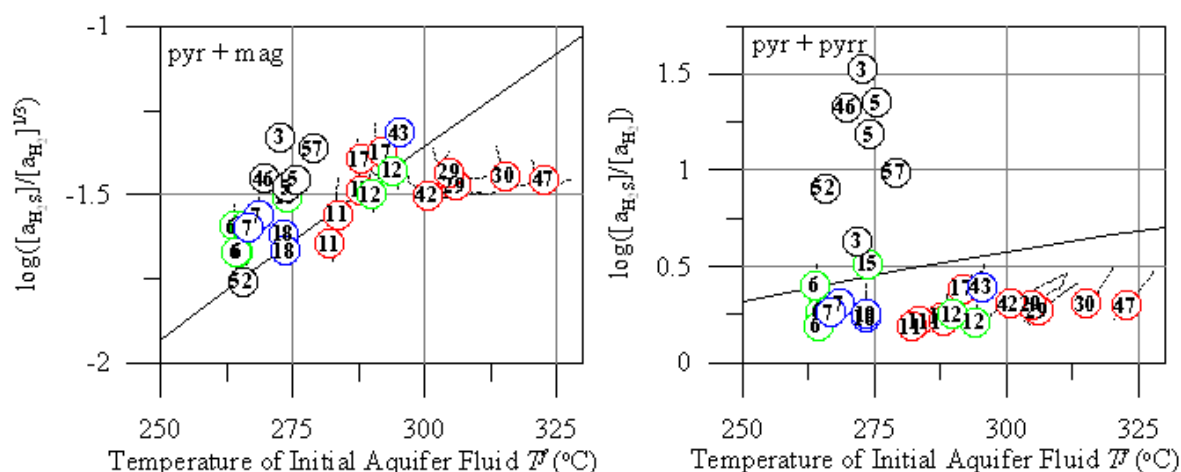
Figure 4.8. Calculated H_2S/H_2 activity ratios compared with theoretical equilibrium with pyr + mag and pyr + pyrr mineral pairs. Symbology same as above.

4.3 Field Scale Distribution

As was shown in Figure 3.1, the majority of the wells sampled in this study are confined to a fairly small area close to the eruptive fissure of ~1100 years b.p. In this section, insight gained from discharge enthalpy, temperature and pressure measurements will be discussed along with the field-scale distribution of the main gases and chloride. The objective is to integrate these forms of data into a conceptual model of the hydrothermal system.

Temperature and pressure logs were made available by Orkuveita Reykjavíkur for most of the 21 wells considered in this study. Some of these wells show clear temperature reversals around 1000 meters depth (HE-03, HE-06, HE-07, HE-18, HE-19). Quartz equilibrium temperatures match well measured temperature maxima in these wells, indicating that they represent feedzones (see Table 4.2). Wells drilled near the eruptive fissure of ~1100 b.p. do not show such reversals (HE-29, HE-30, HE-42, HE-47), and also have higher quartz equilibrium temperatures (>300°C), suggesting deeper feedzones. There is some correlation between well discharge enthalpy and feedzone temperature. In particular, the wells in the proximity of the eruptive fissure have discharge enthalpies in excess of 2100 kJ kg^{-1}, with two even discharging dry steam (HE-41, HE-45). The only other dry steam well in Hellisheidi is HE-09. Three wells close to HE-09 (HE-11, HE-12, HE-17) have enthalpies between 1750-2050 kJ kg^{-1}. Remaining wells have discharge enthalpies <1600 kJ kg^{-1}, with those located on the margins of the production field showing liquid enthalpy (HE-03, HE-05, HE-46, HE-52, HE-57). Pressure logging in HE-29, HE-42 and HE-47 indicates a low density, vapor-rich fluid down to the well bottom (~2 km depth). The low density of this fluid inevitably results in an upflow zone. A separate upflow zone with similar characteristics may exist in the vicinity of HE-09, apparently with somewhat shallower feedzones.

As was shown in the previous section, the concentrations of H_2S and H_2 are equilibrium controlled, with elevated concentrations of the latter especially indicating an equilibrium vapor fraction in the initial aquifer fluid. The data points in Figure 4.7 can be divided into several groups. The largest group consists of excess enthalpy well discharges with H_2S and H_2 concentrations at or, in the case of the latter gas, slightly above the equilibrium curve of the assemblage pyrr + pre + epi + pyr. Many of these wells have the relatively shallow feedzones (~1000 m depth) and temperature reversals described above. The high enthalpy, high temperature wells located in the proximity of the eruptive fissure make up the second group. Compared to the previous group, the H_2 and H_2S concentrations of these wells are lower and tend to fall below the equilibrium curve (with the exception of HE-29), which is especially evident for the latter gas. The low calculated gas concentrations may be an artifact of the faulty assumption that all of the excess discharge enthalpy was produced by the process of phase segregation. Due to the fact these wells have deeper feedzones and discharge a fluid dominantly consisting of saturated steam, conductive heat transfer from the rock to the fluid flowing into wells may be more of a factor than for the previous group. If a significant proportion of the 'excess' enthalpy of these discharges is the result of conductive heat transfer, the phase segregation model would tend to calculate lower-than-true gas concentrations. When the effect of conductive heat transfer is taken into consideration for one of the gases (either H_2S or H_2), bringing its calculated concentration up enough to match the population described by the first group (either close to equilibrium for H_2S or slightly above equilibrium for H_2), the calculated

concentration of the other gas increases sufficiently to match its population in the first group. Thus, this process best explains the low equilibrium vapor fractions of the wells in the upflow zone compared to those in the outflow zone. The last group consists of liquid enthalpy wells located on the margins of the main producing area, all of which show far below equilibrium H_2 and H_2S concentrations. Based on further evidence from N_2 and Cl discussed below, the low gas concentrations of these wells are best explained either by mixing with shallow recharging fluids or degassing.

The field scale distributions of H_2S and H_2 are shown in Figures 4.9 and 4.10, respectively. Especially for H_2, the highest concentrations of these gases are calculated in the proximity of the proposed upflow zones, where the highest temperatures are found (see Figure 2.5). It is apparent that somewhat low gas concentrations are calculated in the Helliskard area, near the two dry steam wells HE-41 and HE-45. As described above, the upflow zone associated with the eruptive fissure of ~1100 b.p. is thought to be continuous throughout this area from Reykjafell to the north of Kolvidarholl, and the apparent low gas concentrations are related to the contribution of conductive heat transfer to excess discharge enthalpy described above. The more northern H_2 and H_2S maxima extend eastward to wells not drilled in close proximity to the eruptive fissure (HE-09, HE-12, HE-17). In addition to the well logging data described above, these high gas concentrations are suggestive of a second upflow zone. Comparatively low gas concentrations are found in the wells with the temperature reversals (HE-03, HE-06, HE-07, HE-18, HE-19), which are located in the outflow paths of these upflow zones. The lowest gas concentrations are found in the liquid enthalpy wells in the northern part of the field (HE-46, HE-52, HE-05).

In contrast to H_2S and H_2, both CO_2 and N_2 are not equilibrium but instead source controlled. In the case of the former, its source is dissolution of basaltic rock, magma degassing or the dissolution of hydrothermal calcite precipitated in an earlier stage of the geothermal system; for the latter, recharging air-saturated meteoric water. Concentrations in aquifer fluids can also be affected by degassing prior to entering the producing zone of a well. In most of the upflow and outflow wells, aquifer fluid N_2 concentrations are far below that of air-saturated water (~19 ppm). While H_2S and H_2 are generated by reactions with the rock that can bring their concentrations back to equilibrium after degassing has occured, CO_2 and N_2 remain low after even a small fraction of steam has been lost. Since N_2 concentrations are low while the calculated concentrations of H_2 and H_2S are close to equilibrium, it is likely most aquifer fluids have undergone degassing. During the process of descent along the sub-vertical fractures that serve as the main recharge channels for the reservoir, meteoric water is heated up close to the boiling point at relatively shallow depths (~500 m). Nitrogen will strongly partition into the vapor phase if a small fraction of steam has been generated, and this steam will have a strong tendency to rise and separate from the descending liquid. Additionally, degassing could be occurring nearly continuously in the fluids within the upflow zone, which have already been shown to contain a small vapor fraction ~0.2 by mass. This process is expected to account for the low N_2 and CO_2 concentrations observed in the up- and outflow wells. However, in well HE-03, N_2 is low as are other low-solubilty gases (H_2); the likely cause of this is steam loss from the fluid while flowing into this well.

The distributions of CO_2 and N_2 on the scale of the geothermal field are shown in Figures 4.12 and 4.13, respectively. Carbon dioxide concentrations are constrained to a local maximum at the southern end of Skardsmýrarfjall below Hamragil (HE-05, HE-06, HE-11). The liquid enthalpy well discharges HE-46 and HE-52 in the north and HE-03 in
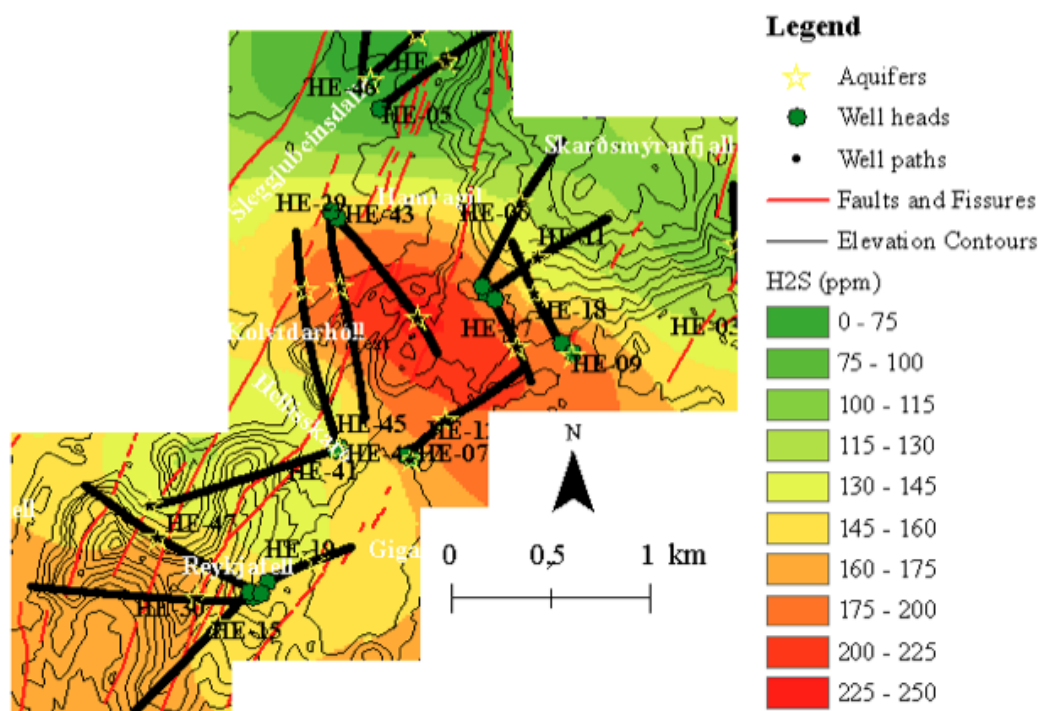
Figure 4.10. Field-scale distribution of H₂S throughout the Hellisheidi geothermal field.
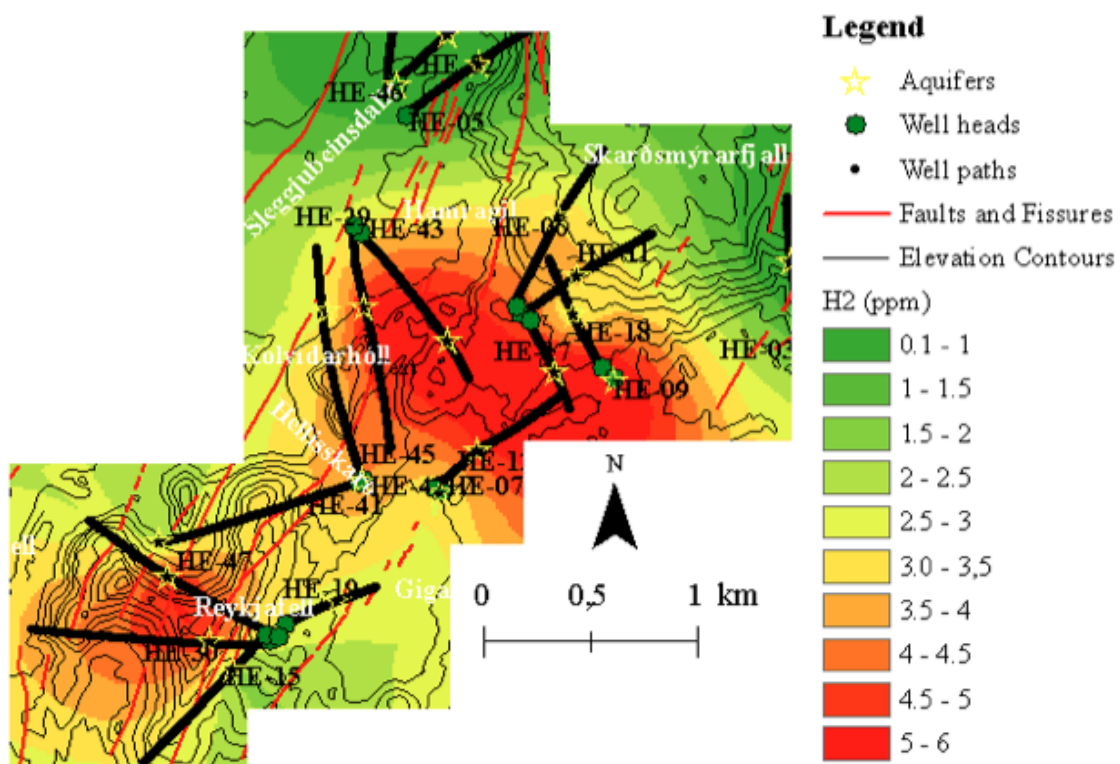

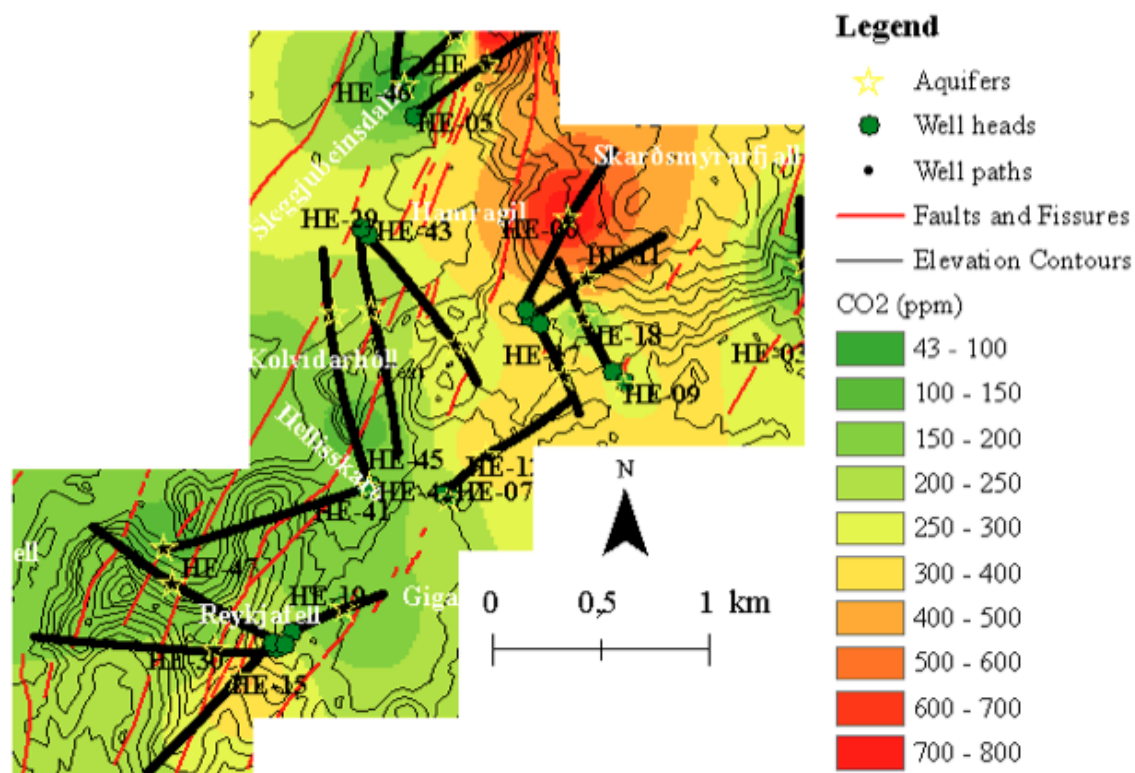*Figure 4.9. Field-scale distribution of H₂ throughout the Hellisheidi geothermal field.*

Figure 4.11. Field-scale distribution of CO$_2$ throughout the Hellisheidi geothermal field.
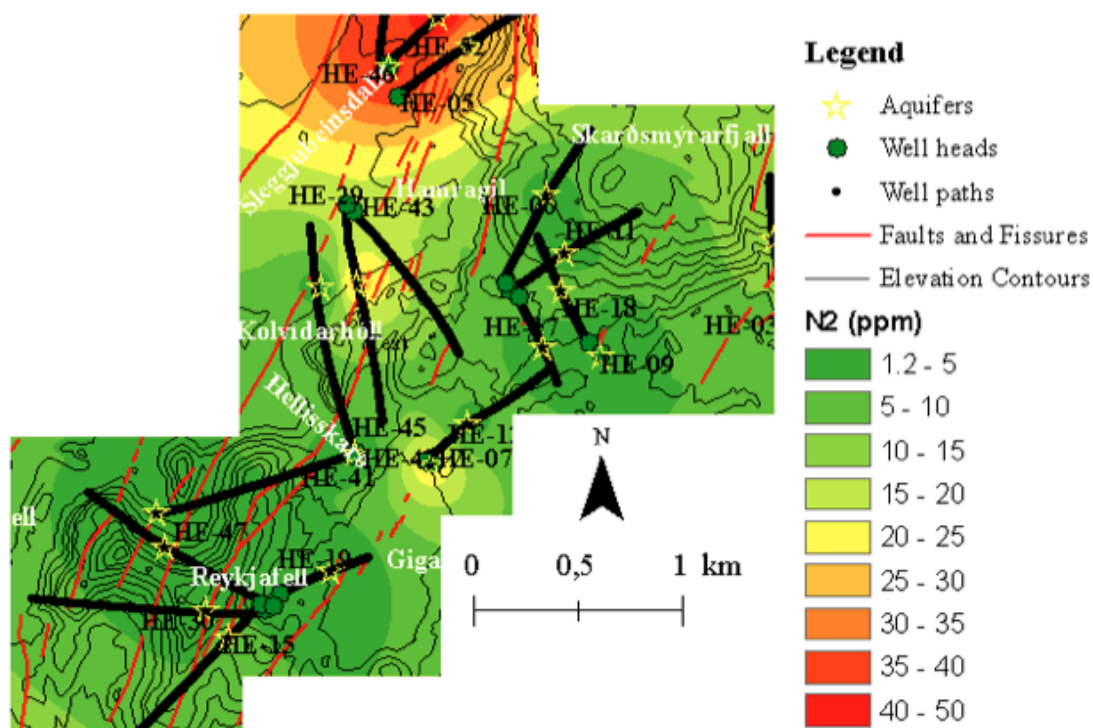

Figure 4.12. Field-scale distribution of N$_2$ throughout the Hellisheidi geothermal field.
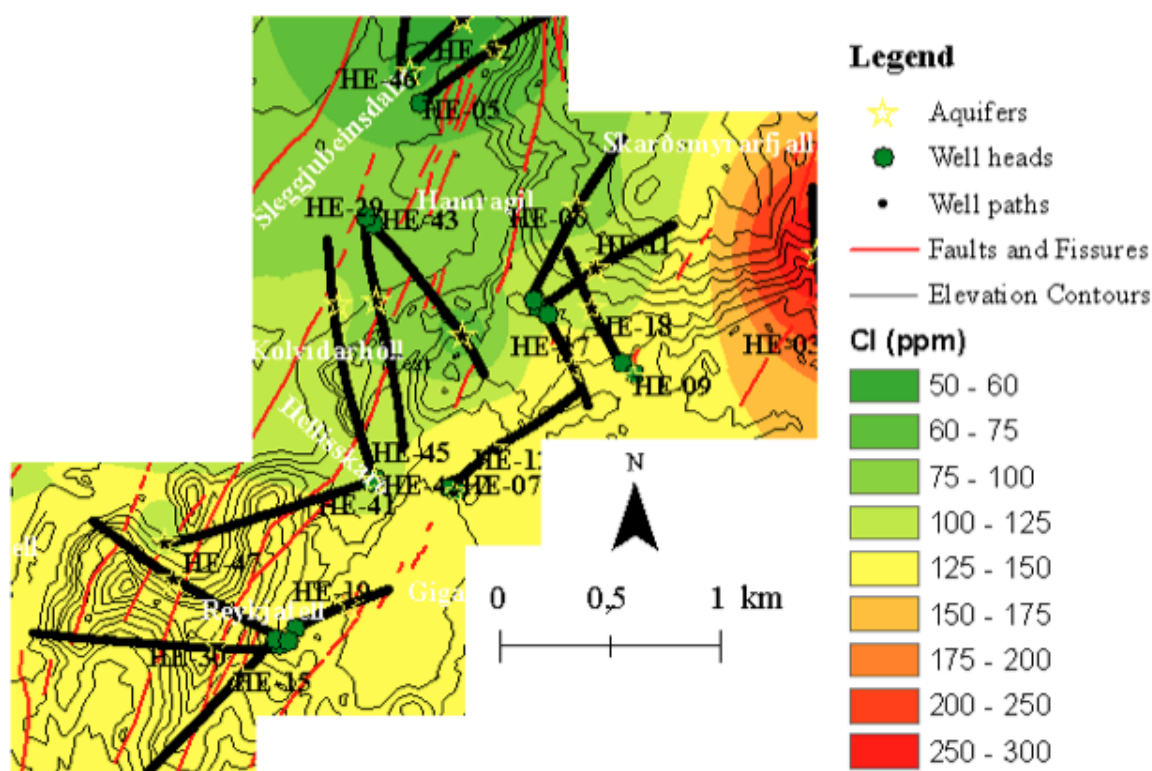
Figure 4.13. Field-scale distribution of Cl throughout the Hellisheidi geothermal field.

the east show relatively low CO_2 concentrations, but HE-57 in the south has high CO_2 concentrations relative to the field average. The N_2 maximum exists in the liquid enthalpy wells in northern part of the field (HE-05, HE-46, HE-52), in the same areas where H_2S and H_2 were found to be lowest. The elevated N_2 contents of HE-46, HE-52 and HE-05 strongly suggest mixing with shallow meteoric water, indicating the presence a recharge zone directed from the north towards the south. It is not understood what processes have led to concentrations in excess of that of air-saturated water. However, if this serves as recharge zone for the deep fluid below the upflow, then degassing with respect to N_2 must occurr between this recharge zone and the source fluid below the upflow.

Recharging meteoric waters would be expected to have relatively low Cl, in addition to being elevated in N_2, since the main source of Cl in aquifer fluids is progressive dissolution of the host rock. As can be seen from Figure 4.13, which shows the field scale distribution of Cl, the low Cl in the liquid enthalpy wells to the north (HE-05, HE-46, HE-52) accords well with this idea. The recharge zone appears to extend further to the south as well, as HE-29, HE-43, HE-06 and HE-11 all show relatively low Cl. By far, the highest Cl can be seen in the liquid enthalpy well HE-03 far to the east. By considering the Cl/B mass ratio of sampled fluids (Figure 4.14), it appears clear that this well has a slight seawater component that is accounting for the high Cl. Past studies the have shown that a seawater component is present in all of wells in the Hveragerdi field, which lies about 10 km to the east of HE-03 (Arnórsson and Andrésdóttir, 1995). It is concluded that the signal of this seawater component is retained as far east as HE-03, but not into the main producing area of the Hellisheidi field, where most of the samples have Cl/B ratios that correspond closely with that of the average Icelandic tholeiitic basalt (Arnórsson and Andrésdóttir, 1995), indicating congruent rock dissolution.

The Cl/B ratio has also been considered by plotting the molar ratio against discharge enthalpy (Figure 4.15). As can be seen in both Figure 4.14 and 4.15, many of the
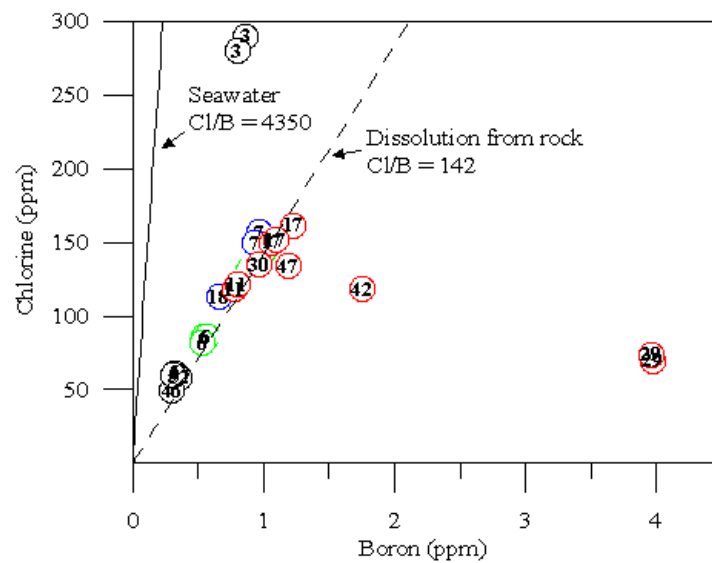
Figure 4.14. Chlorine and boron concentrations in aquifer fluids of all samples considered in this study, compared with average ratio in Icelandic tholeiitic basalt and seawater (Arnórsson and Andrésdóttir, 1995).
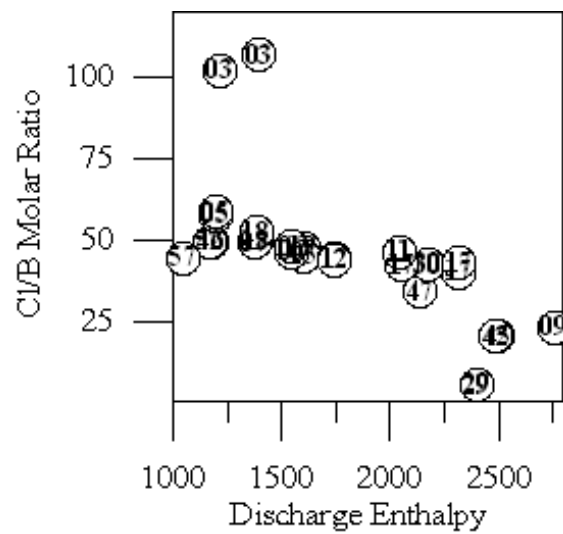

Figure 4.15. Chlorine and boron molar ratio versus well discharge enthalpy.

58

highest excess enthalpy wells are quite elevated in boron relative to the average composition of the Hellisheidi field, where most of the samples have Cl/B ratios that correspond closely with that of the average Icelandic tholeiitic basalt (Arnórsson and Andrésdóttir, 1995), indicating congruent rock dissolution.

The Cl/B ratio has also been considered by plotting the molar ratio against discharge enthalpy (Figure 4.15). As can be seen in both Figure 4.14 and 4.15, many of the highest excess enthalpy wells are quite elevated in boron relative to the average composition of Icelandic tholeiitic basalt. In general, the overall trend exhibited in Figure 4.15 is that the Cl/B ratio decreases with increasing discharge enthalpy. One mechanism that can enrich boron in well discharges relative to aquifer fluids is high vapor/liquid ratios at high temperatures. At temperatures >300°C, boron has a stronger tendency to partition into the vapor phase than chlorine, and subsequent cooling (by depressurization) of vapor that has separated from fluids that have congruently dissolved basalt could lead to enrichment of boron in the liquid phase of well discharge fluids (Arnórsson and Andrésdóttir, 1995). It is believed that this process, instead of the alternative explanation of degassing of boron from a magmatic heat source, best accounts for the Cl/B ratios of the excess enthalpy wells that fall significantly below the rock ratio.

A tracer test was recently conducted in the vicinity of the proposed recharge zone for the purpose of evaluating the site as the location of a H_2S injection and sequestration experiment (Gunnarsson et al., 2011). A concentrated sodium benzoate solution was injected in HE-08, a vertically drilled well situated on the same platform as HE-46 and HE-52. A monitoring regime was set up that included these two wells as well as HE-05 and HE-31, the latter of which is located directly to the south of HE-08. The only well in which the tracer was detected was HE-46, whose main feedzone is approximately 450 m away from the injection site. The first measurable concentration of tracer was detected less than two days after injection commenced, with peak concentrations measured approximately 2.5 days thereafter. Modeling of tracer flow parameters using the TRACINV software (Arason et al., 2004) indicate 30-40% tracer recovery in this well. This study highlights the high permeability that can exist in this area.

Reinjection at the Hellisheidi field is currently taking place at Gráhnúkar, an area located to the southwest of HE-30 and HE-15, with the obvious intention to recharge the highly-productive part of the field further to north (Gunnarsson, 2011). The data presented in this study suggests no recharge zone in the southern part of the field. Instead, it seems more likely for injected fluids to mix with outflowing fluids from the proposed upflow zone near Reykjafell and flow towards the south. This may partially explain why HE-57 shows both high nitrogen and relatively high chloride. The effect of relatively cool injected fluids would also account for the relatively low productivity of HE-57 and the fact that the enthalpy of this well has recently been revised downward. Due to the surprisingly high measured temperatures (>300°C) and discharge enthalpies (>2000 kJ kg^{-1}) of the injection wells in Gráhnúkar, there are plans to move the reinjection zone to the Húsmúli area to the west of Sleggubeinsdalur (Gunnarsson, 2011). In light of the evidence of a recharge zone in this area presented in this study, this location appears more promising for reinjection. However, reinjection efforts may be even more successful directly to the north of Sleggubeinsdalur.

5 Conclusions

This thesis has primarily focused on the processes controlling the concentrations of chemical components, especially gases, in the aquifer fluids of the Hellisheidi geothermal field. The overall objective of this thesis was to use these investigations to elucidate the physical nature of the hydrothermal system. For this reason, the chemical discussion was preceded by an intensive discussion of the geology of the Hengill area, including the tectonic factors that shape the evolution of the hydrothermal system, and the lithology and alteration mineralogy of the reservoir rock. While this review reveals the great advances in understanding the nature of the system that have been made in the past decades, surface geological investigations and various geophysical exploration methods have been somewhat limited in their ability to resolve features of the hydrothermal system on the scale important for the geothermal reservoir engineer. The nature of geothermal development is that this is only possible once a resource has been as extensively drilled as the Hellisheidi field. It is hoped that this study can serve as an example of how geochemistry can be employed in this way for geothermal resource assessment of a field like Hellisheidi.

This study is based on 33 samples from all of the 21 currently producing wet-steam wells. Eighteen samples were collected in 2010 as part of the present study, 6 analyses are from Remoroza (2010) and 9 from Stefánsson et al. (2010). A significant portion of this thesis focused on how aquifer fluid compositions were calculated based on chemical analyses of the two phases performed at the surface. It was shown that the process of phase segregation, caused by the retention of liquid onto mineral grain surfaces, best accounts for the observed discharge enthalpies of wet-steam wells in the Hellisheidi field. The main uncertainty of the phase segregation model involves the selection of a single pressure at which this process occurs. Selection of a phase segregation pressure approximately in between that of the initial aquifer fluid and the wellhead was deemed appropriate, since the liquid saturation at this pressure was calculated to roughly match the residual liquid saturation in porous and fractured media (0.2-0.3). However, the overall approach taken by this study was to calculate initial aquifer fluids chemical compositions assuming a range of different phase segregation pressures. While the calculated concentration of non-volatile components in initial aquifer fluids is not sensitive to the selected phase segregation pressure, the calculated concentration of gaseous components is markedly more sensitive. Once a phase segregation pressure was selected, the chemical composition and speciation of initial aquifer fluids was calculated using the WATCH program.

Generally, the calculated chemical compositions of initial aquifer fluids show close approach to equilibrium with main hydrothermal alteration minerals. Assuming the 'mid-point' phase segregation pressure, the average saturation indices of the calcium-bearing alteration minerals calcite, wollastonite, epidote, clinozoisite and prehnite were found to be -0.14, 0.12, 1.22, 0.97 and 0.56. The calcium-proton activity ratio was shown to be controlled by a mineral assemblage consisting of prehnite, clinozoisite and quartz. The sodium-potassium activity ratios differ systematically from equilibrium with respect to the feldpsars microcline and low-albite. However, the difference amounts to less than 1000 J mole^{-1}, which is well within the limit of error of the thermodynamic data used to calculate the equilibrium constant for the reaction between low-albite, microcline and solution. The

saturation state of the Fe-bearing alteration minerals pyrite, pyrrhotite and magnetite could not be meaningfully evaluated due to faulty thermodynamic data for aqueous iron species.

The concentrations of H_2S and H_2 generally seem to be controlled by close approach to equilibrium with respect to a mineral assemblage consisting of pyrite, pyrrhotite, prehnite and epidote. The elevated H_2 concentrations found in most total aquifer fluids relative to equilibrium with liquid water indicate the presence of a small equilibrium vapor fraction in the initial aquifer fluid, approximately 0.2% by mass. Some of the well discharges – especially the high temperature, high excess enthalpy wells located in proximity to the main upflow zone, and the liquid enthalpy wells located on the margins of the field – show calculated H_2S and H_2 concentrations significantly below equilibrium. For the former wells, the best explanation for the low calculated gas concentrations is that a significant part of the excess enthalpy of these well discharges results from conductive heat transfer from the aquifer rock to the fluid flowing into wells. For the latter wells, the low gas concentrations results from mixing of aquifer fluids with shallow, recharging meteoric waters, and in the case of HE-03, steam loss from the fluid during horizontal flow into the producing well. However, in general, calculated gas concentrations are highest in the proximity of the two proposed upflow zones: 1) near the eruptive fissure of ~1100 b.p., in alignment with the axial fissure swarm from Reykjafell towards the NE 2) on the southern margin of Skardsmýrarfjall, to the southeast of Hamragil.

In contrast to H_2S and H_2, the concentrations of CO_2 and N_2 are source-controlled. The concentrations of CO_2 were found to be highest in the northern part of field, close to Skardsmýrarfjall. A possible source of CO_2 is the dissolution of calcite that formed there during a previous stage of the hydrothermal system when CO_2 concentrations and temperatures were higher. The aquifer fluids in the up- and outflow zones have N_2 concentrations below that of air-saturated water, suggesting that meteoric waters undergo some degree of degassing during the process of recharge. This process may also partially explain the low CO_2 concentrations observed in these wells as well. The high N_2 in the liquid enthalpy wells to the north results from mixing with shallow, recharging, air-saturated meteoric waters – this area is believed to serve as the main recharge zone. This interpretation is supported by the low Cl concentrations in these aquifer fluids. For most of the wells, the concentrations of the conservative components Cl and B are controlled by progressive, congruent dissolution of the reservoir rock. However, the elevated Cl contents in HE-03, on the far eastern margin of the geothermal system, are explained by a small seawater component in the aquifer fluid, while the elevated B in the highest excess enthalpy wells is due to partitioning of B into the vapor phase at high temperatures.

This study supports the interpretation that upflow zones in the Hengill area are numerous and confined to relatively small regions that correspond to loci of significant volcanic or intrusive activity. Selection of sites for future drilling efforts must be performed with great care. In general, the sampled area of the hydrothermal field has been extensively drilled. Increasing production from the main upflow zone may risk pressure decline and resultant lower produced fluid temperatures. One area that might be worthy of attention in future drilling efforts is the southern boundary of the second upflow zone. The need to harness existing upflow zones effectively and locate new ones (as may be found in Gráhnúkar or Hverahlíd) is reinforced by the idea that ~20 new wells within the next 5 years are needed to maintain production at 300 MWe, once the planned expansion has occurred.

References

Angcoy, E., 2010. Geochemical Modelling of the High-Temperature Mahanagdong Geothermal Field, Leyte, Philippines. MSc Thesis, Faculty of Science, University of Iceland.

Ármansson., H., Benjaminsson, J., and Jeffrey, A. W. A., 1989. Gas Changes in the Krafla Geothermal System, Iceland. Chem Geol 76, 175-196.

Árnason, K.., Eysteinsson, H., and Hersir, G. P., 2010. Joint 1D inversion of TEM and MT data and 3D inversion of MT data in the Hengill area, SW Iceland. Geothermics 39, 13-34.

Árnason, K.., Haraldsson, G. I., Johnsen, G. V., Hersir, G. P., Thorbergsson, G., Saemundsson, K., Georgsson, L. S., Rognvaldsson, S. T., and Snorrason, S. P., 1987. Nesjavellir - Olkelduhals, Yfirbordsrannsoknir 1986 (Nesjavellir - Olkelduhals, Geophysical Studies 1986). Orkustofnun, Reykjavík, Iceland.

Árnason, K.., Haraldsson, G. I., Johnsen, G. V., Thorbergsson, G., Hersir, G. P., Saemundsson, K., Georgsson, L. S., and Snorrason, S. P., 1986. Nesjavellir, Jardfraedi- og jardedlisfradileg konnun 1985 (Nesjavellir, Geological and Geophysical Investigations 1985). Orkustofnun, Reykjavík, Iceland.

Árnason, K.. and Magnusson, I. T., 2001. Jardhiti vid Hengil og a Hellisheidi - Nidursodur vidnamsmaelinga (Geology of Hengill and Hellisheidi - Resistivity Studies). Orkustofnun, Reykjavík, Iceland.

Arnórsson, S., 1995. Geothermal systems in Iceland: Structure and conceptual models .1. High-temperature areas. Geothermics 24, 561-602.

Arnórsson, S. and Andresdóttir, A., 1995. Processes Controlling the Distribution of Boron and Chlorine in Natural Waters in Iceland. Geochim Cosmochim Ac 59, 4125-4146.

Arnórsson, S. and Andresdóttir, A., 1999. The dissociation constants of Al-hydroxy complexes at $0-350^oC$ and P_{sat}:. In: Ármansson., H. (Ed.),5th Intl Symp. on Geochemistry of the Earth's Surface., Balkema, Rotterdam.

Arnórsson, S. and Andresdóttir, A., 2000. Water-Rock Interaction and Equilibration Between Geothermal Waters and Hydrothermal Minerals. World Geothermal Congress, Kyushu - Tohoku, Japan.

Arnórsson, S., Angcoy, E., Bjarnason, J. O., Giroud, N., Gunnarsson, I., Kaasalainen, H., Karingithi, C. W., and Stefánsson, A., 2010. Gas Chemistry of Volcanic Geothermal Systems. World Geothermal Congress, Bali, Indonesia.

Arnórsson, S., Bjarnason, J. Ö., Giroud, N., Gunnarsson, I., and Stefánsson, A., 2006. Sampling and analysis of geothermal fluids. Geofluids 6, 203-216.

Arnórsson, S., Björnsson, S., Muna, Z. W., and Ojiambo, S. B., 1990. The use of gas chemistry to evaluate boiling processes and initial steam fractions in geothermal reservoirs with an example from the Olkaria field, Kenya. Geothermics 19, 1307-1325.

Arnórsson, S. and Gunnlaugsson, E., 1985. New gas geothermometers for geothermal exploration - calibration and application. Geochim Cosmochim Ac 49, 1307-1325.

Arnórsson, S., Gunnlaugsson, E., and Svavarsson, H., 1983a. The Chemistry of Geothermal Waters in Iceland .2. Mineral Equilibria and Independent Variables Controlling Water Compositions. Geochim Cosmochim Ac 47, 547-566.

Arnórsson, S., Gunnlaugsson, E., and Svavarsson, H., 1983b. The Chemistry of Geothermal Waters in Iceland .3. Chemical Geothermometry in Geothermal Investigations. Geochim Cosmochim Ac 47, 567-577.

Arnórsson, S. and International Atomic Energy Agency., 2000. Isotopic and chemical techniques in geothermal exploration, development and use : sampling methods, data handling, interpretation. International Atomic Energy Agency, Vienna.

Arnórsson, S., Sigurdsson, S., and Svavarsson, H., 1982. The Chemistry of Geothermal Waters in Iceland .1. Calculation of Aqueous Speciation from O-Degree-C to 370-Degree-C. Geochim Cosmochim Ac 46, 1513-1532.

Arnórsson, S. and Stefánsson, A., 1999. Assessment of feldspar solubility constants in water in the range 0 degrees to 350 degrees C at vapor saturation pressures. Am J Sci 299, 173-209.

Arnórsson, S. and Stefánsson, A., 2005. Wet-Steam Well Discharges. II. Assessment of Aquifer Fluid Compositions. World Geothermal Congress, Antalya, Turkey.

Arnórsson, S. and Stefánsson, A., 2007. Fluid-fluid interactions in geothermal systems. Rev Mineral Geochem 65, 259-312.

Björnsson, A. and Hersir, G. P., 1981. Geophysical Reconnaissance Study of the Hengill High-Temperature Geothermal Area, SW-Iceland. Geothermal Resources Council, Transactions 5, 55-58.

Björnsson, A., Hersir, G. P., and Björnsson, G., 1986. The Hengill High-Temperature Area SW-Iceland: Regional Geophysical Survey. Geothermal Resources Council, Transactions 10, 205-210.

Björnsson, G., Gunnlaugsson, E., and Hjartarson, A., 2006. Applying the Hengill Geothermal Reservoir Model in Power Plant Decision Making and Environmental

Impact Studies. TOUGH Symposium Lawrence Berkeley National Laboratory, Berkely, California.

Björnsson, G., Hjartarson, A., Bodvarsson, G. S., and Steingrimsson, B., 2003. Development of a 3-D Geothermal Reservoir Model for the Greater Hengill Volcano in SW-Iceland. TOUGH Symposium, Lawrence Berkeley National Laboratory, Berkeley, California.

Chen, C.-Y., Horne, R. N., and Fourar, M., 2004. Experimental Study of Two-Phase Flow Structure Effects on Relative Permeabilities in a Fracture. Twenty-Ninth Workshop on Geothermal Reservoir Engineering, Stanford University, Stanford, CA.

D'Amore, F. and Celati, R., 1983. Methodology for calculating steam quality in geothermal reservoirs. Geothermics 12, 129-140.

D'Amore, F. and Truesdell, A. H., 1985. Calculation of geothermal reservoir temperatures and steam fractions from gas compositions. Trans Geotherm Res Council 9, 305-310.

Diakonov, I. I., Schott, J., Martin, F., Harrichourry, J. C., and Escalier, J., 1999. Iron(III) solubility and speciation in aqueous solutions. Experimental study and modelling: Part 1. Hematite solubility from 60 to 300 degrees C in NaOH-NaCl solutions and thermodynamic properties of Fe(OH)(4)-(aq). Geochim Cosmochim Ac 63, 2247-2261.

Einarsson, P., 1991. Earthquakes and Present-Day Tectonism in Iceland. Tectonophysics 189, 261-279.

Einarsson, P., 2008. Plate boundaries, rifts and transforms in Iceland. Jökull 58, 35-58.

Einarsson, T., 1960. Geologie von Hellisheidi (in German). Kommissionsverlag und Auslieferung für den Buchhandel W. Stollfuss, Köln,.

Eshaghpour, M., 2003. Borehole Geology and Alteration Mineralogy of Well HE-9 in Hellisheidi Geothermal Field, SW-Iceland. The United Nations University, Geothermal Training Programme, Reykjavík, Iceland.

Fernandez-Prini, R., Alvarez, J. L., and Harvey, A. H., 2003. Henry's constants and vapor-liquid distribution constants for gaseous solutes in H_2O and D_2O at high temperatures. J Phys Chem Ref Data 32, 903-916.

Foulger, G. R., 1984. The Hengill geothermal area: Seismological studies 1978-1984. Science Institute, University of Iceland, Reykjavík, Iceland.

Foulger, G. R., 1995. The Hengill Geothermal Area, Iceland - Variation of Temperature-Gradients Deduced from the Maximum Depth of Seismogenesis. J Volcanol Geoth Res 65, 119-133.

Foulger, G. R. and Toomey, D. R., 1989. Structure and Evolution of the Hengill-Grensdalur Volcanic Complex, Iceland - Geology, Geophysics, and Seismic Tomography. J Geophys Res-Solid 94, 17511-17522.

Franzson, H., 1988. Nesjavellir, Borholujardfraedi, Vatnsgengd i jardhitageymi (Nesjavellir, Borehole geology, Geothermal Fluid Type). Orkustofnun, Reykjavík, Iceland.

Franzson, H., 1994. Nesjavellir, Thaettir af ummyndun i jardhitakerfi (Nesjavellir, Geological Investigations). Orkustofnun, Reykjavík, Iceland.

Franzson, H., 1998. Reservoir Geology of the Nesjavellir High-Temperature Field in SW-Iceland. 15th Annual PNOC-EDC Geothermal Conference, Manila, Philippines.

Franzson, H., Gudlaugsson, S. T., and Fridleifsson, G. O., 2001. Petrophysical Properties of Icelandic Rocks. Sixth Nordic Symposium on Petrophysics, Trondheim, Norway.

Franzson, H., Gunnlaugsson, E., Árnason, K.., Saemundsson, K., Steingrimsson, B., and Hardarson, B. S., 2010. The Hengill Geothermal System, Conceptual Model and Thermal Evolution. World Geothermal Congress, Bali, Indonesia.

Franzson, H., Kristjansson, B. R., Gunnarsson, G., Björnsson, G., Hjartarson, A., Steingrimsson, B., Gunnlaugsson, E., and Gislason, G., 2005. The Hengill-Hellisheidi Geothermal Field, Development of a Conceptual Geothermal Model. World Geothermal Congress, Antalya, Turkey.

Fridleifsson, G. O., Ármansson, H., Árnason, K.., Bjarnason, I. T., and Gislason, G., 2003. Iceland Deep Drilling Project, Part 1, Geosciences - Site Selection. Iceland Deep Drilling Project, Reykjavík, Iceland.

Gebrehiwot, K., Koestono, H., Franzson, H., and Mortensen, A. K., 2010. Borehole Geology and Hydrothermal Alteration of Well HE-24, Hellisheidi Geothermal Field, SW-IcelandWorld Geothermal Congress, Bali, Indonesia.

Getaneh, E., 2001. Borehole Geology and Alteration Mineralogy in the Upper Half of Well HE-3, Hellisheidi, SW-Iceland. The United Nations University, Geothermal Training Programme, Reykjavík, Iceland.

Giroud, N., 2008. A chemical study of arsenic, boron and gases in high-temperature geothermal fluids in Iceland. PhD Thesis, Faculty of Science, University of Iceland.

Gudmundsson, A., 1995. Infrastructure and Mechanics of Volcanic Systems in Iceland. J Volcanol Geoth Res 64, 1-22.

Gudmundsson, B. T. and Arnórsson, S., 2002. Geochemical monitoring of the Krafla and Namafjall geothermal areas, N-Iceland. Geothermics 31, 195-243.

Gudmundsson, B. T. and Arnórsson, S., 2005. Secondary mineral-fluid equilibria in the Krafla and Namafjall geothermal systems, Iceland. Appl Geochem 20, 1607-1625.

Gunnarsson, G., Arnaldsson, A., and Oddsdóttir, A. L., 2010. Model Simulations of the Hengill Area, Southwestern Iceland . Transp Porous Med (in press).

Gunnarsson, G. and Kristjansson, B. R., 2003. An Assessment of Intrusive Intensity in Lower Part of Wells HE-3 to HE-7 at Hellisheidi (in Icelandic). Orkustofnun, Reykjavík, Iceland.

Gunnarsson, I. and Arnórsson, S., 2000. Amorphous silica solubility and the thermodynamic properties of H_4SiO_4 degrees in the range of 0 degrees to 350 degrees C at P-sat. Geochim Cosmochim Ac 64, 2295-2307.

Hardarson, B. S., Einarsson, G. M., Kristjansson, B. R., Gunnarsson, G., Helgadóttir, H. M., Franzson, H., Árnason, K.., Agustsson, K., and Gunnlaugsson, E., 2010. Geothermal Reinjection at the Hengill Triple Junction, SW Iceland. World Geothermal Congress, Bali, Indonesia.

Hartanto, D. B., 2005. Borehole Geology and Alteration Mineralogy of Well HE-11, Hellisheidi Geothermal Field, SW-Iceland. The United Nations University, Geothermal Training Programme, Reykjavík, Iceland.

Heinrich, C., 2005. The physical and chemical evolution of low-salinity magmatic fluids at the porphyry to epithermal transition: a thermodynamic study. Miner Deposita 39, 864-889.

Helgadóttir, H. M., Snaebjornsdóttir, S. O., Nielsson, S., Gunnarsdóttir, S. H., Matthiasdóttir, T., Hardarson, B. S., Einarsson, G. M., and Franzson, H., 2010. Geology and Hydrothermal Alteration in the Reservoir of the Hellisheidi High Temperature System, SW-Iceland. World Geothermal Congress, Bali, Indonesia.

Helgeson, H. C., 1967. Thermodynamics of complex dissociation in aqueous solution at elevated temperatures. J. Phys. Chem. 71, 3121-3136.

Helgeson, H. C., Brown, T. H., Nigrini, A., and Jones, T. A., 1970. Calculation of Mass Transfer in Geochemical Processes Involving Aqueous Solutions. Geochim Cosmochim Ac 34, 569-&.

Holland, T. J. B. and Powell, R., 1998. An internally consistent thermodynamic data set for phases of petrological interest. J Metamorph Geol 16, 309-343.

Horne, R. N., Satik, C., Mahiya, G., Li, K., Ambusso, W., Tovar, R., Wang, C., and Nassori, H., 2000. Steam-Water Relative PermeabilityWorld Geothermal Congress, Kyushu-Tohuku, Japan.

Hreggvidsdóttir, H., 1987. The Greenschist to Amphibolite Transition in the Nesjavellir Hydrothermal System, Southwest Iceland. Masters thesis, Stanford University.

Ingebritsen, S. E., Geiger, S., Hurwitz, S., and Driesner, T., 2010. Numerical Simulation of Magmatic Hydrothermal Systems. Rev Geophys 47, -.

Ivarsson, G., 1998. Fumarole gas geochemistry in estimating subsurface temperatures at Hengill in Southwestern Iceland. Proceedings of the 9th Symposium on Water-Rock Interaction, Balkema.

Jakobsson, S. P. and Gudmundsson, M. T., 2008. Subglacial and intraglacial volcanic formations in Iceland. Jokull 58, 179-196.

Johannesson, H., 1980. Jardlagaskipan og Throun rekbelta a Vesturlandi (Evolution of Rift Zones in Western Iceland). Natturufraedingurinn 50, 13-39.

Johnson, J. W., Oelkers, E. H., and Helgeson, H. C., 1992. Supcrt92 - a Software Package for Calculating the Standard Molal Thermodynamic Properties of Minerals, Gases, Aqueous Species, and Reactions from 1-Bar to 5000-Bar and 0-Degrees-C to 1000-Degrees-C. Comput Geosci 18, 899-947.

Jousset, P., Haberland, C., Bauer, K., Árnason, K.., Weber, M., and Fabriol, H., 2010. Seismic Tomography and Long-Period Earthquakes Observation and Modelling at the Hengill Geothermal Volcanic Complex, IcelandWorld Geothermal Congress, Bali, Indonesia.

Karingithi, C. W., Arnórsson, S., and Gronvold, K., 2010. Processes controlling aquifer fluid compositions in the Olkaria geothermal system, Kenya. J Volcanol Geoth Res 196, 57-76.

Koestono, H., 2007. Borehole Geology and Hydrothermal Alteration of Well HE-24, Hellisheidi Geothermal Field, SW-Iceland. The United Nations University, Geothermal Training Programme, Reykjavík, Iceland.

Kristmansdóttir, H., 1979. Alteration of Basaltic Rocks by Hydrothermal Activity at 100-300°C. In: Mortland, M. M. and Farmer, V. C. Eds., International Clay Conference 1978. Elsevier Scientific Publishing Co., Amsterdam, Netherlands.

LaFemina, P. C., Dixon, T. H., Malservisi, R., Arnadóttir, T., Sturkell, E., Sigmundsson, F., and Einarsson, P., 2005. Geodetic GPS measurements in south Iceland: Strain accumulation and partitioning in a propagating ridge system. J Geophys Res-Sol Ea 110, -.

Larsson, D., Grönvold, K., Oskarsson, N., and Gunnlaugsson., E., 2002. Hydrothermal alteration of plagioclase and growth of secondary feldspar in the Hengill Volcanic Centre, SW Iceland. J of Volcanol and Geoth Res 114, 275-290.

Mesfin, K. G., 2010. Subsurface geology, hydrothermal alteration and geothermal model of Northern Skardsmyrarfjall, Hellisheidi geothermal field, SW Iceland. Masters Thesis, University of Iceland.

Mutonga, M. W., Sveinbjornsdóttir, A., Gislason, G., and Ármansson, H., 2010. The Isotopic and Chemical Characteristics of Geothermal Fluids in Hengill Area, SW-Iceland (Hellisheidi, Hveragerdi and Nesjavellir Fields)World Geothermal Congress, Bali, Indonesia.

Nielsson, S. and Franzson, H., 2010. Geology and Hydrothermal Alteration of the Hverahlid HT-System, SW-Iceland. World Geothermal Congress, Bali, Indonesia.

Pendon, R. R., 2006. Borehole Geology and Hydrothermal Mineralisation of Well HE-22, Olkelduhals Field, Hengill Area, SW-Iceland. The United Nations University, Geothermal Training Programme, Reykjavík, Iceland.

Plummer, L. N. and Busenberg, E., 1982. The Solubilities of Calcite, Aragonite and Vaterite in CO2-H2O Solutions between 0-Degrees-C and 90-Degrees-C, and an Evaluation of the Aqueous Model for the System CaCO3-CO2-H2O. Geochim Cosmochim Ac 46, 1011-1040.

Pokrovskii, G. S., Schott, J., Salvi, S., Gout, R., and Kubicki, J. D., 1998. Structure and stability of aluminium-silica complexes in neutral to basic solution. Experimental study and molecular orbital calculations. Min. Mag. 62A, 1194-1195.

Pokrovskii, V. A. and Helgeson, H. C., 1995. Thermodynamic properties of aqueous species and the solubilities of minerals at high pressures and temperatures: The system Al2O3-H2O-NaCl. Am J Sci 295, 1255-1342.

Pruess, K., 2002. Mathematical modeling of fluid flow and heat transfer in geothermal systems - an introduction in five lectures. United Nations University, Geothermal Training Programme, Reykjavík, Iceland.

Remoroza, A. I., 2010. Calcite Mineral Scaling Potentials of High-Temperature Geothermal Wells. MSc thesis, Faculty of Science, University of Iceland.

Robie, R. A., Hemingway, B. S., and Geological Survey (U.S.), 1995. Thermodynamic properties of minerals and related substances at 298.15 K and 1 bar (10 pascals) pressure and at higher temperatures. U.S. G.P.O. ;

Saemundsson, K., 1967. Vulkanismus und Tektonik des Hengill - Gebietes in Sudwest-Island. (in German) Volcanology and tectonics of the Hengll area in SW Iceland). Acta Nat. Isl. 2, 109 pp.

Saemundsson, K., 1992. Geology of the Thingvallavatn Area. Oikos 64, 40-68.

Saemundsson, K., 1995a. Geological Map of the Hengill Area 1:50,000. Orkustofnun, Hitaveita Reykjavíkur and Landmaelingar Islands, Reykjavík, Iceland.

Saemundsson, K., 1995b. Hengill, Jardhiti, Ummyndun og Grunnvatn (Hengill, Geothermal Activity, Alteration and Groundwater). . Orkustofnun, Reykjavík, Iceland.

Saemundsson, K. and Arnórsson, S., 1971. Geinagerd um borhol Asi 1 hja Olfusborgum i Olfusi (Well Asi 1 near Olfusborgir in Olfus). Orkustofnun, Reykjavík, Iceland.

Schiffman, P. and Fridleifsson, G. O., 1991. The Smectite Chlorite Transition in Drillhole Nj-15, Nesjavellir Geothermal-Field, Iceland - Xrd, Bse and Electron-Microprobe Investigations. J Metamorph Geol 9, 679-696.

Sigmundsson, F., Einarsson, P., Bilham, R., and Sturkell, E., 1995. Rift-Transform Kinematics in South Iceland - Deformation from Global Positioning System Measurements, 1986 to 1992. J Geophys Res-Sol Ea 100, 6235-6248.

Sigmundsson, F., Einarsson, P., Rognvaldsson, S. T., Foulger, G. R., Hodgkinson, K. R., and Thorbergsson, G., 1997. The 1994-1995 seismicity and deformation at the Hengill triple junction, Iceland: Triggering of earthquakes by minor magma injection in a zone of horizontal shear stress. J Geophys Res-Sol Ea 102, 15151-15161.

Sigurdsson, H., 2000. Encyclopedia of volcanoes. Academic, San Diego, Calif. ; London.

Sinton, J., Gronvold, K., and Saemundsson, K., 2005. Postglacial eruptive history of the Western Volcanic Zone, Iceland. Geochem Geophy Geosy 6, -.

Stefánsson, A. and Arnórsson, S., 2002. Gas pressures and redox reactions in geothermal fluids in Iceland. Chem Geol 190, 251-271.

Stefánsson, A., Arnórsson, S., Gunnarsson, I., and Kaasalainen, H., 2009. Forgun brennisteins fra Hellisheidarvirkjun Jardefnafraedileg athugun. University of Iceland, Institute of Earth Sciences, Reykjavík, Iceland.

Stefánsson, A., Arnórsson, S., Gunnarsson, I., Kaasalainen, H., and Gunnlaugsson, E., 2011. The geochemistry and sequestration of H_2S into the hydrothermal system at Hellisheidi, Iceland. J Volcanol Geoth Res (in press).

Steingrimsson, B., Gudmundsson, A., Franzson, H., and Gunnlaugsson, E., 1990. Evidence of a supercritical fluid at depth in the Nesjavellir field. Fifteenth Workshop on Geothermal Reservoir Engineering, Stanford University, Stanford, CA.

Steingrimsson, B., Gudmundsson, A., Sigvaldason, H., Sigurdsson, O., and Gunnlaugsson, E., 1986. Nesjavellir, Hola NJ-11, Borun, rannsoknir og vinnslueiginleikar (Well Report NJ-11). Orkustofnun, Reykjavík, Iceland.

Thorbergsson, G., Magnusson, I. T., Gunnarsson, A., Johnsen, G. V., and Björnsson, A., 1984. Geodetic and gravity survey of the Hengill area 1982 and 1983 (in Icelandic). Orkustofnun, Reykjavík, Iceland.

Thordarson, T. and Larsen, G., 2007. Volcanism in Iceland in historical time: Volcano types, eruption styles and eruptive history. J Geodyn 43, 118-152.

Tryggvason, A., Rognvaldsson, S. T., and Flovenz, O. G., 2002. Three-dimensional imaging of the P- and S-wave velocity structure and earthquake locations beneath Southwest Iceland. Geophys J Int 151, 848-866.

Vogfjörd, K. S. and Hjaltadóttir, S., 2007. Kortlagning skjalftavirkni vid Hverahlid a Hellisheidi i Februar 2006. Vedurstofa Islands, Reykjavík, Iceland.